Multi-wavelength Extreme Ultraviolet Ptychography for Imaging and Wavefront Sensing

Antonios Pelekanidis

VRIJE UNIVERSITEIT

Multi-wavelength Extreme Ultraviolet Ptychography for Imaging and Wavefront Sensing

ACADEMISCH PROEFSCHRIFT

ter verkrijging van de graad Doctor of Philosophy
aan de Vrije Universiteit Amsterdam,
op gezag van de rector magnificus
prof.dr. J.J.G. Geurts,
volgens besluit van de decaan
van de Faculteit der Bètawetenschappen
in het openbaar te verdedigen
op woensdag 17 september 2025 om 13.45 uur
in de universiteit

door

Antonios Pelekanidis

geboren te Thessaloniki, Griekenland

promotoren:	prof.dr. S.M. Witte
	prof.dr. K.S.E. Eikema
promotiecommissie:	dr. P.M. Kraus
	dr. L.V. Amitonova
	prof.dr. K.J. Batenburg
	prof.dr. M.P. van Exter
	dr. T. Ruchon

This work was carried out at the Advanced Research Center for Nanolithography (ARCNL), a public-private partnership between the University of Amsterdam (UvA), Vrije Universiteit Amsterdam (VU), Rijksuniversiteit Groningen (RUG), the Dutch Research Council (NWO), and the semiconductor equipment manufacturer ASML.
This work was supported by the Dutch Research Council (Perspectief program LINX, grant agreement no. P16-08).

Cover: Concept and design by Antonios Pelekanidis
Printed by: ProefschriftMaken, Amsterdam, The Netherlands
DOI: https://doi.org/10.5463/thesis.1262
A digital version of this thesis is available at: https://research.vu.nl/

"Wise as you will have become, so full of experience, you'll have understood by then what these Ithakas mean." - C. P. Cavafy

Contents

Chapter 1

Introduction

1.1 Lensless imaging

Scientific research has seen a great boost thanks the development of microscopy, that enables us to look at tiny structures beyond the physical capabilities of the human eye. The most characteristic example of great advancement thanks to microscopes is biology and medicine. In that regard, improvement of microscopy systems has been an ongoing research topic on each own. Next-generation advanced microscopes used for biomedical applications and semiconductor metrology may be required to have specifications that will be challenging for conventional microscopes, based on magnifying optics. Therefore, lensless diffractive imaging techniques have emerged as alternatives and outperform lens-based microscopes at specific applications [1, 2]. By "lensless" we mean that there are no optics between the object of interest and a detector, which is typically a camera. "Diffractive" means that the detector captures the diffracted signal following the incidence of light on the object. Therefore, the detector does not get a directly magnified image of the object of interest, but the object is numerically reconstructed from the recorded diffraction information.

The first advantage of lensless imaging is on the achievable spatial resolution. According to Abbe's diffraction limit theory, the resolution is proportional to the wavelength of the illumination and is given by the equation $\Delta x = \lambda/2NA$, where λ is the wavelength and NA is the numerical aperture of the microscopy system [3]. Therefore, nanometer-scale resolution, which is the current requirement for many biomedical and semiconductor industry applications, can in principle be achieved with microscopes using light in the extreme ultraviolet (XUV) and soft X-ray (SXR) range. However, focusing optics for such wavelengths have limited capabilities in terms of losses and image distortions. On the other hand, lensless imaging techniques are in principle extensible to any wavelength of the illumination source.

Besides the spatial resolution, lensless imaging techniques offer element-specific

contrast [4]. The numerical reconstruction of the object is based on modelling the propagation of light from the measurement plane to the detector plane, where the object is considered an interface that interacts with the light. Therefore, the numerical reconstruction is typically a complex-valued expression of the transmission or reflection function of the object, depending whether the light is transmitted through or reflected from the object. This complex-valued representation contains quantitative information about the optical properties of the object, which are element-specific, as each element has a distinct refractive index at the wavelength of the incident illumination.

As mentioned before, numerical reconstruction from diffraction data is possible because we have analytical expressions that describe the propagation of coherent light from the measurement plane to the detector plane. If we consider the configuration of Fig. 1.1, where we know the electric field distribution at the object plane (plane 1) with coordinates (x_1, y_1), we can precisely determine the electric field at a plane 2 with coordinates (x_2, y_2), at distance z_0 from plane 1, which is the detector plane, and vice versa. The analytical expression connecting the fields between these two planes is, according to the Huygens-Fresnel principle [5]:

$$U(x_2, y_2) = \frac{z_0}{j\lambda} \iint_{-\infty}^{\infty} U(x_1, y_1) \frac{e^{jkr}}{r^2} dx_1 dy_1 \tag{1.1}$$

where λ is the wavelength, $k = \frac{2\pi}{\lambda}$ and

$$r = \sqrt{z_0^2 + (x_2 - x_1)^2 + (y_2 - y_1)^2} = z_0 \sqrt{1 + \frac{(x_2 - x_1)^2 + (y_2 - y_1)^2}{z_0^2}}. \tag{1.2}$$

The Huygens-Fresnel principle treats each individual point at the measurement

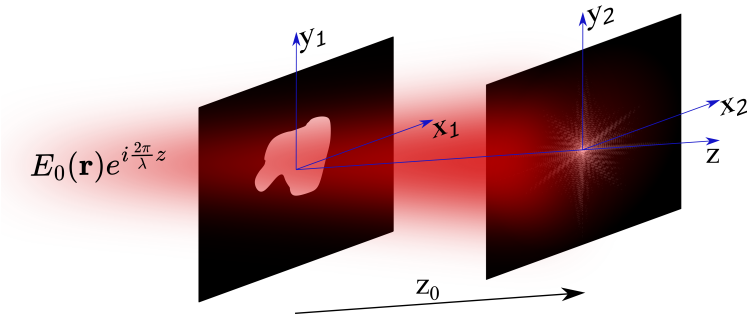

Figure 1.1: Schematic of a lensless imaging setup, explaining Eq. (1.1). A monochromatic light source illuminates the object plane and the diffracted signal propagates towards the detector plane. In Eq. (1.1), the input field distribution at plane 1 $U(x_1, y_1)$ is equal to $U(x_1, y_1) = T(x_1, y_1)E_0(x_1, y_1, z_1)e^{i\frac{2\pi}{\lambda}z_1}$, where T is the transmission function of the object and $E_0 e^{i\frac{2\pi}{\lambda}z_1}$ is the laser field distribution at plane 1. For simplicity we have assumed plane wave propagation of the incoming wave.

plane as a point source that emits a spherical wave. The resulting field at the detector plane will be the superposition of all these spherical waves. Under the paraxial approximation, which mathematically means that $(x_2 - x_1)^2 + (y_2 - y_1)^2 \ll z_0^2$, the expression for r can be simplified with a binomial expansion $\sqrt{1+b} = 1 + 1/2\, b - 1/8\, b^2 + \ldots$. At the exponent of the expression e^{jkr} we will keep the first two terms of the expansion and for the denominator of e^{jkr}/r^2 we will keep only the first term. The propagation expression can then be written as:

$$U(x_2, y_2) = \frac{e^{jkz_0}}{j\lambda z_0} \iint_{-\infty}^{\infty} U(x_1, y_1) e^{j\frac{k}{2z_0}\left((x_2-x_1)^2+(y_2-y_1)^2\right)} dx_1 dy_1 \tag{1.3}$$

which is known as the Fresnel integral. In Ch. 2 we start from the Fresnel integral and its discretized form and derive the propagation models that we have used in all the numerical analysis that follows in the rest of the thesis.

From the Fresnel integral we can be observe that the incident light on the detector is a complex-valued quantity with amplitude $|U|$ and phase $\angle U$. However, the detectors that are available for light detection can only capture the intensity of the light, which is proportional to $|U|^2$, therefore all phase information is lost. There are various lensless diffractive methods that each uses a different approach in solving the phase retrieval problem. In all the following chapters in this thesis we use ptychography, but before introducing ptychography we will address briefly other methods that have been also developed.

One way to measure the phase of the transmitted light through an object, called thereafter exit wave, is via holography [6]. In holography the exit wave is interfered with a reference wave and the phase is imprinted in the interference pattern. The reference wave can be on-axis [6] or off-axis [7] with respect to the wave incident on the object, while the detector can be in the near field or the far field of the object. For far-field detection, Fourier Transform Holography has been developed [8–10], where the reference wave is transmitted through a pinhole and the image reconstruction is basically achieved via a spatial Fourier transform of the interference pattern.

A reference-free approach for lensless diffractive imaging is Coherent diffractive imaging (CDI), that was first introduced in [11] for x-ray crystallography, but was later developed and used successfully for imaging arbitrary structures with illuminating wavelengths ranging from visible to x-ray [12–17]. Here the object must be confined spatially, so that there is prior knowledge of the object surroundings, which is called finite support constraint. The reconstruction happens in an iterative manner, where the reconstruction algorithm starts with an initial guess for the object and propagates the exit wave from the object plane to the detector plane and backwards. At every plane the respective constraints are applied, which are the diffraction pattern intensity at the detector plane and the finite support at the object plane. Therefore, every iteration yields a better estimate for the object until the algorithm converges to a solution.

Sometimes, for instance when an object contains elements with absorption edges at characteristic energies, it is useful to have a non-monochromatic illumination source with photon energies matching those energies, as that can lead

to increased element contrast [4]. The diffraction patterns for polychromatic illumination exhibit blurred features due to wavelength-dependent diffraction, which may deteriorate the reconstructed image quality of a CDI measurement. A solution to this spectral blurring effect was proposed in [18], which combines the concept of Fourier Transform Spectroscopy [19] with diffractive imaging, and which was further explored and developed in [20–22]. In this technique, the object is illuminated by two time-delayed coherent pulses, resulting in a delay-dependent interference pattern in the detector. With appropriate delay scan in terms of step size and total range, the authors were able to retrieve the spectrum of every pixel in the diffraction pattern and monochromatize the diffraction patterns accordingly. Then, the challenging task of image reconstruction based on the polychromatic diffraction pattern was converted into easier tasks of reconstructing the image per wavelength based on the calculated monochromatic diffraction patterns.

A scanning variation of CDI that allows us to image extended objects is ptychography [23], which is explained in more detail in the next section. Ptychography has a few advantages with respect to CDI or holography. Two such advanced properties of ptychography are 1) the high-quality imaging without any requirement for prior knowledge of the object or dependence on a reference beam and 2) the opportunity to reconstruct complex-valued expression of the illumination along with the object of interest, thus making ptychography an advanced wavefront sensing technique [4].

1.2 Ptychography

Ptychography, first developed and demonstrated in [23–25], is a scanning CDI variation, where the object of interest ($O(r)$) is on a stage that can move laterally to the illumination. The detector captures a series of diffraction patterns for all the object scan positions. The scan grid is designed such that there are overlapping illuminated areas between adjacent scan positions. This overlap leads to correlated diffraction patterns, which allows the reconstruction algorithm, through an iterative process, to converge to a unique solution for both the object and the wavefront of the illumination, which in ptychography is called probe ($P(r)$). A schematic of a ptychography setup is shown in Fig. 1.2.

The ptychographic reconstruction algorithm can be described by the following steps:

Ptychographic algorithm

1. iteration = 0
2. iteration = iteration + 1, scan position = 0
3. scan position = scan position + 1
4. Calculate exit wave $\psi(r) = P(r) \cdot O(r - r_j)$

5. Propagate exit wave to detector $\Psi(q) = \mathscr{P}\{\psi(r)\}$
6. Compare $I_{measured}(q)$ and $I_{estimated}(q) = |\Psi(q)|^2$, calculate error and perform intensity projection
7. Back-propagate updated field from the detector to the object plane $\psi^{updated}(r) = \mathscr{P}^{-1}\{\Psi^{updated}(q)\}$
8. Update $P(r)$ and $O(r - r_j)$ from $\psi^{updated}(r)$
9. If not all scan positions have been checked, move to step 3; else, move to step 2

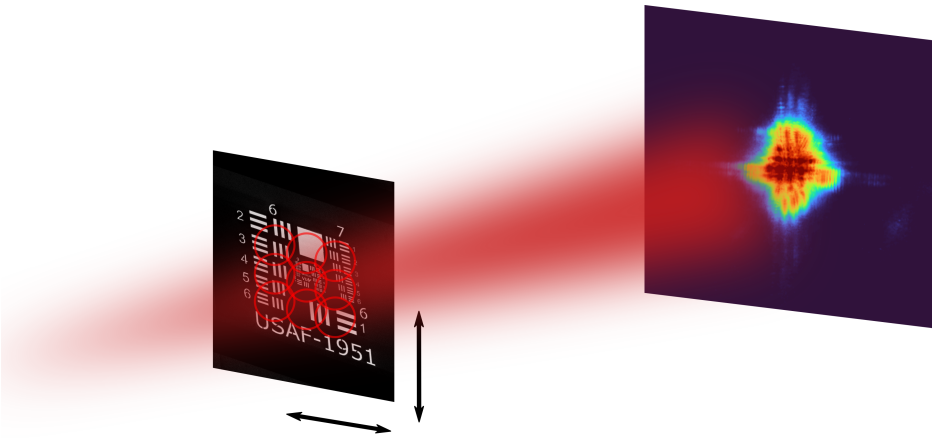

Figure 1.2: Schematic of a ptychography setup. A coherent light beam illuminates the sample of interest and a camera captures the diffraction pattern. The sample is on a stage moving laterally with respect to the beam, so that we record diffraction patterns from different but overlapping areas of the sample.

The algorithm usually stops when the error has converged, which means that the probe and object have stopped updating. In the above algorithm, the forward and backward wave propagation, denoted with the operators $\mathscr{P}$ and $\mathscr{P}^{-1}$ respectively, is performed according to Eq. (1.3) for coherent monochromatic light and far-field conditions. In the case of multi-wavelength illumination, the exit wave is calculated separately for each wavelength ($\psi_\lambda(r)$) and propagated to the detector ($\mathscr{P}_\lambda\{\psi_\lambda(r)\}$). At the detector plane the intensities from each wavelength are added incoherently and compared with the measured intensity. More details about multi-wavelength ptychography are given in Section 1.5. Furthermore, the intensity projection is an operation that updates the estimated diffraction signal using the measured signal information. The exact operation is based on the assumed noise statistics during the data acquisition. For the works described in this thesis we assume the measurements are dominated by pho-

ton noise and update the amplitude of the estimated diffraction signal [26, 27] $\Psi^{updated} = \frac{\sqrt{I_{measured}}}{|\Psi|+\epsilon} \cdot e^{i\angle\Psi}$, with ϵ a small number introduced to prevent division with zero.

The functionality of probe update was not available in the original implementation of the ptychographic reconstruction algorithm, called Ptychographic Iterative Engine (PIE) [23], but was later added in [28–30], leading to the extended PIE (ePIE) algorithm. The expressions for the update of both probe and object are given in [30]. This is a remarkable feature of ptychography, as high-quality imaging can be achieved even with strongly aberrated wavefronts or distorted beam profiles, while certain assumptions for the illumination have to be made for other lensless diffractive methods. On the contrary, as it will be explained in Section 1.3, it is usually beneficial in ptychography to have beams with a structured amplitude or phase profile.

Ptychography has been demonstrated in experimental setups with XUV illumination in both transmission [31] and reflection [32] mode. Since the first demonstrations, there have been many studies with both illumination modes. In principle, the transmission mode is preferred for imaging two-dimensional or thin samples with respect to the penetration depth [33–37], while the reflection mode is used for imaging the outer layers of a thick sample [38–40]. The working principles of ptychography are identical for transmission and reflection mode, with the exception that in reflection the sample and the detector are not in parallel planes and tilt plane correction is required as a first step.

A ptychographic measurement has a few design parameters that need to be considered in advance for a successful reconstruction, as measurement and reconstruction happen asynchronously. For example, the scan grid needs to be designed in a way that the full area of interest in scanned and sufficient overlap between adjacent scan positions is satisfied. However, increased overlap leads to an increased number of scan positions in order to cover the desired field of view, which can have implications on the measurement time and memory issues for the computer that will run the reconstruction algorithm. In [41], an overlap factor of 60% is concluded to be sufficient for a ptychographic scheme with a monochromatic probe. Another important design aspect is the oversampling factor [42]. The oversampling factor poses a constraint on the extent of the probe, as a largely illuminating area of the object may cause diffraction features that cannot be sufficiently sampled by the detector. The maximum probe size should be, therefore, equal to $\lambda z/2dq$, with λ the wavelength of the probe, z the distance between sample and detector and dq the pixel size of the detector.

Apart from optimized design parameters in the measurement setup, there are a few algorithmic techniques that can contribute to a high-quality imaging performance. Since ptychography was first introduced, many groups around the world developed variations of the original PIE/ePIE engines oriented towards enhanced imaging quality. For example, if the beam is partially coherent, the mixed states approach decomposes the probe into a set of incoherent modes [43]. This approach can also be used when there are external sources of decoherence that have an equivalent effect on the diffraction patterns, such as high-frequency sample vibrations, background, or for finite spectral bandwidth [35]. Other variations of

the ePIE algorithm have been developed for multi-wavelength illumination [44], beam pointing instability [45], object to camera distance calibration [46], tilt angle calibration on reflection mode ptychography [47], scan positions correction [48], three-dimensional object reconstruction [49] and super-resolution imaging [50]. Finally, Gardner *et al.* proposed the use of the undiffracted probe information in the reconstruction algorithm and showed a significant improvement in imaging quality [51].

Reported potential applications of ptychography are in imaging of biological samples [33, 36, 52, 53], in inspection of wafers and XUV mirrors [39, 54–56], and for wavefront sensing [28, 30, 45, 57–63]. The latter is especially interesting for XUV light, as the most standard way to generate coherent XUV light is via high harmonic generation (HHG), discussed in detail in Section 1.4, and wavefront sensing on HHG beams can be used to to answer fundamental questions of the HHG process. We address such fundamental questions in Chs. 3 and 4, which we manage to answer thanks to the wavefront sensing capabilities of ptychography.

Throughout this thesis we show ptychographic reconstructions using the aforementioned ePIE algorithm or variations of it. However, recently different approaches to solve the phase retrieval problem have been introduced, inspired by machine learning models. One such approach uses a physics-based forward model to describe the propagation of the exit wave from the object plane to the camera and implements an iterative algorithm to update the probe and object based on automatic differentiation (AD) [40, 64–66]. This approach turns out to be more flexible than ePIE, as any model parameter besides the object and probe pixel values, such as scan positions, distance, wavelength, angle, can be set to either "trainable" or "non-trainable" and be updated as well. We believe that this approach has great potential to solve any kind of ptychography problem in the future.

1.3 Structured illumination

The highest resolution that can be achieved with ptychography (without resorting to superresolution techniques) is the diffraction-limited resolution $\Delta x = \lambda/2NA$ mentioned also in Section 1.1. In microscopy, however, people often assume a composite definition for NA, or effective NA, defined as $NA_{eff} \approx NA_{ill} + NA_{det}$ [67], where NA_{ill} is the NA of the illumination (i.e. the Fourier transform of the optical system's exit pupil), and NA_{det} is the detection NA, with $NA_{det} = L_d/2z$. Here z is the distance between the sample of interest and the detector and L_d the detector size, where for simplicity we have considered a square detector and equal resolution limit in x and y direction. This extended concept of NA motivated the authors of [50] to develop the superresolution ptychographic algorithm, which basically can lead to increased resolution of the object in the order of $\Delta x = \lambda/2NA_{eff}$.

In practice, typically the detector is aligned such that the undiffracted probe illuminates the center of the detector. Sometimes, for example in case of a weakly diffracting object illuminated by a probe with low illumination NA, most photons will end up around the center of the detector and effectively any signal at

the edges of the detector will be very weak and "buried" under the noise level. Consequently, introducing a high illumination NA in the probe, such that the undiffracted probe already illuminates a large part of the detector, is an efficient way to increase the effective NA of the system.

A high illumination NA can be interpreted as a large spectrum of k vectors in the beam, thus rays that propagate in different directions. An intuitive way to increase the illumination NA of the probe is by adding divergence to a standard Gaussian-like probe [68, 69], but still in such probe configuration most energy is directed towards the center of the detector. An efficient alternative is structured illumination, which means introducing some structure in either the amplitude or the phase of the beam. There have been many studies showing how structured illumination can optimize the object resolution [34, 35, 69–75]. In fact, the benefit of structuring the probe is twofold. First, the diffracted signal is spread across the full detector, increasing the effective NA. Second, structuring mitigates the saturation of the center of the detector from zeroth order diffraction, allowing us to use a probe with higher photon flux. The higher probe photon flux eventually leads to better reconstruction quality [4].

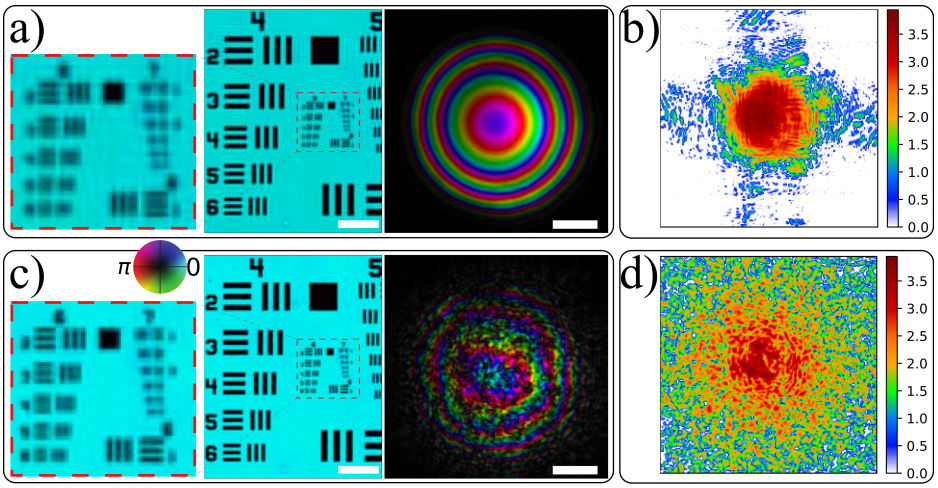

Figure 1.3: Ptychography reconstructions with a,b) smooth and c,d) structured illumination. a,c) Object and probe reconstructions. The scale bar is equal to 200 µm. Brighness indicates the amplitude and hue the phase. b,d) Example diffraction patterns in logarithmic scale.

In Fig. 1.3 we show an example reconstruction of a USAF 1951 resolution target with a smooth (Fig. 1.3a)) and a structured (Fig. 1.3c)) monochromatic probe at wavelength 700 nm. For a laser beam at the NIR or visible spectrum we can easily structure the beam by placing a piece of scotch tape on an aperture and imaging that aperture on the sample plane, which is how the probe in Fig. 1.3c) was generated. From the object reconstructions we see a clear improvement in the imaging quality for the case with the structured probe, without artifacts and clear

resolution of the features up to the Element 3 in Group 6. In Figs. 1.3b) and 1.3d) we also show diffraction patterns in logarithmic scale from random scan positions for the smooth and structured illumination respectively, where we can observe that there is higher signal on the edges of the detector for the structured probe compared to the smooth probe. It is also clear how for structured illumination the photons are more uniformly spread across the detector, which prevents saturation of the center of the camera.

For ptychography measurements with XUV and X-ray illumination it is more challenging to efficiently structure the probe. In [34, 35, 71–73, 76] the authors used diffractive binary masks in order to structure XUV and X-ray beams, such as zone plates or arrays of small apertures. However, such a technique leads to a decrease in the photon flux of the probe, as part of the beam is blocked. Recently, Eschen *et al.* proposed an EUV phase-shift diffuser that enables structuring the probe while achieving higher transmission through the diffuser compared to a binary mask [75].

1.3.1 Vortex illumination

A different approach to structuring the probe in the XUV and SXR was proposed in [69], where the authors used a beam carrying orbital angular momentum (OAM), also known as vortex beam, to image an object with periodic structures. As it will be explained in the next section, they managed to introduce OAM to the XUV beam without placing any lossy optics or masks in the XUV beamline.

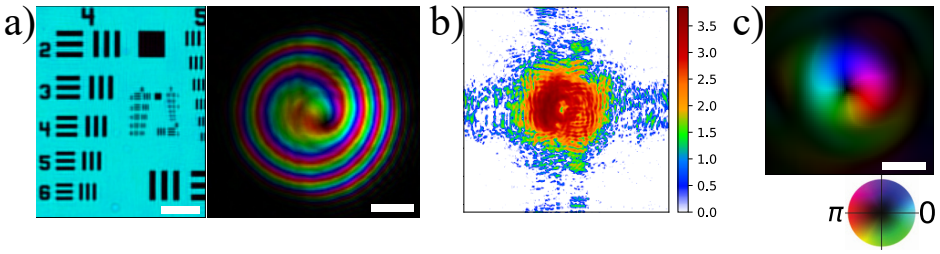

Figure 1.4: Ptychography reconstruction with vortex illumination. a) Object and probe reconstructions. The scale bar is equal to 200 µm. Brightness indicates the amplitude and hue the phase. b) Example diffraction pattern in logarithmic scale. c) Numerically backpropagated beam at the focal plane. Scale bar is equal to 50 µm. In a,c) brightness indicates the amplitude and hue the phase.

The effect of OAM in the beam is illustrated in Fig. 1.4, where we show an experimental demonstration of a ptychographic reconstruction with a NIR beam carrying OAM. The OAM beam has a singularity in the centre with the intensity approaching to zero. Therefore, the zeroth order diffraction is not as easily saturated as with a Gaussian smooth beam, which can be seen in a diffraction pattern from a random scan position in Fig. 1.4b). By numerically backprop-

agating the probe to the focal plane, shown in Fig 1.4c), we can observe some properties of OAM beams. In terms of the amplitude profile, we see that OAM beams have a doughnut-shaped amplitude profile, while their phase ramps up in the azimuthal direction from 0 to $l \times 2\pi$. Mathematically this is described by a phase term $e^{il\phi}$, with l called the topological charge [77]. For the probe in Fig. 1.4, the topological charge is equal to 1. In Ch. 5 we extend the work of [69] by using a multi-wavelength XUV beam carrying OAM to image an object with arbitrary structures. We also compare this method of structuring with the conventional mask-based structuring.

1.4 High order harmonic generation

In the previous sections we reported several studies that deployed ptychography with XUV and SXR light. In this section we discuss the illumination source for coherent light in this spectrum. The most common technique to generate coherent XUV and SXR light is via HHG [78, 79]. HHG can be described semi-classically with the three-step model illustrated in Fig. 1.5 [80]. In HHG a strong laser field with a wavelength in the IR or the visible spectrum interacts with a non-linear medium, which is usually a noble gas. According to the three-step model, the strong electric field, in the order of $10^{14} - 10^{15}$ W/cm^2 bends the Coulomb potential of the atom of the noble gas, and electrons can escape via tunneling. The electron accelerates in the continuum, until the electric field of the drive laser changes sign. Then, the drive field applies an opposite force to the electron, which is decelerated and accelerated back towards the parent ion, provided the polarization of the drive laser is linear. If the electron recombines with the parent ion, due to its high kinetic energy it emits a photon, whose energy extends to the XUV and SXR spectrum. The maximum photon energy that can be emitted is equal to $E_{max} \approx I_p + 3.17U_p$. where E_{max} is also called the cutoff energy, I_p is the ionization potential of the atom and U_p is the ponderomotive energy, which is associated with the intensity and the wavelength of the drive field. A more accurate analysis was performed in [81] with a quantum mechanical solution, which was analytically calculated under the strong field approximation.

For half a cycle of the drive laser, the emitted photon energies are in a continuous range from I_p until the cutoff energy. However, for multi-cycle drive laser pulses, the three-step process happens twice in every cycle, leading to a pulse train of attosecond pulses with repetition rate twice the drive laser frequency. In the frequency domain, this corresponds to a frequency comb-like spectrum with the odd harmonics of the drive laser. The high harmonics are in principle generated with similar efficiency, and for this reason are called plateau harmonics.

As we mentioned earlier, diffractive imaging methods, like ptychography, require coherent light, so that we can model mathematically the propagation of the exit wave from the object plane to the detector. The spatial coherence of the high harmonics have been investigated in [83], where the authors found good spatial coherence properties of the harmonic beams, although the coherence can degrade for long drive wavelength, very high-order harmonics and high ionization

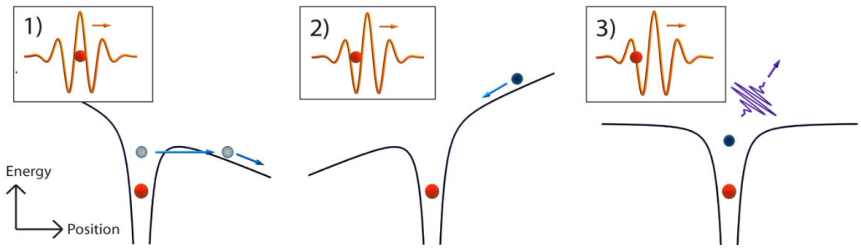

Figure 1.5: Three step model (copied from [82]). 1) The strong electric field of the drive laser bends the Coulomb potential of the atom, allowing an electron to escape via tunneling. The electron accelerates in the continuum. 2) When the electric field changes direction at the next half cycle, the electron is accelerated back towards its parent ion. 3) If the electron manages to recombine with its parent ion, it emits a photon with high energy due to its high kinetic energy.

of the gas. Furthermore, since HHG is a highly non-linear process, minor beam pointing stability issues of the drive laser can create decoherence effects of the harmonics. In terms of longitudinal coherence, the linewidth of each harmonic depends on the number of cycles within the drive laser pulse, with shorter pulses leading to broader linewidths of the harmonics. For our studies shown later in this thesis, the drive laser pulse ranges between 40 fs and 50 fs, with driving laser cycle between 2.67 fs and 3.43 fs. For this condition, we expect each harmonic to be sufficiently narrowband, so that the distance between the object and the detector is smaller than the coherence length. However, for better modelling of the propagation of an exit wave corresponding to a harmonic beam, it is recommended to use mixed states for partially coherent beams [43], which can take into consideration all the above decoherence effects.

The study of the HHG process has shown that there are two electron trajectories that lead to the emission of a photon with a particular energy below the cutoff energy. The first trajectory is called long trajectory, in which the electron has left the atom early within the drive laser cycle and has spent more time in the continuum, so by the time it reaches its parent ion and recombines, the drive laser field has changed sign again and has decelerated the electron. The other trajectory is called short trajectory and corresponds to an electron leaving late within the cycle, and eventually cannot reach the maximum kinetic energy when it is accelerated back towards the parent ion and recombines.

Each trajectory has different phase matching conditions because of different dipole phases, i.e. different phases accumulated by the electron wave packet between the time of tunneling and the time of recombination [84]. Phase matching is an important aspect of HHG, because upon interaction of the laser field with an extended non-linear medium, the maximum yield of XUV and SXR energy can be achieved when the fields generated throughout the medium add constructively [85]. In general, short trajectories have longer coherence length [84, 86],

so they are easier to phase-match and typically dominate over long trajectories. For imaging purposes, high flux is directly associated with better resolution [4]. Therefore, in all studies shown in this thesis we aimed to maximize the XUV flux by optimizing phase matching conditions for the short trajectories, which led to poor phase matching conditions for the long trajectories and thus they were ignored from further analysis. Especially in Chs. 3 and 4, where we compare experimental findings with simulations, we developed our theoretical model based on the assumption that only short trajectories are present in the reconstructed HHG beams. In fact, assuming only short trajectories in our simulation models was sufficient to explain the experimental findings.

Theoretical models for predicting the behaviour of the high harmonic beams have been studied and formulated in [87–92], based on knowledge of the drive laser properties. Although most accurate models use the time-dependent Schrödinger equation, close approximations can be achieved with the Single Atom Response (SAR) model, according to which the phase of the high harmonic wavefront with harmonic order q at the generation plane can be written as $\Phi_q = q\phi + \Phi_d$, with ϕ the phase of the fundamental beam and Φ_d the dipole phase. The dipole phase is associated with the intensity I of the drive laser. Particularly for the short trajectories, which are of interest for the work presented in the thesis, there are various models to describe the dipole phase as a function of the drive laser intensity. In [87–90] the authors derive a model of the form $\Phi_d \propto \alpha I$. However, in our works we adopt the model from [91, 92], according to which $\Phi_d \propto \gamma/I$, which we have used in Chs. 3 and 4 and is in close agreement with our experimental results. In terms of the amplitude of the high harmonics, it is shown that in the non-perturbative regime all harmonics are generated with an amplitude that is proportional to the amplitude of the driving laser to the power p [93], with common values for p being $p = 4$ [92] and $p = 3.4$ [94].

The SAR model is an insightful tool for predicting the properties of the high harmonic beams in terms of amplitude profile, phase and propagation behavior. First demonstrations of HHG were with a Gaussian drive laser that produced Gaussian high harmonic beams. However, more exotic drive beams than just Gaussian have been used as well. One such example is a beam carrying OAM, which, as we mentioned in the previous section, is also interesting for ptychographic imaging purposes. The SAR model suggests that the topological charge is upconverted to the high harmonics proportionally to the harmonic order, while further analysis based on the same model predicts that all harmonics propagate to the far field with similar divergence [95]. An example of this upconversion is shown in Fig. 1.6, where we show how a doughnut-shaped fundamental beam with topological charge equal to 1 generates doughnut-shaped high harmonics with topological charge proportional to the harmonic order. Therefore, starting with a low-topological charge input fundamental beam, we can generate a polychromatic XUV pulse with high topological charges. In the time domain the resulting attosecond pulse (or pulse train) has a helical structure also known as a spatiotemporal light spring [96].

In Ch. 4 we investigate how changes in the generation conditions and properties of the drive OAM beam influence the OAM and the propagation behavior of the

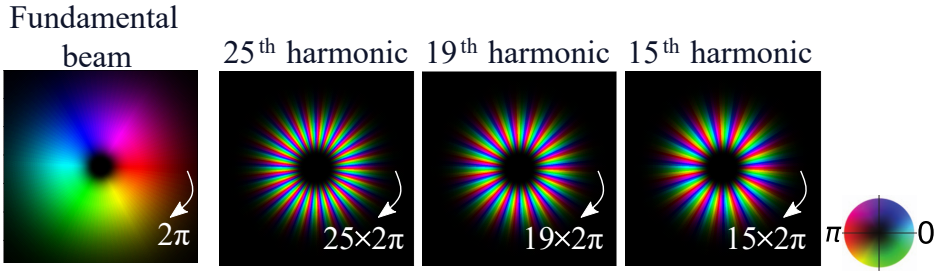

Figure 1.6: Upconversion of topological charge during HHG. For simplicity, the intensity-dependent dipole phase is omitted from the modelled high harmonic wavefronts, as it only adds a local divergence in the phase and does not contribute to the topological charge.

high harmonics, and, eventually, the shape of the attosecond light spring. Here we should note an important distinction between the topological charge and the OAM. Topological charge is the number l in the phase term $e^{il\phi}$ of an OAM beam, and is defined as $l = {}^1/_{2\pi} \oint_C d\phi$ [97]. OAM, on the other hand, describes the angular momentum that will apply a force to a particle positioned in the beam, and is strongly dependent on where in the beam it is measured. For circular beams, it can be calculated as the Fourier Transform of the complex electric field along a circular loop [98] and the result is a range of modal content of OAM.

1.5 Multi-wavelength ptychography with XUV illumination

When performing ptychography experiments with XUV HHG beams, some additional aspects should be considered. Firstly, we discussed in the previous section the coherence properties of a single harmonic beam. However, typically in the HHG process we generate 7 to 11 harmonics which we cannot treat as one coherent beam, as the coherence length ξ_l is very short and violates the coherence condition $\xi_l > PLD$ [99], with PLD the path length difference between two rays starting from the opposite edges of the beam and diffracting at the highest angle that can be captured by the detector.

A simple way to get a coherent beam from HHG is to isolate one harmonic beam and filter out all other harmonics. This solution has been implemented and presented, among others, in [33, 35, 36, 38–40, 69] using narrowband optics for refocusing and spectral selection. However, for very high harmonics and long drive wavelength the harmonic wavelengths are very close and a single harmonic cannot be easily isolated, as noted in [39, 40]. Furthermore, by filtering out harmonics, all the energy of these harmonics is lost, reducing the available flux for the ptychographic measurement. Finally, by cropping the XUV and SXR

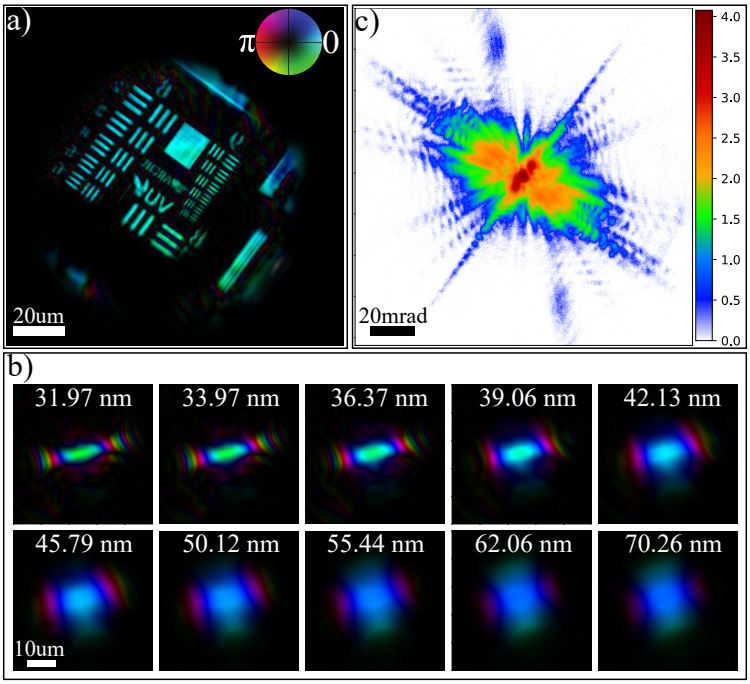

Figure 1.7: Ptychography reconstruction with a multi-wavelength HHG beam. a) Reconstructed object, b) reconstructed probe, with 10 harmonic wavelengths in the beam ranging from 15^{th} (70.26 nm) to 33^{rd} (31.97 nm) harmonic. The drive laser wavelength is centered around 1030 nm. In a) and b) brightness indicates the amplitude and hue the phase. c) Diffraction pattern from the center of the object, in logarithmic scale. We can observe the distinct signal from each wavelength in the first-order diffraction towards the edges of the detector.

spectral range of the illumination source, we cannot perform spectrally-resolved imaging where we can make use of the absorption edges of different elements.

Throughout this thesis we perform HHG ptychographic measurements using a polychromatic source and implementing multi-wavelength ptychography [44]. The ptychographic algorithm for treating multiple wavelengths in the probe is similar to mixed states [43], where we decompose the probe into an incoherent set of modes. In contrast to the mixed states, the incoherent modes in multi-wavelength ptychography have a physical meaning, as each mode corresponds to a specific harmonic wavefront. These modes are treated independently in terms of illumination of the object and propagation to the detector. At the detector plane, the diffraction patterns from each wavelength are added incoherently and the sum is compared to the measured diffraction pattern. In [44] it has been demonstrated that it is possible to reconstruct multiple probes and objects from the polychromatic diffraction patterns; however, as the number of unknown parameters increases, the increased complexity of the phase retrieval problem often requires higher overlap between scan positions or prior knowledge of the probes

or the objects.

An example from an experimental dataset of HHG multi-wavelength ptychography is shown in Fig. 1.7. The object is a home-built non-dispersive binary USAF 1951 resolution target, which has a common transmission function for all wavelengths, and it is illuminated by a 10-wavelength Gaussian probe. In Figs. 1.7a) and b) we present object and probe reconstructions respectively. In Fig. 1.7c) we show a diffraction pattern from illuminating the center of the object, where we can observe once again that for this type of illumination the energy of the diffracted signal is concentrated at the center of the detector. For multi-wavelength measurements this effect renders the ptychographic reconstruction even harder, because the zeroth order diffraction behavior is quite similar for all wavelengths, while in higher diffraction angles the contribution of each wavelength is more distinct. The diversity of the individual monochromatic diffraction patterns within a polychromatic diffraction pattern is a property that can enhance the imaging quality. This is further discussed in Ch. 5, where we compare the reconstructions of multi-wavelength ptychographic measurements for smooth and structured illumination. As structured illumination, we use beam structuring via diffraction from a mask and OAM-driven HHG. The latter is of particular interest, as there is inherent spectral diversity in the probes, shown in Fig. 1.6, which can potentially lead to increased diversity in the monochromatic diffraction patterns as well.

Recently, a ptychographic scheme with two coherent pulses was presented in [100]. This technique works similar to CDI combined with FTS [18, 20–22], where the second pulse is delayed with respect to the first pulse, leading to interference fringes on the diffraction pattern, the positions of which are a function of the delay τ between the two pulses. By changing τ at each scan position we encode spectral information in the diffraction patterns in the form of the fringes, which can allow an AD-based reconstruction algorithm to reconstruct spectrally-resolved images of the objects and probes with increased robustness.

1.6 High harmonic generation drive sources at ARCNL

In Section 1.4 we mentioned that a necessary condition for HHG to be initiated is that the drive laser power density is in the order $10^{14} - 10^{15}$ W/cm^2. Such levels of power density are typically achieved by focusing tightly an ultrashort pulse with pulse energy equal to a few mJ. For the works shown in this thesis, the HHG-related measurements were performed at ARCNL, where we have switched from a home-built Ti:Sa [101] seeded source to a commercial Yb:KGW laser. The Ti:Sa laser has been used for the measurements presented in Ch. 3, whereas the experimental results presented in Chs. 4 and 5 were acquired with the Yb:KGW laser as drive laser source.

The Ti:Sa laser can provide ultrashort pulses of 20 fs pulse duration, spanning a spectrum from 700 nm to 900nm, but the pulse energy is low. Therefore, the output of the Ti:Sa oscillator was used as seed in an amplification stage, after

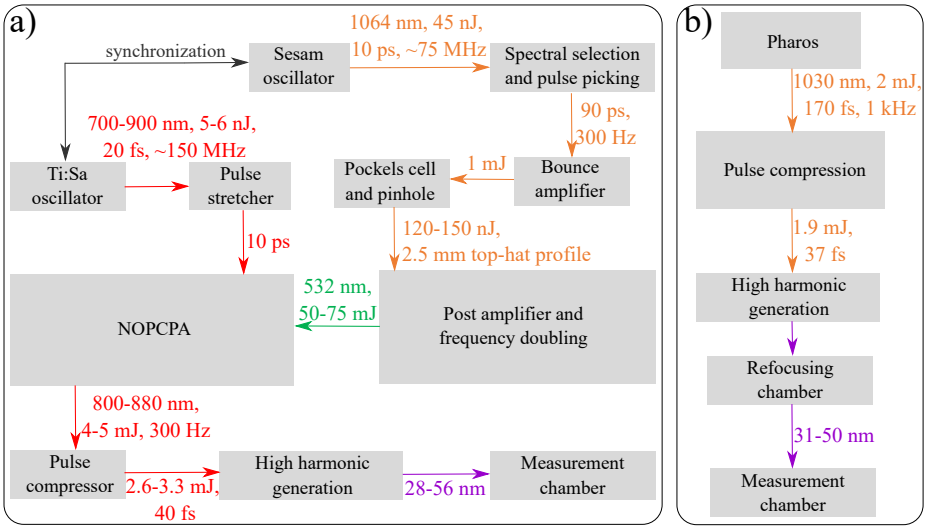

Figure 1.8: Schematic of the two setups to generate high harmonics. a) Old setup based on Ti:Sa seed beam amplified in a NOPCPA. b) New setup based on Yb:KGW commercial laser (Pharos) and a pulse compression scheme. In the new setup we also installed a refocusing chamber in the XUV part, so that we can perform ptychography measurements with a smaller beam size.

which the pulse energy was increased to 4-5 mJ. The full scheme is presented in Fig. 1.8a). Firstly, the output pulses of the Ti:Sa oscillator were stretched, such that they could be amplified to the mJ level without damaging the optics and the non-linear crystals at the amplification stage. Then, they were amplified in a non-collinear optical parametric chirped pulse amplification (NOPCPA) [102, 103] module by a pump beam. Details of the pump beam are given in Fig. 1.8a), as well as in [82, 104]. After the NOPCPA, the pulses were compressed with a pair of gratings to a pulse duration of approximately 40 fs at pulse energies 2.6-3.3 mJ. The pulses were finally sent for HHG, where we could typically generate harmonics in the range 28-56 nm, which corresponds to harmonics 29-15.

The advantages of this laser system are, among others, the high pulse energies, accessibility of every module of the (home-built) seed and pump lasers, short drive wavelength, compared to the Yb-KGW laser, which helps with HHG efficiency and spatial coherence, and more separated harmonics, which helps with multi-wavelength reconstructions. However, the complexity of this system was high, and there were beam-pointing and energy-stability issues, long warm-up times, and needs for frequent alignment of the NOPCPA. In fact, the capabilities of this laser system were beyond the 3.3 mJ pulse energy at the gas jet, as 10 mJ pulse energy for the same system has been reported in [82]. The reduced output power that we achieved during the measurements associated to Ch. 3 was due to the challenging and tedious task of alignment of the NOPCPA and due to aging of the equipment. Finally, there is a big space requirement for all these

modules shown in Fig. 1.8a), and they covered almost entirely an optical table with dimensions approximately 6 m×1.5 m.

At the end of 2022 we acquired a commercial Yb-KGW laser (Pharos from Light Conversion), which delivers 2 mJ pulses with 170 fs FWHM. The central wavelength of the laser is at 1030 nm. As the pulse energy is already at a sufficient level, we only needed to implement a pulse compression system. The compression system was based on the CASCADE concept [105], which includes long gas cells where the beams are loosely focused. This loose focusing leads to sufficient spectrum broadening, via self-phase modulation [106], while suppressing self-focusing [106], which is associated to degradation of the beam quality. After each pass through a gas cell, we use chirped mirrors with negative group delay dispersion [106] to compress the pulses. The modules of the new setup are shown in Fig. 1.8b). The pulse duration after two passes through gas cells was measured via a FROG measurement [107] equal to 35 fs. More details about the technique and the beam characterization can be found in [108]. In the new setup we also introduced refocusing XUV mirrors after the HHG chamber, such that ptychography measurements are facilitated with a smaller beam size. The resulting spectrum of the XUV illumination is shaped by the spectral efficiency of the XUV mirrors. For the projects described in Chs. 4 and 5, the XUV spectrum was in the range 31-50 nm (harmonics 33-21).

The new setup is more compact, as the dimensions of Pharos is approximately 80 cm×42 cm, although still much space in the optical table is used for the long gas cells in the spectrum broadening part. The entire setup is easier to build and maintain, compared to the older setup, and the laser beam is more stable in terms of both pointing instability and energy fluctuation. However, the laser pulse energy has a maximum level of 2 mJ, which, for some applications, such as interferometric measurements, may not be sufficient. Also, the longer drive wavelength leads to lower conversion efficiency for the HHG, lower spatial coherence of the high harmonics, and more harmonics within a specific spectral window.

1.7 Structure of this thesis

The thesis is structured as follows: In Ch. 2, we derive and compare analytical propagation models that are suitable for multi-wavelength beam configurations. In Ch. 3, we perform WFS measurements of Gaussian HHG beams, where we vary the drive laser focus position with respect to the generation plane, and study chromatic aberration effects. Ch. 4 is also about WFS measurements, but for HHG beams with non-zero OAM. Specifically, we study the effects on OAM HHG beams when we vary the drive laser focus position and introduce drive laser aberrations. Finally, in Ch. 5, we study how structured illumination for multi-wavelength HHG beams improves imaging quality and demonstrate it with two types of structured beams: HHG beams driven by a laser beam carrying OAM, and HHG beams structured via diffraction from a binary mask. We associate the improved imaging with increased diversity in the diffraction patterns.

Chapter 2

Optical propagators with user-defined object-plane pixel size for ptychography

Lensless imaging techniques have been developed to visualize objects with high robustness and unprecedented resolution. Lensless imaging is based on the numerical reconstruction of the transmission or reflection function of a sample from optical diffraction measurements. Specifically, coherent diffractive imaging (CDI) and ptychography involve an iterative process of numerical propagation of coherent light waves between the sample and detector plane. However, in the standard propagation models the pixel size of the reconstructed object image is typically fixed and wavelength-dependent, which limits CDI and broadband ptychography. Here we investigate three propagation models for far-field propagation that allow user-defined pixel size at the object plane. These propagators are the two-step Fresnel, scaled angular spectrum, and chirp-Z transform. We derive their analytical expressions and observe that all three models are mathematically equivalent, although they have a different physical origin. Each propagator can be written in two distinct versions, which conceptually represent propagation via different intermediate planes. We perform propagation simulations and ptychographic reconstructions on experimental data to compare the performance of these two different versions. Our results show that the choice of intermediate plane can affect the reconstruction quality due to different sampling bandwidth requirements, which enables a wider choice of pixel sizes in the object plane. Our analysis provides guidelines for selecting an optimized object pixel size when performing reconstructions on broadband CDI and ptychography data.

The content of this chapter has been published as: Antonios Pelekanidis, Kjeld S. E. Eikema, and Stefan Witte, *Far-field optical propagators with user-defined object-plane pixel size for ptychography,* Opt. Continuum **4**(4), 804–825 (2025).

2.1 Introduction

Lensless imaging techniques have been studied and developed extensively over the last decades. Among the lensless techniques, ptychography [23, 24] has distinguished itself as a robust coherent diffractive imaging (CDI) method. In CDI, the object of interest is illuminated by a laser beam, typically referred to as the probe, and diffracts the light towards an imaging detector. Because the detector can only capture the intensity of the diffraction pattern, the phase of the diffracted field must be algorithmically calculated. Specifically in ptychography, the phase problem is addressed by moving the object laterally to the laser beam, so that the detector captures the diffraction patterns from multiple object positions sequentially. Each position has significant overlap with the adjacent positions and the abundance of the captured diffraction data allows the ptychographic algorithm to reconstruct complex-valued expressions of both the object and the probe.

Ptychographic imaging has been explored with monochromatic coherent light in a broad range of wavelengths from infrared [70] to X-ray [28], and diffraction-limited imaging resolution [3] has been demonstrated. In its most basic form, the pixel size dx of the reconstructed object image in CDI is equal to the diffraction limit $dx = \lambda/2NA$, where λ is the wavelength of the radiation and NA is the numerical aperture of the measurement setup.. Thus, the object image pixel size is both fixed and wavelength dependent. This fixed number for the pixel size comes from the most commonly used models based on Fraunhofer and Fresnel propagation [5]. However, various applications require broadband illumination, such as white visible light [109] or multi-wavelength extreme ultraviolet (XUV) light generated via high harmonic generation (HHG) [31, 34]. Specifically, ptychography with HHG radiation has attracted great interest, because of its potential for nanometer-resolution microscopy with tabletop sources for semiconductor metrology [35, 38] and biomedical applications [36].

For ptychography with non-monochromatic illumination, a typical way to model the probe is as a set of incoherent modes, with each mode corresponding to a different wavelength [44]. The exit wave for each mode is propagated independently to the detector and at the detector plane the monochromatic diffracted signals are added incoherently and compared to the measured diffraction pattern. Since each wavelength is treated independently, we can apply monochromatic propagation for each wavelength separately using the standard propagation models. However, in this case the pixel size at the object plane will be different for each wavelength. In many cases, it is necessary to have the same pixel size for all wavelengths, as we can apply constraints based on prior knowledge, such as a coupling constraint between the object reconstructions for adjacent wavelengths [110]. For some applications, the object can be entirely non-dispersive, e.g. in the ptychographic measurements with multi-wavelength HHG beams demonstrated in [37, 63, 111]. In these examples the object was binary, either for imaging or wavefront-sensing purposes, and the complexity of the reconstruction problem was reduced extensively.

A simple approach for multi-wavelength wave propagation is to select the well-known angular spectrum propagator (ASP) [5], which is accurate, easy to imple-

ment and fast to compute, as it requires only two Fourier transforms. In ASP, the pixel sizes at the source plane and the observation plane are fixed and equal, irrespective of the wavelength. However, for far-field diffraction, the ASP transfer function suffers from aliasing [112]. Furthermore, the pixel size of the detector is usually larger than the diffraction limited resolution [113], therefore, the reconstructed object and probe are sampled with a coarser pixel size compared to the resolution capabilities of the imaging system.

This pixel size limitation can be mitigated by reverting to propagation models that allow the user to define the pixel size at the object plane. For example, the authors of [112, 114] propose such propagation models using non-uniform fast Fourier transforms [115]. Another solution includes zero-padding the space of the input field [116]. Similarly, Yu *et al.* developed a propagation model with an increased calculation window while performing linear convolutions to mitigate the computational burden [117]. Asoubar *et al.* investigated more elaborate operators requiring an additional Fourier transform compared to the standard ASP, in order to increase accuracy for non-paraxial diffraction [118]. More recently, a scalable angular spectrum propagator was proposed also for more accurate propagation in near-field conditions, again at the computational expense of three Fourier transforms [113].

In this paper we focus on three models that are simple conceptually and relatively fast, as they operate under the paraxial approximation and require two Fourier transforms. These models are the two-step Fresnel propagation (2SF) [119, 120], the scaled angular spectrum propagation (sASP) as introduced in [120] and the chirp-Z transform (CZT) as introduced and implemented in [40, 121, 122]. These models have been mostly presented separately in earlier works [119–122], and each has a different physical interpretation. Therefore, there may be a misconception that these models differ in their mathematical formulations, potentially leading to different performance in the ptychographic reconstruction context. To validate the equivalence of the models, we first derive the equations that describe the propagation of the electromagnetic wave from the object plane to the observation plane for each model. From the mathematical descriptions we conclude that all three of them are identical; however, they can be expressed in two versions, which, as we shall see for the 2SF propagator has a physical interpretation as propagation in different intermediate planes. We denote these versions as "+" and "−", because of a distinct sign difference within the mathematical expressions. We subsequently compare the two versions with the commonly used (one-step) Fresnel propagator by calculating the correlation of simulated diffraction patterns. Finally, we test the propagators on experimental ptychographic data, where we vary the pixel size at the object plane. The reconstruction results confirm that bandwidth limitations of the propagators affect the imaging quality, although the effect is mainly apparent for very high and very low magnification ratios between object and detector planes. However, this deterioration of the imaging quality can be mitigated by zero padding the exit wave at the sample plane before propagating to the detector.

2.2 Analytical expressions of the propagation models

The following analysis is based on [120], where we assume that we know the electric field $U(x_1, y_1)$ at a source plane 1, with x_1, y_1 the spatial coordinates of this plane. Then, the electric field $U(x_2, y_2)$ at an observation plane 2, with x_2, y_2 the coordinates at this plane, is given by the Fresnel integral,

$$U(x_2, y_2) = \frac{e^{ikz}}{i\lambda z} \int_{-\infty}^{\infty} \int_{-\infty}^{\infty} U(x_1, y_1) e^{i\frac{k}{2z}[(x_1-x_2)^2+(y_1-y_2)^2]} dx_1 dy_1 \tag{2.1}$$

In Eq. (2.1), k is the propagation constant of the electromagnetic wave, $\lambda = {}^{2\pi}/_{k}$ is the wavelength, i is the imaginary unit and z is the distance between planes 1 and 2. This equation describes the propagation of any scalar monochromatic electromagnetic wave under the paraxial approximation [5, 120]. In case of a multi-wavelength beam, the intensity at any plane is given by the incoherent sum of the intensities for all wavelengths at that plane, $I_j = \sum_\lambda |U(\lambda, x_j, y_j)|^2$ [44]. Therefore, the forward propagation calculation presented in Eq. (2.1) can be calculated independently for each wavelength.

In discretized space, Eq. (2.1) is written as,

$$U(m_2 dq, n_2 dq) = \frac{e^{ikz}}{i\lambda z} dx^2 \sum_{m_1=-\infty}^{\infty} \sum_{n_1=-\infty}^{\infty} U(m_1 dx, n_1 dx) \cdot e^{i\frac{k}{2z}[(m_1 dx - m_2 dq)^2 + (n_1 dx - n_2 dq)^2]} \tag{2.2}$$

In the above equation dx and dq are the sizes of square pixels in planes 1 and 2 respectively, and (m_1, n_1), $(m_2, n_2) \in \mathbb{Z}$ are the discrete coordinates in planes 1 and 2.

2.2.1 One-step Fresnel propagator

In order to derive the standard one-step Fresnel propagator [5], we rewrite Eq. (2.2) as

$$U(m_2 dq, n_2 dq) = \frac{e^{ikz} dx^2}{i\lambda z} e^{i\frac{k}{2z}[(m_2 dq)^2 + (n_2 dq)^2]} \cdot \sum_{m_1=-\infty}^{\infty} \sum_{n_1=-\infty}^{\infty} \left(U(m_1 dx, n_1 dx) e^{i\frac{k}{2z}[(m_1 dx)^2 + (n_1 dx)^2]} \right) \cdot e^{-i\frac{2\pi dx dq}{\lambda z}[(m_1 m_2) + (n_1 n_2)]} \tag{2.3}$$

We assume the size of the arrays that describe the electric fields are $N \times N$. As the pixel size in plane 2 dq is set by the choice of detector, the pixel size at plane 1 can be set equal to $dx = {}^{\lambda|z|}/_{N \cdot dq}$ to simplify Eq. (2.3). The electric field at

plane 2 then becomes

$$U(m_2dq, n_2dq) = \frac{e^{ikz}dx^2}{i\lambda z} e^{i\frac{k}{2z}[(m_2dq)^2+(n_2dq)^2]} \cdot \sum_{m_1=0}^{N-1}\sum_{n_1=0}^{N-1}\left(U(m_1dx, n_1dx)e^{i\frac{k}{2z}[(m_1dx)^2+(n_1dx)^2]}\right) \cdot e^{-sign(z)i\frac{2\pi}{N}[(m_1m_2)+(n_1n_2)]}$$

This expression can be rewritten as a Fourier transform, but with a form that depends on whether the propagation is in the forward ($z > 0$) or backward ($z < 0$) direction:

$$U(m_2dq, n_2dq) = \frac{e^{ikz}dx^2}{i\lambda z} e^{i\frac{k}{2z}[(m_2dq)^2+(n_2dq)^2]} N \cdot \mathscr{F}\left\{U(m_1dx, n_1dx)e^{i\frac{k}{2z}[(m_1dx)^2+(n_1dx)^2]}\right\} \quad (2.4)$$

if $z > 0$ and

$$U(m_2dq, n_2dq) = \frac{e^{ikz}dx^2}{i\lambda z} e^{i\frac{k}{2z}[(m_2dq)^2+(n_2dq)^2]} N \cdot \mathscr{F}^{-1}\left\{U(m_1dx, n_1dx)e^{i\frac{k}{2z}[(m_1dx)^2+(n_1dx)^2]}\right\}$$

if $z < 0$. By $\mathscr{F}^{(-1)}$ we denote the two-dimensional normalized (inverse) Discrete Fourier Transform (DFT). Equation (2.4) is a convenient formula in order to computationally calculate the electric field at plane 2. In case of very large z, $e^{ik/2z[(m_1dx)^2+(n_1dx)^2}} \approx 1$ in Eq. (2.4) and the propagation from plane 1 to plane 2 is written as

$$U(m_2dq, n_2dq) = \frac{e^{ikz}dx^2}{i\lambda z} e^{i\frac{k}{2z}[(m_2dq)^2+(n_2dq)^2]} N \cdot \mathscr{F}^{(-1)}\left\{U(m_1dx, n_1dx)\right\} \quad (2.5)$$

which is known as the Fraunhofer propagation model [123].

As mentioned earlier, the one-step Fresnel propagator in the expression of Eq. (2.4) is valid only for a specific, wavelength-dependent pixel size at plane 1, determined by the detection geometry. However, in multi-wavelength ptychography it is often desirable to have a ratio between the pixel sizes $m = {}^{dq}/_{dx}$ that is both adjustable and independent of the wavelength. The propagation models 2SF, sASP and CZT accomplish that by rewriting Eq. (2.2) accordingly, each based on a specific interpretation of the equations.

2.2.2 Two-step Fresnel propagator

For the 2SF propagator, we define an intermediate plane 1a at distance z_1 from plane 1, as shown in Fig. 2.1. First we propagate the electromagnetic field from

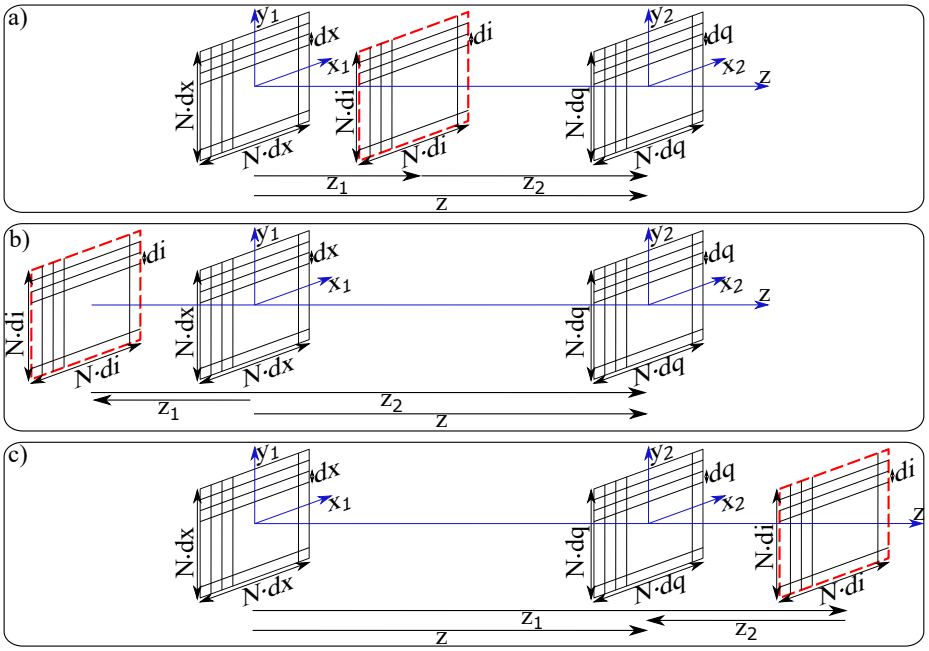

Figure 2.1: The two-step Fresnel propagator concept. A first numerical propagation step is performed to an intermediate plane at a distance z_1 (indicated by the red frame), from which a second step is taken towards the final (detector) plane over distance z_2, with $z = z_1 + z_2$. This intermediate plane can be: a) in between the object and detector planes (both z_1 and z_2 positive), with $z_1 = z \cdot {}^{1}/_{1+m}$ and $z_2 = z \cdot {}^{m}/_{1+m}$, b) behind the object plane (negative z_1), with $z_1 = z \cdot {}^{1}/_{1-m}$, $z_2 = z \cdot {}^{-m}/_{1-m}$ and $m > 1$, or c) beyond the detector plane (negative z_2), with $z_1 = z \cdot {}^{1}/_{1-m}$, $z_2 = z \cdot {}^{-m}/_{1-m}$ and $m < 1$.

plane 1 to a plane 1a using Eq. (2.4). The pixel size at plane 1a is $di = {}^{\lambda|z_1|}/_{N\,dx}$. Next, we propagate the electromagnetic field from plane 1a to plane 2, also using Eq. (2.4). The distance between plane 1a and plane 2 is $z_2 = z - z_1$. From this propagation, we find a second equation for the pixel size at plane 1a, $di = {}^{\lambda|z_2|}/_{N\,dq}$. As the position of the intermediate plane can be freely chosen, this 2SF approach gives the ability to adjust the final pixel size in the object plane. For a given magnification ratio $m = {}^{dq}/_{dx}$, there are actually two possible planes 1a that satisfy the two expressions for di simultaneously, with propagation distances $z_1 = z \cdot {}^{1}/_{1\pm m}$ and $z_2 = z \cdot {}^{\pm m}/_{1\pm m}$ [120]. It is important to realize that the intermediate plane does not have to be located in between planes 1 and 2 (which is the situation shown in Fig. 2.1a), but can also be chosen in the opposite direction (Fig. 2.1b) or at a distance larger than z (Fig. 2.1c). In the latter two cases, one of the propagation steps is in the backward direction, such that either z_1 or z_2 is negative, and requires the use of an inverse Fourier transform. Of the two possible solutions for a given m, one uses two forward propagation steps as in Fig. 2.1a, while the other solution corresponds to either Fig. 2.1b or Fig. 2.1c. We will denote these solutions as 2SF$\pm$ for using $\pm m$

respectively, with the $-m$ solution using an inverse Fourier transform in one of the steps. The full propagation from plane 1 to plane 2 can then be expressed as

$$\begin{aligned} U(m_2dq, n_2dq) = &\frac{e^{ikz_2}di^2}{i\lambda z_2} e^{i\frac{k}{2z_2}[(m_2dq)^2+(n_2dq)^2]} N \cdot \mathscr{F}^{(-1)}\Bigg\{\Big(\frac{e^{ikz_1}dx^2}{i\lambda z_1}\cdot \\ &e^{i\frac{k}{2z_1}[(m_{1a}d_i)^2+(n_{1a}d_i)^2]} N \mathscr{F}^{(-1)}\Bigg\{U(m_1dx, n_1dx)\cdot \\ &e^{i\frac{k}{2z_1}[(m_1dx)^2+(n_1dx)^2]}\Bigg\}\Big) e^{i\frac{k}{2z_2}[(m_{1a}d_i)^2+(n_{1a}d_i)^2]}\Bigg\} \end{aligned} \tag{2.6}$$

As discussed, whether forward or inverse DFT should be performed in each propagation step depends on the signs of z_1 and z_2 respectively.

We can substitute di, z_1 and z_2 with the expressions containing variables only from the initial problem statement, z, k, dx, dq and $m = {}^{dq}/_{dx}$, such that Eq. (2.6) becomes:

$$U(m_2dq, n_2dq) = C^{2SF\pm} Q_3^{2SF\pm} \mathscr{F}^{(-1)}\Bigg\{\mathscr{F}^{(-1)}\Bigg\{U(m_1dx, n_1dx) Q_1^{2SF\pm}\Bigg\} Q_2^{2SF\pm}\Bigg\} \tag{2.7}$$

where

$$C^{2SF\pm} = \frac{e^{ikz}}{\mp m} \tag{2.8}$$

$$Q_1^{2SF\pm} = e^{i\frac{k(1\pm m)}{2z}[(m_1dx)^2+(n_1dx)^2]} \tag{2.9}$$

$$Q_2^{2SF\pm} = e^{\pm i\frac{2\pi^2 z}{mk}\left((\frac{m_{1a}}{Ndx})^2+(\frac{n_{1a}}{Ndx})^2\right)} \tag{2.10}$$

$$Q_3^{2SF\pm} = e^{i\frac{k(1\pm m)}{\pm 2zm}[(m_2dq)^2+(n_2dq)^2]} \tag{2.11}$$

Detailed explanation of the derivation of Eq. (2.7) from Eq. (2.6) is given in Appendix 2.6.1. To clarify whether forward or inverse DFT should be used, it can be instructive to rewrite Eq. (2.7), considering the symmetry of Q_2 around $(m_{1a}, n_{1a}) = (0, 0)$, according to the derivation shown in Appendix 2.6.4:

$$U(m_2dq, n_2dq) = C^{2SF\pm} Q_3^{2SF\pm} \mathscr{F}^{-1}\Bigg\{\mathscr{F}^{\mp 1}\Bigg\{U(m_1dx, n_1dx) Q_1^{2SF\pm}\Bigg\} Q_2^{2SF\pm}\Bigg\} \tag{2.12}$$

where 2SF+ describes the schematic of Fig. 2.1a) and 2SF− the schematic of both Figs. 2.1b) and 2.1c). In this expression, we use $\mathscr{F}^{+1}$ to explicitly denote the forward Fourier transform.

2.2.3 Scaled angular spectrum propagator

The sASP model also starts from the Fresnel integral in Eq. (2.1). In the sASP model, the desired magnification ratio m is introduced directly into the Fresnel

equation by scaling the detector plane variables accordingly. This can be achieved by rewriting the exponential function inside the integral of Eq. (2.1) with the introduction of m in the equation as [120]

$$\begin{aligned} e^{i\frac{k}{2z}[(x_1-x_2)^2+(y_1-y_2)^2]} &= e^{i\frac{k}{2z}|\boldsymbol{r_1}-\boldsymbol{r_2}|^2} \\ &= e^{i\frac{k}{2z}\left(\pm m|\frac{\boldsymbol{r_2}}{m}\mp\boldsymbol{r_1}|^2\mp\left(\frac{1\mp m}{m}\right)r_2^2+(1\mp m)r_1^2\right)} \end{aligned}$$

Note that also in this model, there are two possible solutions corresponding to $\pm m$ that are both mathematically correct. After rearranging the terms and setting the new scaled variables $\boldsymbol{r_2'} = \boldsymbol{r_2}/m$ and $z' = z/m$, Eq. (2.1) is written as

$$\begin{aligned} U(m\boldsymbol{r_2'}) = &\frac{e^{ikz}e^{\mp i\frac{k}{2z'}(1\mp m)(r_2')^2}}{i\lambda z'} \\ &\int_{-\infty}^{\infty}\left(\frac{1}{m}U(\boldsymbol{r_1})e^{i\frac{k}{2z}(1\mp m)(r_1)^2}\right)\left(e^{\pm i\frac{k}{2z'}(\boldsymbol{r_2'}\mp\boldsymbol{r_1})^2}\right)d\boldsymbol{r_1} \\ = &\frac{e^{ikz}e^{\mp i\frac{k}{2z'}(1\mp m)(r_2')^2}}{i\lambda z'}\int_{-\infty}^{\infty}U''(\pm\boldsymbol{r_1})h(\boldsymbol{r_2'}-\boldsymbol{r_1})d\boldsymbol{r_1} \end{aligned} \tag{2.13}$$

This equation shows that the electric field at plane 2 can be expressed as a convolution between a modified input electric field at plane 1 $U''(\pm\boldsymbol{r_1})$ and a transfer function $h(\boldsymbol{r_1}) = e^{\pm ik/2z'(r_1)^2}$. The convolution is replaced by a product in the reciprocal domain, so the electric field at plane 2 can be written as

$$\begin{aligned} U(m_2dq, n_2dq) = &\frac{e^{ikz}dx^2e^{\mp i\frac{k}{2z'}(1\mp m)\frac{(m_2dq)^2+(n_2dq)^2}{m^2}}}{i\lambda z'}\cdot \\ &\mathscr{F}^{-1}\left\{\mathscr{F}\left\{U''(\pm m_1dx, \pm n_1dx)\right\}\cdot\mathscr{F}\left\{h(m_1dx, n_1dx)\right\}\right\} \end{aligned}$$

We can use the property that $\mathscr{F}\{f(-x)\} = \mathscr{F}^{-1}\{f(x)\}$, which then leads to the expression

$$\begin{aligned} U(m_2dq, n_2dq) = &\frac{e^{ikz}dx^2e^{\mp i\frac{k}{2z'}(1\mp m)\frac{(m_2dq)^2+(n_2dq)^2}{m^2}}}{i\lambda z'}\cdot \\ &\mathscr{F}^{-1}\left\{\mathscr{F}^{\pm 1}\left\{U''(m_1dx, n_1dx)\right\}\cdot\mathscr{F}\left\{h(m_1dx, n_1dx)\right\}\right\} \end{aligned} \tag{2.14}$$

In Eq. (2.14) we have already expressed the fields in the discretized space coordinates, where the Fourier transform is implemented as DFT. Here we should note that the convolution with a transfer function using the DFT is a circular convolution [124], therefore we need to convert it into a linear convolution for Eq. (2.14) to make it equivalent to Eq. (2.13). This conversion can be made by doubling the array sizes of the fields and pad them with zeros [124]. Then the

field at the destination plane, which has the same (increased) size as the measurement plane will have to be truncated accordingly, according to [124], to the original dimensions.

Equation (2.14) is valid for any magnification ratio m. It can be further elaborated to get a fully analytical expression and can be compacted by introducing auxiliary phase functions, similar to Eqs. (2.9-2.11) for the 2SF propagator, with a detailed derivation given in Appendix 2.6.2. Following this analysis, Eq. (2.14) then becomes

$$U(m_2dq, n_2dq) = C^{sASP\mp} Q_3^{sASP\mp} \cdot \mathscr{F}^{-1}\left\{ \mathscr{F}^{\pm 1}\left\{ U(m_1dx, n_1dx) Q_1^{sASP\mp} \right\} Q_2^{sASP\mp} \right\} \tag{2.15}$$

where

$$C^{sASP\mp} = \frac{e^{ikz} dx^2}{i\lambda z}\left(\frac{1}{2} \pm \frac{i}{2}\right)\sqrt{\frac{2z}{km}} = \frac{e^{ikz} dx^2}{\sqrt{\lambda z \pi m}}\left(\pm\frac{1}{2} - \frac{i}{2}\right) \tag{2.16}$$

$$Q_1^{sASP\mp} = e^{i\frac{k}{2z}(1\mp m)\left((m_1dx)^2 + (n_1dx)^2\right)} \tag{2.17}$$

$$Q_2^{sASP\mp} = e^{\mp i\frac{2\pi^2 z}{km}\left(\left(\frac{m_f}{Ndx}\right)^2 + \left(\frac{n_f}{Ndx}\right)^2\right)} \tag{2.18}$$

$$Q_3^{sASP\mp} = e^{\mp i\frac{k}{2z}(1\mp m)\frac{(m_2dq)^2 + (n_2dq)^2}{m}} \tag{2.19}$$

2.2.4 Chirp-Z transform propagator

The chirp-Z transform (CZT) is a generalization of the discrete Fourier transform that allows for fast calculations of z-transforms of the form $X_k = \sum_{n=0}^{N-1} x_n A^{-n} W^{nk}$, with A and W arbitrary complex numbers that satisfy the expressions $A = A_0 e^{i2\pi\theta_0}$ and $W = W_0 e^{i2\pi\phi_0}$ [125]. While the main application of the CZT is to map signals onto tailored frequency spaces, an additional benefit is that a magnification ratio m between the pixel sizes in different planes can be introduced in a similar way as for the sASP model. This approach follows the work performed in [122]. The CZT approach starts from Eq. (2.3), and the main step is the introduction of the identities $m_1m_2 = \pm m_1^2/2 \pm m_2^2/2 \mp (m_1 \mp m_2)^2/2$ and $n_1n_2 = \pm n_1^2/2 \pm n_2^2/2 \mp (n_1 \mp n_2)^2/2$. These products can be introduced into the Fourier transform phase factor, so that Eq. (2.3) is then written as

$$U(m_2dq, n_2dq) = \frac{e^{ikz} dx^2}{i\lambda z} e^{i\frac{k}{2z}[(m_2dq)^2 + (n_2dq)^2]} \cdot \sum_{m_1=-\infty}^{\infty} \sum_{n_1=-\infty}^{\infty} U(m_1dx, n_1dx) e^{i\frac{k}{2z}[(m_1dx)^2 + (n_1dx)^2]} \cdot e^{-i\frac{2\pi dx dq}{\lambda z}\left[\left(\frac{\pm m_1^2}{2} \pm \frac{m_2^2}{2} \mp \frac{(m_1 \mp m_2)^2}{2}\right) + \left(\pm\frac{n_1^2}{2} \pm \frac{n_2^2}{2} \mp \frac{(n_1 \mp n_2)^2}{2}\right)\right]} \tag{2.20}$$

The exponent in the last term of Eq. (2.20) can be expanded and worked further, with detailed calculations in Appendix 2.6.3. The final expression for the CZT propagator is the following:

$$U(m_2dq, n_2dq) = \frac{e^{ikz}dx^2}{i\lambda z} Q_3^{CZT\mp} \mathscr{F}^{-1}\left\{ \mathscr{F}^{\pm 1}\left\{ U(m_1dx, n_1dx) Q_1^{CZT\mp} \right\} Q_2^{CZT\mp} \right\} \tag{2.21}$$

where

$$Q_1^{CZT\mp} = e^{i\frac{k}{2z}[(m_1dx)^2+(n_1dx)^2]} e^{\mp i\frac{kmdx^2}{z}(\frac{m_1^2}{2}+\frac{n_1^2}{2})} = e^{i\frac{k}{2z}\left((m_1dx)^2+(n_1dx)^2\right)(1\mp m)} \tag{2.22}$$

$$Q_2^{CZT\mp} = \mathscr{F}\left\{ e^{\pm i\frac{kmdx^2}{z}(\frac{m_1^2}{2}+\frac{n_1^2}{2})} \right\} \tag{2.23}$$

$$Q_3^{CZT\mp} = e^{i\frac{k}{2z}[(m_2dq)^2+(n_2dq)^2]} e^{\mp i\frac{kdq^2}{zm}(\frac{m_2^2}{2}+\frac{n_2^2}{2})} = e^{i\frac{k}{2z}\left((m_2dq)^2+(n_2dq)^2\right)(1\mp\frac{1}{m})} \tag{2.24}$$

By comparing Eqs. (2.21-2.24) with Eqs. (2.29-2.32) of the sASP model, it can be seen that the expressions of the sASP and the CZT propagators are actually identical. This is an interesting observation, as the models have a different physical motivation, but result in the same mathematical expression. Because of this equivalence, we will only consider the 2SF and the sASP models for further comparison in the following section.

2.2.5 Equivalence between sASP and 2SF propagators

To systematically compare the 2SF and sASP propagators we need to examine the analytical formulas of the two propagators in Eqs. (2.8-2.12) and (2.15-2.19) respectively. Firstly, we observe that the quadratic phase terms Q_1, Q_2 and Q_3 are identical for the two propagators and both $\pm$ versions. Furthermore, the sequence of performing the forward and inverse DFT operations are also identical. The only difference is in the constant term C. However, in practice, C is selected such that there is energy conservation between the two planes. Therefore, we conclude that all three propagators that have been studied in this paper are equivalent, despite the fact that conceptually they had a different starting point. Of practical importance is that each propagator has two versions that are denoted as the "+" and "−" version. Using the conceptualization used for the 2SF model and the visualization of Fig. 2.1, these two versions can be interpreted as having an intermediate plane between ("+") or outside ("−") the two planes of interest. In the rest of the paper, we will study the differences in the precision and performance of these two versions.

2.2.6 Bandwidth limits

The mathematical expressions for both versions were derived from the Fresnel integral equation, without any further assumptions or approximations. Therefore, the accuracy of the models is in principle the same. However, when working with discretized space we must ensure, according to the Nyquist theorem, that the sampling rate is at least twice the maximum frequency [126]. Alternatively, the highest frequency that can be uniquely encoded in a signal is half the sampling rate. In our analysis, the Nyquist theorem poses different limits to the highest resolvable frequencies of each auxiliary quadratic phase function, which can eventually affect the accuracy of each model.

The procedure to calculate the Nyquist frequency is based on ref. [124] and follows three steps. Firstly, we write the bandwidth-limited array that represents an auxiliary function of a model in the form $H(u;a,b) = e^{i\phi(u;a,b)}$, where u are the coordinates either in the spatial domain or the reciprocal domain. By a and b we denote other parameters such as distance and wavelength. Then, we determine the frequency of $H(u;a,b)$ by calculating the partial derivative $f_u(u;a,b) = {}^{1}/_{2\pi}\ {}^{\partial\phi}/_{\partial u}$. Finally, we write the Nyquist theorem in the form $\Delta u^{-1} \geq 2|f_u|$, where Δu is the pixel size. By solving the latter with respect to u, we can determine $u_{max} = 2|f_u|$. We apply these steps to the quadratic phase functions of both the "+" and "−" propagators. As our analysis is performed for ptychography, we will only investigate the Nyquist frequency for the terms that affect the ptychographic algorithm. Specifically, ptychography is insensitive to phase information in the detector plane, labelled as plane 2 in the previous sections. Therefore, we can ignore Q_3 and we need to check the bandwidth limits for the functions Q_1 and Q_2 only.

Both Q_1 and Q_2 have a general form $Q_j = e^{iA_j u^2}$ (with $j = 1, 2$), where A_j is a constant and $u^2 = u_1^2 + u_2^2$ with u_1, u_2 independent variables. Then

$$\begin{aligned} f_u &= \frac{1}{2\pi}\frac{\partial A_j u^2}{\partial u} = \frac{1}{2\pi} 2A_j u \\ \Delta u^{-1} \geq 2|f_u| &\Leftrightarrow \Delta u^{-1} \geq \frac{1}{\pi} 2|A_j||u| \Leftrightarrow |u| \leq \frac{\pi}{2|A_j|\Delta u} \\ u_{max} &= \frac{\pi}{2|A_j|\Delta u} \end{aligned} \tag{2.25}$$

We can apply Eq. (2.25) for each function Q_j of the Eqs. (2.9, 2.10).

Nyquist criterion for "+"

- Q_1: $A_1 = \frac{k(1+m)}{2z}$, $\Delta u = dx \longrightarrow u_{max} = \dfrac{\pi z}{k(1+m)dx}$ (2.26)

- Q_2: $A_2 = \frac{2\pi^2 z}{mk}$, $\Delta u = \frac{1}{Ndx} \longrightarrow \quad u_{max} = \dfrac{mkNdx}{4\pi z}$ (2.27)

Nyquist criterion for "−"

- Q_1: $A_1 = \frac{k(1-m)}{2z}$, $\Delta u = dx \longrightarrow u_{max} = \dfrac{\pi z}{k|1-m|dx}$ (2.28)

- Q_2: $A_2 = \frac{-2\pi^2 z}{mk}$, $\Delta u = \frac{1}{Ndx} \longrightarrow \quad u_{max} = \frac{mkNdx}{4\pi z}$

From Eqs. (2.26) and (2.28) we conclude that the "−" version of the propagators always has a less strict Nyquist limit for the Q_1 phase term, with the difference between the two versions becoming more apparent when $m \approx 1$. The Q_2 phase term has the same Nyquist limit for both versions.

Setting the Nyquist limits in the phase functions Q_1 and Q_2 has a straightforward mathematical aspect of ensuring the signals are well-sampled, but there is an implicit physical implication which has been discussed in [124]. The authors of [124] discuss a physical error associated with the bandwidth limit of the transfer function, which for the sASP case is equivalent to Q_2. This physical error emerges if the bandwidth limit of Q_2 is smaller than the maximum spatial frequency of the field at the source plane. Since Q_2 is multiplied with the Fourier transform of the field, any spatial frequencies beyond the bandwidth limit will be excluded from the propagation calculation, leading to inaccurate propagation result. Similarly for Q_1, the bandwidth limit of Q_1 needs to be larger than the radius of the beam; otherwise, the product $U \cdot Q_1$ in Eq. (2.15) will exclude parts of the field that may carry a significant part of the total energy and information. Furthermore, sharp edges in the product $U \cdot Q_1$ due to a strict bandwidth limit of Q_1 will cause artificial diffraction effects. To verify whether this physical error is present in the following simulations and experimental reconstructions, we can calculate the percentage of the input field energy that is preserved after the multiplications with Q_1 and Q_2: $\Delta E = \frac{\sum_{all\ pixels} |\mathscr{F}^{\pm 1}\{U \cdot Q_1\} Q_2|^2}{\sum_{all\ pixels} |\mathscr{F}\{U\}|^2} 100\%$.

2.3 Precision of propagation models tested on simulated diffraction data

In order to compare the different propagators, we perform a simulation in which we propagate the exit wave of a coherent light beam after it is transmitted through a binary object. The probe beam has a wavelength $\lambda = 38.25$ nm and is Gaussian-shaped with 23 µm full-width at half maximum (FWHM). We compare the "+" and "−" versions with respect to the standard one-step Fresnel, as mathematically they should be identical. For the "±" propagators we have calculated the diffraction patterns with and without zero-padding the exit waves, as the sASP and CZT indicate that zero padding is necessary, whereas the 2SF analysis does not include any convolution step that would necessitate zero padding. The difference in the diffraction patterns between zero-padded and non-zero-padded exit waves for these demonstrated propagations turns out to be very small, as is shown in Appendix 2.6.5. We attribute this small difference on the finite extent of the probe and consequently of the exit wave, compared to the field of view at the object plane. Generally, in ptychography the probe is

aimed to have a small size, so that we can satisfy the oversampling ratio criterion [42]. Specifically, for an object pixel size equal to the diffraction limit, the probe has to be of diameter $d_{probe} \leq {}^{N dx}/_{2}$ [42]. Therefore, there is typically much empty space on the frame of the exit wave, and the circular convolution is not affected strongly by wrapping artifacts. However, as shown in the next section, for a certain selection of object pixel sizes where the probe extends to the whole frame, zero-padding is indeed necessary.

The exit waves at the sample plane and the diffraction patterns are shown in Fig. 2.2. Specifically, in Fig. 2.2 we demonstrate three different cases of illumination divergence, which correspond to diffraction patterns with stronger far-field or near-field features. The flux of the exit surface wave is $7.6{\times}10^{6}$ photons. The detector is assumed to be a 2048×2048-pixel camera with pixel size equal to 13.5 µm, placed at a distance $z = 105$ mm from the object. The diffraction patterns are calculated and stored as single-precision floating point (float32) numbers. In Appendix 2.6.5 we study more examples in terms of probe divergence, as well as different object to detector distances for flat wavefront illumination.

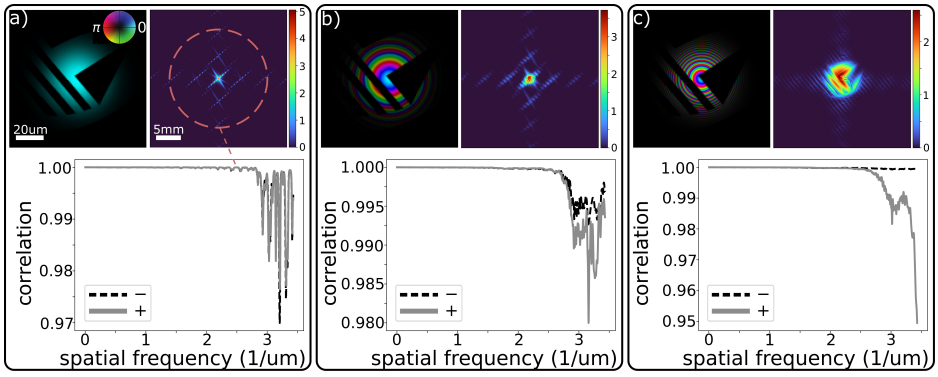

Figure 2.2: Comparison of diffraction patterns acquired for different propagators, using probes with varying radius of curvature R. a) $R = \infty$, b) $R = 7.83$ mm, c) $R = 1.88$ mm. In a-c), top left: exit wave. The brightness indicates the amplitude and the hue the phase; top right: intensity of diffraction pattern using one step Fresnel propagator at the detector plane at a distance $z = 105$ mm; bottom: correlation between diffraction patterns acquired from one step Fresnel and sASP± for different probes, as a function of spatial frequency (distance from center of detector). All subfigures share the same respective scale bars. The dashed circle indicates the spatial frequency $f = 2.5$ µm^{-1}, where the correlation starts to decrease.

In Fig. 2.2 we also show correlation results between the diffraction patterns acquired via the one-step Fresnel propagator and the sASP± propagators. The correlation is shown as a function of the radius r_2 from the center of the detector, which for far-field propagation can be interpreted as spatial frequency $f = {}^{r_2}/_{\lambda z}$. We observe that the diffraction patterns we get from either the "+" or "−" version of the sASP propagator are almost identical to the the one-step

Fresnel propagator up to a spatial frequency equal to 2.5 μm^{-1}, indicated by the dashed circle in Fig. 2.2a). For higher spatial frequencies, the propagators give slightly different diffraction patterns, with the "+" version deviating more from the reference diffraction pattern of the one-step Fresnel propagator. The worse performance of the "+" version can be explained by the lower bandwidth limit of Q_1^+ compared to Q_1^-. The deviation of the "+" propagator becomes larger for highly divergent beams, which we attribute to the divergent phase front of Q_1^+ (Eq. (2.17)). When multiplying two signals corresponding to the exit wave from the object plane and the phase function Q_1^+, the product may not be Nyquist sampled, even though the individual signals are Nyquist sampled. This effect cannot be solved by further truncating the product $U \cdot Q_1^+$ until it fulfills the Nyquist sampling criterion, because that would mean cropping the exit wave in its physical extent, which would create artificial diffraction from the imposed sharp edges.

2.4 Performance of propagation models on experimental ptychography data

To demonstrate the accuracy of the studied propagators in actual use cases, we perform ptychographic reconstructions on real experimental data with a varying, user-defined pixel size. The goal is to find a range of pixel sizes beyond the default $dx = {}^{\lambda z}/_{N\,dq}$, where the propagators still perform properly and the reconstruction quality is preserved. The results from this analysis can be a tool for choosing the probe and object pixel size during a multi-wavelength ptychographic reconstruction. According to the 2SF model, different magnifications $m = {}^{dq}/_{dx}$ correspond to different intermediate planes at distances z_1, z_2 from the sample and the detector respectively. However, eventually these distances are only implicitly used in the model, as the final expression (Eq. (2.12)) after performing all the calculations on the equations does not include z_1, z_2 explicitly.

The ptychographic setup has been described in detail previously [61], and for the present measurements it was set to provide a monochromatic probe with a wavelength centered at 708 nm. The sample is a standard positive USAF resolution target and is illuminated by a smooth divergent beam with ${}^1/_{e^2}$ diameter equal to 157 µm. A camera (CMOS Manta G419B NIR, 2048x2048 pixels, 5.5 µm pixel size) is placed at a distance $z \approx 75$ mm from the object. The object is scanned across the beam, covering 151 positions of a Fermat spiral scan pattern. The step size is equal to 50 µm, which corresponds to a linear overlap factor of 68%. The diffraction patterns are binned by a factor of 4 before running the reconstruction algorithm in order to speed up the reconstruction process. Reconstructions were performed using the *ptylab.py* toolbox [110]. The reconstruction algorithm for each propagator and magnification ratio has been performed three times with different initial guesses of object and probe, using GPU-accelerated computation on a NVIDIA Tesla K40. In Fig. 5.4 we show the best reconstructions, in terms of minimum converged error, that were achieved for each parameter set.

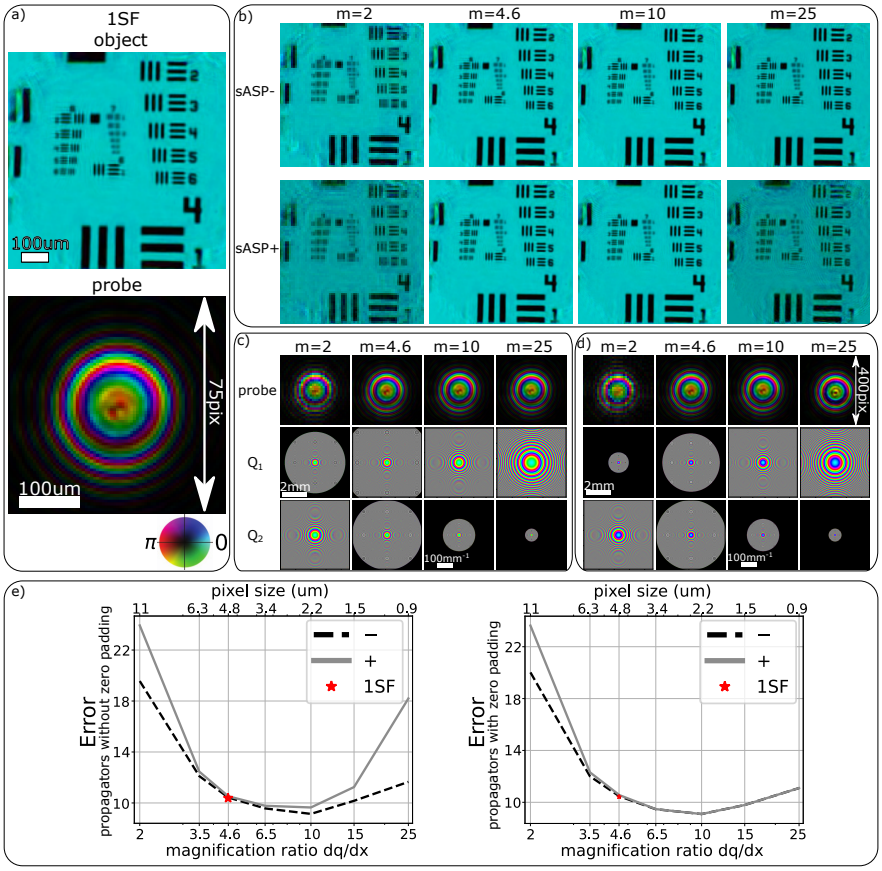

Figure 2.3: Reconstruction results of experimental data for different propagators and pixel sizes at object plane. a) Object and probe reconstructions using the one step Fresnel propagator. b) Object reconstruction using the "−" and "+" version of the sASP propagator for different pixel sizes at the object plane, without zero-padding the exit wave. c-d) Probe reconstructions and full-frame plots of the auxiliary phase functions Q_1 and Q_2 for the c) "−" and d) "+" version of the sASP propagator without zero-padding the exit wave. Q_1 is defined at the object plane, with pixel size dx. The size of the full frame in each dimension is therefore $512 \times dx$, with the corresponding pixel size for each m. The scale bar of the Q_1 plots for magnification equal to $m = 2$ is given as an example, while no scale bar is included in the other plots due to poor contrast of a scale bar inside the frames. Similarly, for the Q_2 plots the size of the full frame in each dimension is equal to $1/dx$. The scale bar of the Q_2 plots for magnification equal to $m = 10$ is given as an example. e) Normalized error between measured and estimated diffraction patterns for different propagators and pixel sizes, summed over all scan positions. The x-axis is in logarithmic scale for better visibility of the numbers. Reconstruction errors are compared for scaledASP± propagators without (left panel) and with (right panel) zero-padding of the exit wave before propagating.

Figure 5.4a) shows the reconstruction results when the propagator is the standard one step Fresnel. The pixel size of the object and the probe is equal to 4.76 µm, which corresponds to a pixel size ratio $m = {}^{dq}/_{dx} = 4.6$ for a binned camera pixel size. Figures 5.4b-d) show the results when repeating the reconstruction process using the sASP± propagators and varying pixel size ratios. For the results in Figs. 5.4b-d) we did not perform zero-padding before propagating, as this step is not implemented in the standard version of Ptylab. However, we repeated the reconstructions with zero-padded fields and include the error results with and without zero-padding for comparison in Fig. 5.4e).

In Fig. 5.4e) we have calculated the error between the estimated diffraction patterns, I_e, after convergence of the reconstruction algorithm, and measured diffraction patterns, I_m, for every propagator and pixel size ratio m. The error is calculated over all the diffraction patterns as $\sum_j \frac{\sum_{x,y} |I_e^j - I_m^j|}{\sum_{x,y} I_m^j}$, with j the index of the scan position. The results indicate that for the non-zero-padded data there is a range between $m = 4.6$ and $m = 15$ where the reconstruction error is low, whereas for pixel sizes outside this range the error increases substantially, especially for the propagator with the + sign. We can also associate the phase functions Q_1 and Q_2 with the model errors and observe that for extreme low or high pixel size ratios m, either Q_1 or Q_2 have a very dense phase progression in the radial direction and need to be heavily cropped to remove the aliasing. Furthermore, the lower bandwidth limit for the "+" propagator, which indicates an even faster phase progression radially, affects negatively the precision of the propagated fields and subsequently the reconstruction results.

Performance improvement in the propagation when we zero-pad the fields beforehand is apparent for large magnification ratios. As mentioned in Sec. 2.3, for the standard pixel size, which corresponds to $m = 4.6$ in our experiment, the probe size must be smaller or equal to half the frame size. In Fig. 5.4a) we indicate that the probe extends over an area of 75×75 pixels, while the frame size is 512×512 pixels. However, for $m = 25$ the probe spans over an area of 400×400 pixels, which can lead to strong circular convolution artifacts. This problem is more apparent in the + propagator, but zero-padding ensures that both + and − propagators behave similarly and exhibit the same model error. For the propagations related to this experimental dataset, we have also calculated the energy transferred, according to definition in Sec. 2.2.6. Our findings indicate that more than 99.9% of the energy of the exit waves is preserved after multiplications with Q_1 in the real domain and Q_2 in the reciprocal domain.

To make solid conclusions on the best range of m that leads to optimal reconstruction quality, we need to clarify whether the exact value of m or the deviation from the diffraction-limited resolution is the cause for increased reconstruction error. For this reason we have performed a series of reconstructions with a binning factor equal to 2 for our ptychographic dataset, which changes the detector pixel size, but does not affect the resolution limit. When binning with a different binning factor, the number of pixels N of the probe and the diffraction patterns also change accordingly, which leaves the bandwidth limit for Q_2 unchanged (Eq. (2.27)). Therefore, reconstructions using binned data

with another binning factor have a different influence on the functions that we want to compare. However, this round of reconstructions can still provide some insight into the limitations of the free choice of the magnification ratio m. The error from these reconstructions, also calculated as $\sum_j \frac{\sum_{x,y} |I_e^j - I_m^j|}{\sum_{x,y} I_m^j}$, is shown in Appendix 2.6.6.

In this analysis (binning factor equal to 2) the magnification ratio for object pixel size equal to diffraction limit is equal to $m = 2.3$. Reconstruction with magnification ratio equal to or slightly smaller than 2.3 still gives very good reconstruction quality and low error, which indicates that, in this regime of m, the actual pixel size and not the exact value of m influences the reconstruction quality. On the other hand, choosing $m = 12.5$, which corresponds to an object pixel size with $m = 25$ for the dataset with binning factor equal to 4, the reconstruction quality is still very good and the error is low, while a deterioration in reconstruction quality and increase of the error is noticeable for $m \approx 20$. This result indicates that in the large-m regime, the exact value of m (and not the object pixel size per se) determines the limit for a good ptychographic reconstruction. The latter can be explained by interpreting Eq. (2.27), as Q_2 is the function with strong bandwidth limits for large ms (Figs. 5.4d,e)). The bandwidth limit for Q_2 is $u_{max} = {}^{mkN\,dx}/_{4\pi z} = {}^{k\cdot FoV}/_{4\pi z}$, where FoV is the field of view of the detector and is, therefore, independent of the binning. Also, the pixel size of Q_2 is $\Delta u = {}^{1}/_{N\,dx}$ (Eq. (2.27)). Since $N_{bin2} = 2N_{bin4}$, we can 'afford' to set $dx_{bin2} = {}^{1}/_{2} \cdot dx_{bin4}$, such that Q_2 has the same sampling, and therefore, the same accuracy.

From all the above we can conclude that it is generally better to choose the propagator with the negative sign if we do not intend to zero-pad the fields before propagating, and choose the pixel size such that for all wavelengths the pixel size ratio is equal to or slightly larger than the diffraction-limited resolutions. Zero-padding is typically recommended, but the reconstruction time increases because of the larger array sizes. The results align very well with the intuitive decision one would make, as one would choose a pixel size smaller or equal to the resolution limit, so that one can make best use of the capabilities of their imaging setup. However, the above analysis shows that, even with zero-padding, there are limitations on the minimum pixel size one should use for the probe and object representation, as we observed a slight increase in the reconstruction error. This is particularly useful when, for instance, performing measurements with a broadband source. In such a scenario, using a common object pixel size for the full bandwidth may lead to suboptimal modelling of the propagation for the longest wavelength, because the selected pixel size will be very different from the respective resolution limit.

2.5 Conclusion

In this paper we investigated the relative performance of the propagation models that are commonly used in multi-wavelength ptychography experiments, especially with regards to the pixel size magnification ratio. We looked at three

well-known propagation models, namely the 2-step Fresnel propagator, the scaled angular spectrum propagator and the chirp-Z transform. The theoretical analysis revealed that all three propagators are identical in principle, with each having two versions, which we denoted as "+" and "−". We compared the performance of these two versions and observed that the performance depends strongly on the bandwidth limitations set by the Nyquist theorem, which are always less stringent for the "−" propagator. Furthermore, we investigated the range over which the pixel size at the object plane can be arbitrarily chosen. The results indicate that the pixel size should be such that for all wavelengths it is (slightly) smaller than or equal to the Abbe resolution limit. The exact range of m that can describe accurately the propagation depends on a variety of parameters, such as the number of pixels N, and the λz product. We believe that this analysis can serve as a guideline for improving the reconstruction process of ptychographic datasets.

2.6 Appendix

2.6.1 Derivation of two-step Fresnel propagation

In this section we present the derivation of Eq. (2.7) from Eq. (2.6) for the 2SF propagation model.

$$\begin{aligned} U(m_2dq, n_2dq) =& \frac{e^{ikz_2}di^2}{i\lambda z_2} e^{i\frac{k}{2z_2}[(m_2dq)^2+(n_2dq)^2]} N \cdot \mathscr{F}^{(-1)}\Bigg\{ \Big(\frac{e^{ikz_1}dx^2}{i\lambda z_1} \cdot \\ & e^{i\frac{k}{2z_1}[(m_{1a}d_i)^2+(n_{1a}d_i)^2]} N \mathscr{F}^{(-1)}\Bigg\{ U(m_1dx, n_1dx) \cdot \\ & e^{i\frac{k}{2z_1}[(m_1dx)^2+(n_1dx)^2]} \Bigg\} \Big) e^{i\frac{k}{2z_2}[(m_{1a}d_i)^2+(n_{1a}d_i)^2]} \Bigg\} \end{aligned} \tag{2.6}$$

The constant factor $e^{ikz_1}dx^2/i\lambda z_1$ can be taken out of the Fourier transform operator

$$\begin{aligned} U(m_2dq, n_2dq) =& \frac{e^{ikz_2}di^2}{i\lambda z_2} \frac{e^{ikz_1}dx^2}{i\lambda z_1} e^{i\frac{k}{2z_2}[(m_2dq)^2+(n_2dq)^2]} N^2 \cdot \\ & \mathscr{F}^{(-1)}\Bigg\{ e^{i\frac{k}{2z_1}[(m_{1a}d_i)^2+(n_{1a}d_i)^2]} e^{i\frac{k}{2z_2}[(m_{1a}d_i)^2+(n_{1a}d_i)^2]} \cdot \\ & \mathscr{F}^{(-1)}\Bigg\{ U(m_1dx, n_1dx) e^{i\frac{k}{2z_1}[(m_1dx)^2+(n_1dx)^2]} \Bigg\} \Bigg\} \end{aligned}$$

We replace $di = \lambda|z_1|/Ndx$ outside the Fourier transform operator and group the phase terms inside the operator

$$U(m_2dq, n_2dq) = \frac{e^{ikz}z_1}{-z_2N^2} e^{i\frac{k}{2z_2}[(m_2dq)^2+(n_2dq)^2]} N^2.$$

$$\mathscr{F}^{(-1)}\Bigg\{ e^{i\frac{kd_i^2}{2}(m_{1a}^2+n_{1a}^2)\left(\frac{1}{z_1}+\frac{1}{z_2}\right)}\cdot \mathscr{F}^{(-1)}\Big\{ U(m_1dx,n_1dx)e^{i\frac{k}{2z_1}[(m_1dx)^2+(n_1dx)^2]}\Big\}\Bigg\}$$

We replace z_1, z_2 and di with variables that are not related to the intermediate plane

$$\begin{aligned} U(m_2dq,n_2dq) =& \frac{e^{ikz}}{\mp m} e^{i\frac{k(1\pm m)}{\pm 2zm}[(m_2dq)^2+(n_2dq)^2]}\cdot \\ & \mathscr{F}^{(-1)}\Bigg\{ e^{i\frac{k}{2}\left(\frac{\lambda z}{Ndx(1\pm m)}\right)^2(m_{1a}^2+n_{1a}^2)\frac{(1\pm m)^2}{\pm mz}}\cdot \\ & \mathscr{F}^{(-1)}\Big\{ U(m_1dx,n_1dx)e^{i\frac{k(1\pm m)}{2z}[(m_1dx)^2+(n_1dx)^2]}\Big\}\Bigg\} \end{aligned}$$

We replace $\lambda = {}^{2\pi}/_{k}$ and perform the calculations in the phase term that is at the outer Fourier transform operator

$$\begin{aligned} U(m_2dq,n_2dq) =& \frac{e^{ikz}}{\mp m} e^{i\frac{k(1\pm m)}{\pm 2zm}[(m_2dq)^2+(n_2dq)^2]}\cdot \\ & \mathscr{F}^{(-1)}\Bigg\{ e^{\pm i\frac{2\pi^2 z}{mk}\left(\left(\frac{m_{1a}}{Ndx}\right)^2+\left(\frac{n_{1a}}{Ndx}\right)^2\right)}\cdot \\ & \mathscr{F}^{(-1)}\Big\{ U(m_1dx,n_1dx)e^{i\frac{k(1\pm m)}{2z}[(m_1dx)^2+(n_1dx)^2]}\Big\}\Bigg\} \\ =& C^{2SF\pm}Q_3^{2SF\pm}\mathscr{F}^{(-1)}\Bigg\{\mathscr{F}^{(-1)}\Big\{U(m_1dx,n_1dx)Q_1^{2SF\pm}\Big\}Q_2^{2SF\pm}\Bigg\} \end{aligned} \tag{2.7}$$

with $C^{2SF\pm}$, $Q_1^{2SF\pm}$, $Q_2^{2SF\pm}$ and $Q_3^{2SF\pm}$ given in Eqs. (2.8-2.11).

2.6.2 Derivation of scaled angular spectrum propagation

In this section we present the derivation of Eq. (2.15) from Eq. (2.14) for the sASP propagation model.

$$\begin{aligned} U(m_2dq,n_2dq) =& \frac{e^{ikz}dx^2 e^{\mp i\frac{k}{2z'}(1\mp m)\frac{(m_2dq)^2+(n_2dq)^2}{m^2}}}{i\lambda z'}\cdot \\ & \mathscr{F}^{-1}\Bigg\{\mathscr{F}^{\pm 1}\Big\{U''(m_1dx,n_1dx)\Big\}\cdot\mathscr{F}\Big\{h(m_1dx,n_1dx)\Big\}\Bigg\} \end{aligned} \tag{2.14}$$

Equation (2.14) can be written in a compact form, by introducing auxiliary phase functions:

$$U(m_2dq, n_2dq) = \frac{e^{ikz}\,dx^2}{i\lambda z} Q_3^{sASP\mp} \mathscr{F}^{-1}\left\{ \mathscr{F}^{\pm 1}\left\{ U(m_1dx, n_1dx) Q_1^{sASP\mp} \right\} Q_2^{sASP\mp} \right\} \tag{2.29}$$

where

$$Q_1^{sASP\mp} = e^{i\frac{k}{2z}(1\mp m)\left((m_1dx)^2+(n_1dx)^2\right)} \tag{2.30}$$

$$Q_2^{sASP\mp} = \mathscr{F}\left\{ e^{\pm i\frac{km}{2z}\left((m_1dx)^2+(n_1dx)^2\right)} \right\} \tag{2.31}$$

$$Q_3^{sASP\mp} = e^{\mp i\frac{km}{2z}(1\mp m)\frac{(m_2dq)^2+(n_2dq)^2}{m^2}} \tag{2.32}$$

Equation (2.31) can be analytically calculated according to the property that a function $g(x) = e^{\pm i\alpha x^2}$ has a Fourier transform $G(k_x) = \left(1/2 \pm i/2\right) e^{\mp i k_x^2/4\alpha} 1/\sqrt{\alpha}$ if α is a real and positive number [127]. Therefore, Eq. (2.31) can be written with continuous variables as

$$Q_2^{sASP\mp}(k_x, k_y) = \mathscr{F}\left\{ e^{\pm i\frac{km}{2z}\left(x^2+y^2\right)} \right\} = \left(\frac{1}{2} \pm \frac{i}{2}\right) e^{\mp i\frac{k_x^2+k_y^2}{4\frac{km}{2z}}} \frac{1}{\sqrt{\frac{km}{2z}}}$$
$$= C_{Q_2}^{sASP\mp} e^{\mp i\frac{z}{2km}(k_x^2+k_y^2)}$$

where $C_{Q_2}^{sASP\mp}$ includes all constant terms and k_x, k_y are the spatial frequency variables in units rad/m. The above equation can be written with respect to the spatial frequency variables $f_x = {}^{k_x}/_{2\pi}$, $f_y = {}^{k_y}/_{2\pi}$ whose units are m^{-1} as

$$Q_2^{sASP\mp}(f_x, f_y) = C_{Q_2}^{sASP\mp} e^{\mp i\frac{2\pi^2 z}{km}(f_x^2+f_y^2)}$$

or in discretized form, for N samples per dimension and spacing in the real domain equal to dx

$$Q_2^{sASP\mp}(m_f df, n_f df) = C_{Q_2}^{sASP\mp} e^{\mp i\frac{2\pi^2 z}{km}\left((m_f df))^2+(n_f df)^2\right)} \tag{2.33}$$

where $df = {}^1/_{Ndx}$. For simplicity, in the evaluation of Q_2 we will only consider the quadratic phase term with unitary amplitude as the constant term can be taken out of the Fourier transform calculations. Therefore, Eq. (2.29) then becomes

$$U(m_2dq, n_2dq) = C^{sASP\mp} Q_3^{sASP\mp} \cdot$$
$$\mathscr{F}^{-1}\left\{ \mathscr{F}^{\pm 1}\left\{ U(m_1dx, n_1dx) Q_1^{sASP\mp} \right\} Q_2^{sASP\mp} \right\} \tag{2.15}$$

with $C^{sASP\mp}$, $Q_1^{sASP\mp}$, $Q_2^{sASP\mp}$ and $Q_3^{sASP\mp}$ given in Eqs. (2.16-2.19).

2.6.3 Derivation of chirp-Z transform propagation

In this section we present the derivation of Eq. (2.21) from Eq. (2.20) for the CZT propagation model.

$$U(m_2dq, n_2dq) = \frac{e^{ikz}dx^2}{i\lambda z} e^{i\frac{k}{2z}[(m_2dq)^2+(n_2dq)^2]} \cdot \sum_{m_1=-\infty}^{\infty}\sum_{n_1=-\infty}^{\infty} U(m_1dx, n_1dx) e^{i\frac{k}{2z}[(m_1dx)^2+(n_1dx)^2]} \cdot e^{-i\frac{2\pi dxdq}{\lambda z}[(\frac{\pm m_1^2}{2}\pm\frac{m_2^2}{2}\mp\frac{(m_1\mp m_2)^2}{2})+(\pm\frac{n_1^2}{2}\pm\frac{n_2^2}{2}\mp\frac{(n_1\mp n_2)^2}{2})]} \tag{2.20}$$

We can separate the terms in the exponent of the last line of Eq. (2.20) and take the part that has no m_1, n_1 dependence outside of the summation

$$U(m_2dq, n_2dq) = \frac{e^{ikz}dx^2}{i\lambda z} e^{i\frac{k}{2z}[(m_2dq)^2+(n_2dq)^2]} e^{\mp i\frac{2\pi dxdq}{\lambda z}(\frac{m_2^2}{2}+\frac{n_2^2}{2})} \cdot \sum_{m_1=-\infty}^{\infty}\sum_{n_1=-\infty}^{\infty} U(m_1dx, n_1dx) e^{i\frac{k}{2z}[(m_1dx)^2+(n_1dx)^2]} \cdot e^{\mp i\frac{2\pi dxdq}{\lambda z}(\frac{m_1^2}{2}+\frac{n_1^2}{2})} e^{\pm i\frac{2\pi dxdq}{\lambda z}[\frac{(m_1\mp m_2)^2}{2}+\frac{(n_1\mp n_2)^2}{2}]}$$

We can rewrite the expression in a more concise form by introducing $W = e^{\mp i2\pi dxdq/\lambda z}$

$$U(m_2dq, n_2dq) = \frac{e^{ikz}dx^2}{i\lambda z} e^{i\frac{k}{2z}[(m_2dq)^2+(n_2dq)^2]} W^{(\frac{m_2^2}{2}+\frac{n_2^2}{2})} \cdot \sum_{m_1=-\infty}^{\infty}\sum_{n_1=-\infty}^{\infty} \Big(U(m_1dx, n_1dx) e^{i\frac{k}{2z}[(m_1dx)^2+(n_1dx)^2]} \cdot W^{(\frac{m_1^2}{2}+\frac{n_1^2}{2})}\Big) W^{-\left(\frac{(m_1\mp m_2)^2}{2}+\frac{(n_1\mp n_2)^2}{2}\right)}$$

By doing a change of variables $m_1' = -m_1$ and $n_1' = -n_1$ for the "+" case, we can make the difference $m_1' - m_2$ and $n_1' - n_2$ appear in the last row of the above expression. Here we show the result after renaming m_1' to m_1 and n_1' to n_1

$$U(m_2dq, n_2dq) = \frac{e^{ikz}dx^2}{i\lambda z} e^{i\frac{k}{2z}[(m_2dq)^2+(n_2dq)^2]} W^{(\frac{m_2^2}{2}+\frac{n_2^2}{2})} \cdot \sum_{m_1=-\infty}^{\infty}\sum_{n_1=-\infty}^{\infty} \Big(U(\pm m_1dx, \pm n_1dx) e^{i\frac{k}{2z}[(m_1dx)^2+(n_1dx)^2]} \cdot W^{(\frac{m_1^2}{2}+\frac{n_1^2}{2})}\Big) W^{-\left(\frac{(m_1-m_2)^2}{2}+\frac{(n_1-n_2)^2}{2}\right)}$$

The sum represents a convolution between the term in the big brackets and the term outside of the bracket

$$U(m_2dq, n_2dq) = \frac{e^{ikz}dx^2}{i\lambda z} e^{i\frac{k}{2z}[(m_2dq)^2+(n_2dq)^2]} W^{(\frac{m_2^2}{2}+\frac{n_2^2}{2})} \Big(U(\pm m_1 dx, \pm n_1 dx) \cdot e^{i\frac{k}{2z}[(m_1dx)^2+(n_1dx)^2]} W^{(\frac{m_1^2}{2}+\frac{n_1^2}{2})} \Big) * W^{-(\frac{m_1^2}{2}+\frac{n_1^2}{2})}. \quad (2.34)$$

This expression has some analogy to Eq. (2.13) in the sense that it describes the propagated field as a convolution between a modified input field and a transfer function $W^{-(m_1^2/2+n_1^2/2)}$. Similar to the approach taken for the sASP, Eq. (2.34) can be treated in the Fourier domain as a product, considering the necessary zero-padding to convert the circular convolution to linear [124]. This leads to the expression

$$U(m_2dq, n_2dq) = \frac{e^{ikz}dx^2}{i\lambda z} e^{i\frac{k}{2z}[(m_2dq)^2+(n_2dq)^2]} W^{(\frac{m_2^2}{2}+\frac{n_2^2}{2})}. \quad (2.35)$$
$$\mathscr{F}^{-1}\Bigg\{ \mathscr{F}\Big\{ U(\pm m_1 dx, \pm n_1 dx) e^{i\frac{k}{2z}[(m_1dx)^2+(n_1dx)^2]} W^{(\frac{m_1^2}{2}+\frac{n_1^2}{2})} \Big\} \cdot \mathscr{F}\Big\{ W^{-(\frac{m_1^2}{2}+\frac{n_1^2}{2})} \Big\} \Bigg\}$$

and due to the property $\mathscr{F}\{f(-x)\} = \mathscr{F}^{-1}\{f(x)\}$

$$U(m_2dq, n_2dq) = \frac{e^{ikz}dx^2}{i\lambda z} e^{i\frac{k}{2z}[(m_2dq)^2+(n_2dq)^2]} W^{(\frac{m_2^2}{2}+\frac{n_2^2}{2})}.$$
$$\mathscr{F}^{-1}\Bigg\{ \mathscr{F}^{\pm 1}\Big\{ U(m_1 dx, n_1 dx) e^{i\frac{k}{2z}[(m_1dx)^2+(n_1dx)^2]} W^{(\frac{m_1^2}{2}+\frac{n_1^2}{2})} \Big\} \cdot \mathscr{F}\Big\{ W^{-(\frac{m_1^2}{2}+\frac{n_1^2}{2})} \Big\} \Bigg\} \quad (2.36)$$

This expression has a similar structure as Eq. (2.14). While a magnification ratio is not explicitly given, the presence of the nonlinear phase factor W provides the freedom to adjust the pixel size dq for the electric field sampling at plane 2. Therefore, Eq. (2.36) works for any arbitrary magnification ratio as well. In the CZT model, this magnification flexibility can be seen as a side benefit resulting from the introduction of the scalable frequency basis. Mathematically, there is a close analogy between Eq. (2.36) and the 2SF and sASP models (Eqs. (2.6) and (2.14)), in the sense that an additional Fourier transform is needed to attain this scalability. Therefore, the computational cost of all three models is comparable too. Similar to the previous propagators, we can rewrite Eq. (2.36) in a more compact form by introducing auxiliary phase functions, in which we also

explicitly include the magnification ratio m via $dq = mdx$:

$$U(m_2 dq, n_2 dq) = \frac{e^{ikz} dx^2}{i\lambda z} Q_3^{CZT\mp} \mathscr{F}^{-1}\left\{ \mathscr{F}^{\pm 1}\left\{ U(m_1 dx, n_1 dx) Q_1^{CZT\mp} \right\} Q_2^{CZT\mp} \right\} \tag{2.21}$$

with $Q_1^{CZT\mp}$, $Q_2^{CZT\mp}$ and $Q_3^{CZT\mp}$ given in Eqs. (2.22-2.24).

2.6.4 Rewriting two-step Fresnel propagation due to symmetry of Q_2

In this section we derive Eq. (2.12) from Eq. (2.7), using the symmetry of Q_2 around $(m_{1a}, n_{1a}) = (0, 0)$.

$$\begin{aligned}
&\mathscr{F}\left\{ \mathscr{F}^{-1}\left\{ U(x_1, y_1) Q_1(x_1, y_1) \right\} Q_2(k_x, k_y) \right\}(x_2, y_2) = \\
&\quad = \iint_{-\infty}^{\infty} Q_2(k_x, k_y) \Big(\iint_{-\infty}^{\infty} U(x, y) Q_1(x, y) e^{-i(k_x x_1 + k_y y_1)} dx\, dy \Big) \cdot \\
&\qquad\qquad e^{i(k_x x_2 + k_y y_2)} dk_x\, dk_y \\
&\quad \overset{k'_x = -k_x,\, k'_y = -k_y}{=\!=\!=} \iint_{-\infty}^{\infty} Q_2(-k'_x, -k'_y) \Big(\iint_{-\infty}^{\infty} U(x, y) Q_1(x, y) e^{i(k'_x x_1 + k'_y y_1)} dx\, dy \Big) \cdot \\
&\qquad\qquad e^{-i(k'_x x_2 + k'_y y_2)} dk'_x\, dk'_y \\
&\quad = \iint_{-\infty}^{\infty} Q_2(k'_x, k'_y) \Big(\iint_{-\infty}^{\infty} U(x, y) Q_1(x, y) e^{i(k'_x x_1 + k'_y y_1)} dx\, dy \Big) \cdot \\
&\qquad\qquad e^{-i(k'_x x_2 + k'_y y_2)} dk'_x\, dk'_y \\
&\quad = \mathscr{F}^{-1}\left\{ \mathscr{F}\left\{ U(x_1, y_1) Q_1(x_1, y_1) \right\} Q_2(k_x, k_y) \right\}(x_2, y_2)
\end{aligned}$$

Similarly,

$$\begin{aligned}
&\mathscr{F}\left\{ \mathscr{F}\left\{ U(x_1, y_1) Q_1(x_1, y_1) \right\} Q_2(k_x, k_y) \right\} = \\
&\qquad\qquad \mathscr{F}^{-1}\left\{ \mathscr{F}^{-1}\left\{ U(x_1, y_1) Q_1(x_1, y_1) \right\} Q_2(k_x, k_y) \right\}
\end{aligned}$$

Therefore, we can rewrite Eq. (2.7) in the form

$$U(m_2 dq, n_2 dq) = C^{2SF\pm} Q_3^{2SF\pm} \mathscr{F}^{-1}\left\{ \mathscr{F}^{\mp 1}\left\{ U(m_1 dx, n_1 dx) Q_1^{2SF\pm} \right\} Q_2^{2SF\pm} \right\} \tag{2.12}$$

2.6.5 Effect of zero-padding in the accuracy of the propagators for spatially confined probes

We study the effect of zero-padding the field before propagating, when the field is confined at a small area within an $N \times N$ array. This is the case for the simulations of Fig. 2.2, where the total field of view for the exit wave at the sample plane is approximately 300 µm, while the beam size is 23 µm FWHM, with a Gaussian profile.

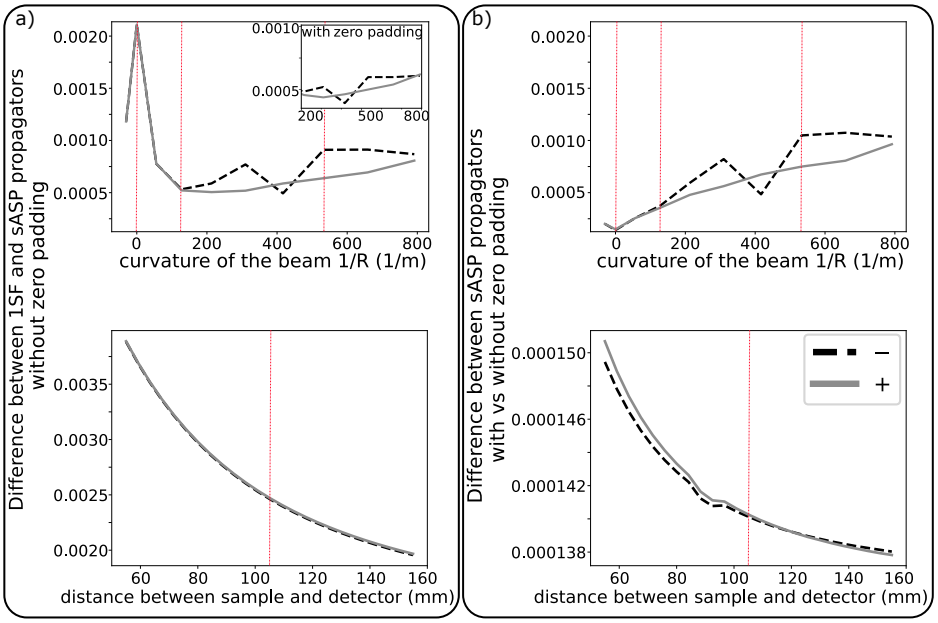

Figure 2.4: Difference between diffraction patterns calculated with two different propagators, defined as $\Sigma_{x,y} {}^{|I_{prop1}-I_{prop2}|}/_{\Sigma_{x,y} I_{prop1}}$. a) Comparison between non-zero-padded sASP± and one-step Fresnel propagator. The inset shows a zoomed-in plot of the difference between zero-padded sASP± and one-step Fresnel propagator at high divergences. b) Effect of zero padding separately on sASP−, sASP+. In both a) and b) the top panels show results when the experimental settings (wavelength, object to detector distance, detector pixel size) are same as the ones considered in Sec. 2.3 and we vary the probe divergence. Bottom panels: we vary the object to detector distance for the case of a probe with flat phase. The detector pixel size changes proportionately to the distance, so that the diffraction patterns can be calculated, for reference, with the one-step Fresnel propagator. The vertical lines indicate the cases that are exhibited in Fig. 2.2. In all graphs, the solid line indicates the "+" propagator and the dashed line the "−" version.

In Fig. 2.4 we show the normalized difference on the diffraction patterns, when they are propagated with different propagators. Specifically, in Fig. 2.4b) we show the difference between using zero-padded and non-zero-padded data for both

the "+" and "−" versions. For reference, in Fig. 2.4a) we show the difference in the diffraction patterns calculated via the one-step Fresnel and the sASP± propagators. The normalized difference is defined as $\sum_{x,y} |I_{prop1} - I_{prop2}| / \sum_{x,y} I_{prop1}$, with prop1 and prop2 the two propagators that are under comparison. We study the trend in the normalized difference as a function of two parameters, namely the divergence of the probe, similar to Fig. 2.2, and the object to detector distance with a flat probe wavefront. The results are shown in the top and bottom panels of Fig. 2.4 respectively.

From the results we observe that the difference between the propagators is generally low, but we can distinguish two main points. First, for high probe divergence the difference in the diffraction patterns between zero-padded and non-zero-padded data before propagating is more prominent than for low divergence. Furthermore, for high divergences the error between zero-padded sASP and one-step Fresnel is smaller, as shown in the inset of Fig. 2.4. Therefore, we conclude that in such cases it is more accurate to zero-pad the field data before propagating. On the other hand, for a flat wavefront illumination, such as when the sample is at the focal plane of a beam, the improvement of zero-padding in the accuracy is negligible (Fig. 2.4b), bottom).

Second, from the bottom panel of Fig. 2.4a) we observe that when the distance between the measurement and detection planes are close, the difference between one-step Fresnel and sASP is increased. This difference cannot mitigated by zero-padding, as from Eqs. (2.26),(2.28) we see that a short propagation distance affects the bandwidth limit of Q_1 which cannot be improved with zero-padding. The reason for this difference needs to be further investigated.

The energy transferred after multiplication with Q_1 and Q_2 in the real and reciprocal domain respectively is, according to the definition given in Sec. 2.2.6, always larger than 99.98% for the non-zero-padded exit waves for all cases studied in this section. Therefore, we conclude that there is no physical error due to cropping significant spatial frequency content in our results.

2.6.6 Experimental results with smaller detector pixel size

In this section we show reconstruction error results when working with diffraction data that have been binned by a factor of 2, resulting in a detector pixel size equal to 11 µm. The results are shown in Fig. 2.5. We observe that the trend of the error is similar to the results with 4×4-binned data, shown in Fig. 5.4, especially for large magnification ratios. However, as we see in the top x-axis scale, the object-plane pixel sizes are half of what is shown in Fig. 5.4. Therefore, as discussed in the main text, the accuracy of the propagation is mostly associated to the magnification ratio m and not the absolute number of the pixel size at the object plane. On the other hand, for low m we see a better reconstruction result with the 2×2- data, as discussed in the main text as well. Finally, we observe that the effect of zero-padding is the same as with the 4×4-binned data, with considerable improvement of the reconstruction for high values of m.

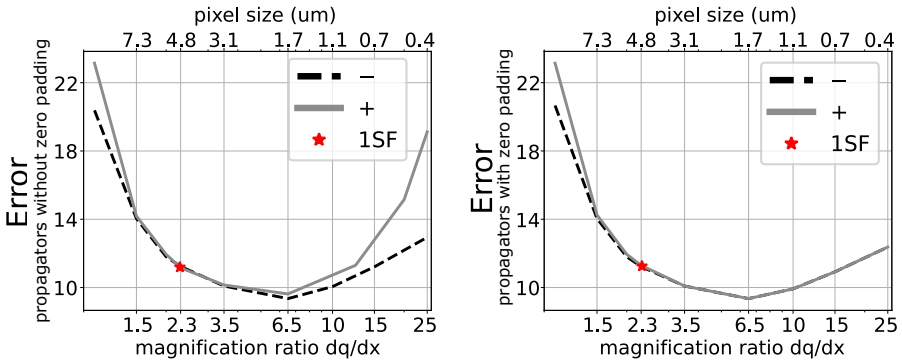

Figure 2.5: Reconstruction error for different magnification ratios, when the experimental data are binned with a binning factor equal to 2. The x-axis is in logarithmic scale for better visibility of the numbers. Left panel: there is no zero-padding in the exit waves when using the sASP± propagator. Right panel: the exit waves are zero-padded when using the sASP± propagator.

Chapter 3

Observation of chromatic effects in high-order harmonic generation

High-harmonic generation sources can produce coherent, broadband radiation at extreme-ultraviolet and soft-X-ray wavelengths. The wavefronts of the generated high-order harmonics are influenced by the incident laser field, the generation conditions, and geometry. These influences depend on harmonic wavelength, which may result in wavelength-dependent focusing properties and spatiotemporal couplings that can affect attosecond physics experiments. We experimentally demonstrate and characterize these chromatic effects in high-harmonic generation by measuring the spectrally resolved high-harmonic wavefronts as a function of generation conditions. We find that the high-harmonic generation process can have significant intrinsic chromatic aberration, particularly for converging incident laser fields. Furthermore, we identify regimes where chromatic effects can be minimized, and show that analytical single-atom models allow accurate predictions of harmonic wavefronts produced by a specific driving field.

The content of this chapter has been published as: Xiaomeng Liu, Antonios Pelekanidis, Mengqi Du, Fengling Zhang, Kjeld S. E. Eikema, and Stefan Witte, *Observation of chromatic effects in high-order harmonic generation,* Phys. Rev. Res. **5**, 043100 (2023).

3.1 Introduction

High-order harmonic generation (HHG) as a laboratory-scale source of coherent soft-X-rays and extreme ultraviolet (EUV) pulses has become indispensable for many table-top coherent diffractive imaging (CDI) experiments [21, 34, 128], and attosecond physics [129]. In the high-harmonic generation process [80, 81, 130, 131], an intense broadband femtosecond infrared laser pulse, with a peak intensity on the order of $10^{14} - 10^{15}\,\mathrm{W\,cm^{-2}}$, is focused into a noble gas medium. The strong driving field leads to electron tunnelling, acceleration and recombination, subsequently leading to the generation of a chirped broadband EUV pulse [129], that for multicycle laser pulses consists of a comb of odd-order harmonics of the drive laser frequency [132, 133].

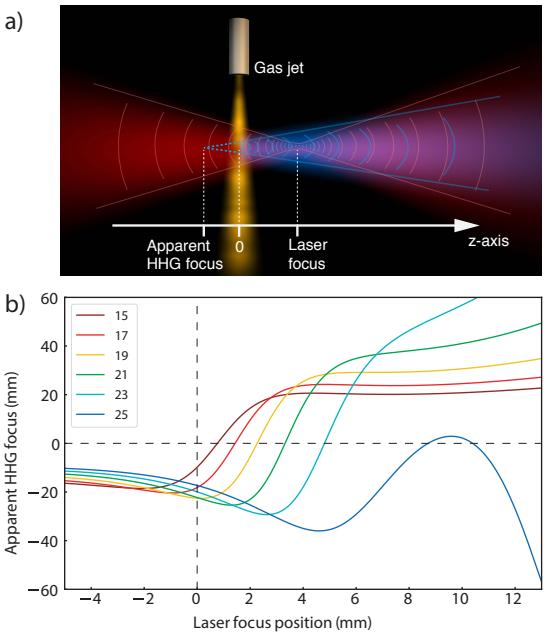

Figure 3.1: a) Typical geometry for high-harmonic generation (HHG). The wavefront curvature of the harmonics may differ from the driving field, mainly because of the dipole phase. b) Apparent focus positions of harmonics 15-25 generated in Argon with laser parameters $\lambda = 800$ nm, $I_0 = 1.7 \times 10^{14}$ W/cm^2, $w_0 = 50$ μm. For both laser and HHG, positive numbers indicate a focus behind the gas jet (being a real HHG focus), and negative numbers mean the focus is before the jet (virtual HHG focus).

The ultrashort pulse duration and broad spectral bandwidth of HHG sources are key enabling features for probing ultrafast phenomena [134, 135], but there is the possibility of couplings between their temporal and spatial properties [136]. Such spatiotemporal couplings can significantly increase the pulse duration upon propagation [137], affect the propagation itself in dispersive nonlinear media [138], and have an influence on nonlinear effects [139]. In the case of time-varying

polarization states, spatiotemporal couplings become even more complex [140]. In many experiments in attosecond spectroscopy [141, 142] and lensless imaging [34, 143], a high quality focus is crucial to obtain a short pulse duration and high peak intensity at the target.

While spatiotemporal coupling is typically associated with aberrations caused by optical components, recent work showed that the HHG process itself may already introduce chromatic aberrations [92, 144, 145], as the wavefront and intensity profile of the generated high-harmonic beam can depend both on the harmonic order and the generation geometry. Placing the gas medium slightly before the waist of the driving laser beam was shown to result in an HHG beam in which the wavefronts range from diverging to converging for different harmonics [145, 146].

The wavefront distribution of a high-harmonic field can be expressed as [92]:

$$\Phi_q(r,z) = q\phi(r,z) + \Phi_i(r,z), \tag{3.1}$$

where $\phi(r,z)$ is the drive laser phase, q is the harmonic order and $\Phi_i(r,z)$ is the atomic dipole phase [81, 87]. While the dipole phase is commonly approximated as $\Phi_i = \alpha_q I$ with I the laser intensity [87–89], we take the expression derived by Guo et al. [91, 92] that for the short trajectories takes the form $\Phi_i = \gamma_s(q\omega_l - \omega_p)/I$. In this expression, $\omega_p = I_p/\hbar$ is the frequency corresponding to the ionization energy I_p and $\gamma_s = a\omega_l^2$ with ω_l the laser frequency and a a constant. These two dipole phase expressions are mutually consistent when taking into account that the α_q-parameter depends on harmonic order and intensity [91]. The $1/I-$model is insightful as its prefactor is a true constant at fixed ω_l, and provides an analytical expression for the phase properties of HHG fields. For an HHG beam with a Gaussian spatial intensity profile, the radius of curvature of the HHG wavefront can be obtained by approximating the phase with a polynomial expansion up to r^2 (considering only short trajectories), plus the wavefront curvature of the drive laser [92]:

$$\frac{1}{R_q} = \frac{1}{R_l(z)} + \frac{4\gamma_s c\left(q\omega_l - \omega_p\right)^2}{I_0 w_0^2 q\omega_l}, \tag{3.2}$$

in which $R_l(z)$ is the radius of curvature of the laser field at the gas jet, I_0 is the peak intensity, and w_0 is the beam waist.

Figure 3.1 shows the concept of the harmonics being generated with a different wavefront curvature than the driving field. We set the geometry as in Fig. 3.1a), with the gas jet as the origin and positive z-values being further downstream (behind the medium). The difference in wavefront curvature of the driving laser field leads to a different 'apparent' focus position where the harmonics appear to originate from, with significant dependence on the harmonic order [92, 145]. We use Eq. (3.2) to calculate the expected apparent foci for our typical generation conditions, with the results shown in Fig. 3.1b). In particular for the laser focusing behind the gas jet, strong wavelength-dependent variations of several Rayleigh lengths in the HHG focus positions are predicted, with most harmonics

changing from a virtual to a real focus at a specific generation position. Refocusing such beams for strong-field attosecond experiments would result in severe chromatic aberrations, even when using fully achromatic refocusing optics.

A quantitative experimental verification of these predicted chromatic aberrations is challenging, as it requires a wavelength-resolved focus characterization with high spatial resolution. Alternatively, a model-independent reconstruction of the HHG focal spot is possible from high-resolution far-field measurements of the transverse complex field distribution of each harmonic. While various far-field wavefront sensing methods have been developed for HHG sources [144, 147–151], achieving both sufficient spatial and spectral resolution without relying on model assumptions remained challenging. Recently, a computational imaging method called ptychography has been applied for wavefront sensing applications [34, 61], where the quantitative complex electric field can be reconstructed with diffraction-limited spatial resolution. Specifically, for characterization of HHG sources, we have developed a multi-wavelength ptychographic wavefront sensing (PWFS) method [63]. In this work, we employ PWFS to study the intrinsic chromatic variations in the HHG process with unprecedented detail. The reconstructed complex field distributions from PWFS can be numerically propagated back to their apparent focus position near the generation medium, without requiring Gaussian optics or assuming certain beam symmetry. By recording PWFS data as a function of the HHG generation geometry, a detailed analysis of these intrinsic chromatic effects in HHG becomes possible. By simultaneously characterizing the complex field of the drive laser, we can compare the measured HHG beams with single-atom-model predictions for a given driving field, enabling a critical comparison of different model approaches.

3.2 Setup for ptychographic wavefront sensing

We measure the multispectral EUV wavefronts and the fundamental laser wavefront with the experimental setup outlined in Fig. 3.2a). High harmonics are generated in a gas jet, using 0.61 mJ, 45 fs, 825 nm wavelength laser pulses from a noncollinear optical chirped pulse amplifier running at 300 Hz repetition rate. The gas jet is formed by a supersonic expansion from a pulsed nozzle into a stainless steel tube with 0.6 mm inner diameter, at 2 bar Argon backing pressure. The laser crosses the jet through 100 μm diameter holes in the side of the tube. As the interaction length is significantly shorter than the 3.4 mm Rayleigh length of the laser focus, propagation effects are expected to be limited [89, 93], and we therefore focus our analysis on the single atom response and the influence of the driving laser wavefront. For the PWFS measurements, an EUV wavefront sensor mask (EUV WFS) as used in [63] is mounted on a two-dimensional translation stage (Smaract SLC-1730) and placed 40.9 cm after the gas jet. A 200 nm thick free-standing aluminum filter blocks the fundamental beam, and the HHG beam is detected by an EUV-sensitive camera (Andor Ikon-L 936SO, 2048×2048 pixels, pixel size 13.5 μm) placed 56.5 cm behind the EUV WFS. A series of diffraction patterns is recorded as the EUV WFS is transversely

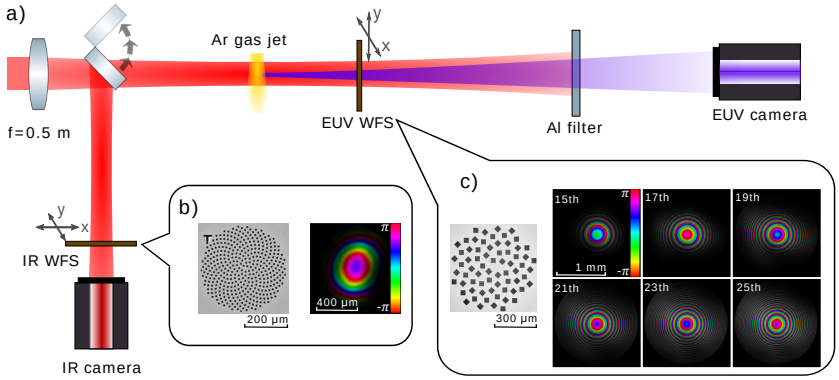

Figure 3.2: a) Experimental setup for wavelength-dependent EUV wavefront measurements. Ultrashort near-infrared pulses are focused into an Argon gas jet for HHG, using a $f = 0.5$ m lens. An EUV wavefront sensor mask (EUV WFS) is transversally scanned through the generated HHG beam for ptychographic wavefront characterization, and the resulting EUV diffraction patterns are recorded by an EUV-sensitive CCD camera. The fundamental field is also characterized using ptychography, in a separate measurement arm. b) Scanning electron microscopy (SEM) image of the near-IR wavefront sensor mask, and a reconstructed laser field (brightness linearly encodes amplitude, color represents phase). c) SEM image of the EUV WFS mask, and a set of reconstructed fields for different harmonics.

scanned through the HHG beam. To characterize the fundamental field, a near-infrared ptychography measurement is set up in an auxiliary beam path outside the vacuum system. Band-pass filters are used to select single wavelengths from the driving laser, enabling characterization of the driving laser at several wavelengths across the broad spectrum. A different wavefront sensor mask is used to measure the fundamental wavefront (Fig. 3.2b)). An infrared camera (Allied Vision Prosilica GT3400) is used to capture the diffraction patterns.

3.3 Results: HHG wavefronts and chromatic aberrations

From a single ptychography scan, complex fields at all harmonic wavelengths are reconstructed (Fig. 3.2c)). These fields can be numerically propagated backward along the beam direction, enabling an accurate characterization of the focus position and the properties of the HHG beam [63].

A reconstruction result with an example of the numerical beam propagation for multiple harmonics is shown in Fig. 3.3. The first column (Figs. 3.3,a1-a6)) contains the reconstructed multispectral EUV fields for harmonics 15 to 25 at the position of the EUV WFS. The plots in the middle column (Figs. 3.3,b1-b6)) show the numerical propagation of the EUV beam through the beam waist, in which the beam direction is from left to right. The dashed white line indicates

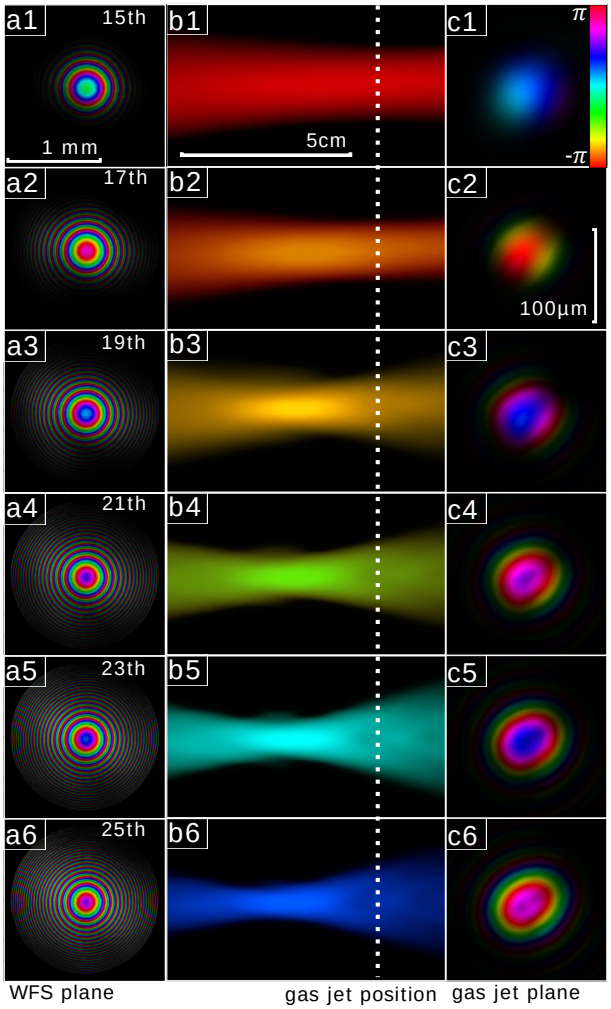

Figure 3.3: a) Reconstructed HHG wavefronts and focusing properties for a laser focus positioned 3.6 mm downstream of the jet. Left column (a1-a6): Reconstructed wavefronts of harmonic beams in the wavefront sensor plane. The corresponding wavelength (harmonic order) is 54.7 nm (15th), 48.2 nm (17th), 43.1 nm (19th), 38.9 nm (21st), 35.5 nm (23rd) and 32.6 nm (25th). Middle column (b1-b6): axial cross section of the reconstructed beam propagating through their foci. The scale bars are shared for all panels. The white dashed line indicates the gas jet position. Right column(c1-c6): reconstructed beam profiles in the gas jet plane. Intensity is linearly encoded in brightness, and phase is encoded as color.

the position of the gas jet. It should be noted that only linear propagation is considered here, and any (nonlinear) effects of the gas jet on the beam propagation are not included. This approach provides a detailed view of the HHG beams around their focus region, with sufficient resolution to identify that the generated harmonics clearly have different focusing properties. In this example we find that the 15^{th} harmonic focuses near the gas jet plane, while the higher harmonics show progressively larger divergence at the gas jet plane (Figs. 3.3c1-c6)), and have virtual foci up to several centimeters upstream of the jet. From the ptychography scans, the complex fields of the fundamental and the generated harmonics can be directly compared around the focus region.

To study the harmonic-order dependence of the focusing properties in detail, we performed a series of PWFS measurements while varying the relative position between the laser focus and the gas jet. The results are shown in Figs. 3.4a,b) where the apparent focus position of harmonics 15 to 25 is determined as a function of the relative gas jet position. Due to slight astigmatism in the fundamental beam, we observed minor differences in horizontal and vertical focusing behaviour, therefore we show separately the focus positions in the horizontal and vertical plane in Figs. 3.4a) and b) respectively.

In Fig. 3.4 we maintain the axis convention of Fig. 3.1, with positive numbers indicating a focus behind the gas jet (i.e. a real focus). The high resolution of our wavefront measurements enables an accurate determination of the focus position of the individual harmonics, with the major advantage that there are no assumptions needed to retrieve the focus position from the measured data, other than the paraxial approximation used in the numerical propagation of the fields. Therefore, we obtain a detailed overview of the intrinsic chromatic aberration resulting from the HHG process itself.

3.4 Discussion

The observed chromatic aberrations qualitatively follow the trends predicted by the single-atom model (Fig. 3.1b)). In the regime of HHG with a converging drive laser beam, some lower-order harmonics are found to have a real focus behind the jet [145]. For these harmonics, the fundamental wavefront contribution dominates the dipole phase. When the laser focus coincides with the gas jet, all harmonic wavefronts are diverging, as only the dipole phase contribution to the harmonic phase is present, which is always divergent. The harmonic-wavelength-dependence of the dipole phase then directly results in chromatic variations. For a laser focus before the jet, all harmonics have diverging wavefronts and thus virtual foci, as expected from Eq. (3.2). Note that these virtual harmonic foci are located several centimeters upstream of the laser focus. An important observation however, is that the chromatic aberrations are significantly smaller in this geometry. The origin of this behaviour is that, while both the dipole phase and fundamental wavefront are diverging, their change as a function of harmonic order is largely inverse, thus partially cancelling wavelength-dependent variations. Figure 3.5 shows the separate influence of dipole phase (Fig. 3.5a)) and wavefront

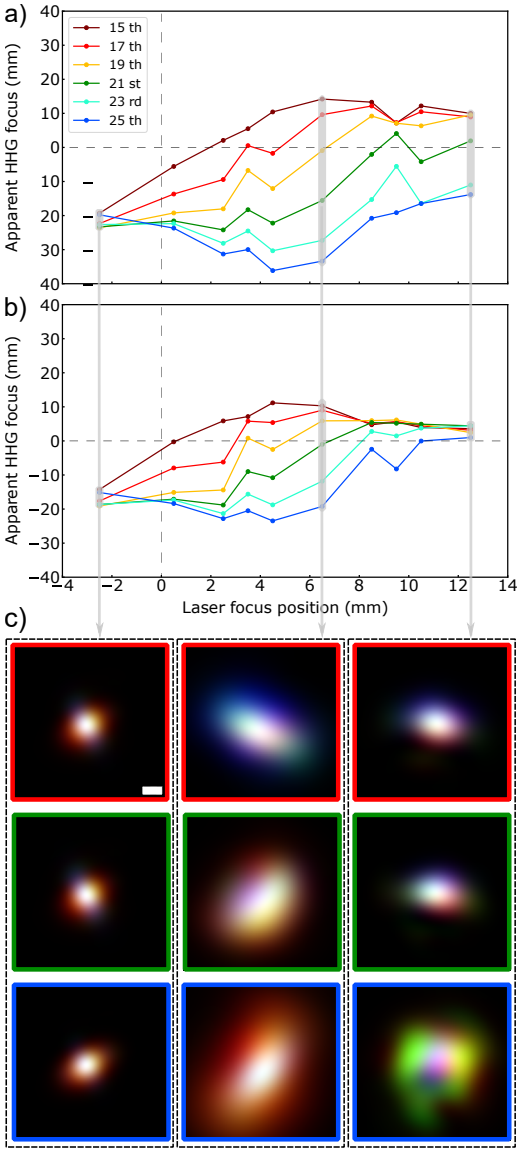

Figure 3.4: a,b) Wavelength-dependent (a) horizontal and (b) vertical focus position of the different harmonics, as determined from reconstructed HHG wavefronts. c) Overlay of reconstructed intensity profiles of harmonics 17 (red), 21 (green) and 25 (blue), at the apparent focus positions of the respective harmonics. The frame color indicates the harmonic that is in focus in that image (red H17, green H21, blue H25). The scale bar in the top left frame is 20 m, and is shared among all images.

transfer (Fig. 3.5b)).

By analyzing the reconstructed complex beam profiles, we find that the shift between the apparent HHG source positions of different harmonics can exceed the Rayleigh length of the harmonic beams, in the present geometry by up to 2-4 times. This effect reaches a maximum when the laser focus is ∼5 mm downstream of the gas jet, corresponding to about one fundamental Rayleigh length. Refocusing of such a multi-wavelength beam, even with perfectly achromatic optics, will result in an aberrated focal spot with spatially varying spectral density and therefore similarly varying durations of attosecond pulses, following model predictions [92]. To give more direct insight into the beams produced in the HHG process, we numerically reconstruct the intensity profiles of three different harmonics around the generation region. The results are shown in Fig. 3.4c), which contain the overlaid intensity profiles of harmonics 17, 21 and 25, at propagation distances that correspond to the apparent focus of each of these harmonics, for three different fundamental focus positions. For a laser focus position before the gas jet, the apparent focus positions of all harmonics are almost identical, and we find a small HHG source spot with a similar profile for all harmonics. Moving to a laser focus behind the gas jet, where a large chromatic aberration was measured, we also observe significant differences in the intensity profiles of the respective harmonics: when reconstructing the HHG beam at the apparent focus position of one specific harmonic, the other harmonics appear clearly defocused, and there is no single position where all harmonics have identical profiles. Further details and additional visualizations are provided in Appendix 3.6.3. We previously already found that astigmatism transfers from the fundamental to the HHG beam in a wavelength-dependent way [63], which is also observed in the present beam reconstructions. We now conclude that dipole-phase-induced wavefront curvature also leads to significant chromatic aberration, and this effect would remain even for diffraction-limited beams.

To connect these experimental results to expectations, a model is needed that simulates the properties of HHG fields based on fundamental field properties. The analytical single-atom model described by Eqs. (3.1) and (3.2) gives an expression for the wavefront, but not the intensity distribution, limiting the options for direct numerical propagation. To find the apparent focus position, the single-atom model does allow for a determination of the radius of curvature through Eq. (3.2). By approximating the beam properties in a Gaussian model, assuming a Gaussian intensity profile and considering only quadratic phase profiles following the paraxial approximation, the focus position z of a beam can be calculated from the radius of curvature R and beam radius w at a given position along the beam propagation axis:

$$z_q = -\frac{R_q}{1 + \left(\lambda_q R_q / \pi w_q^2\right)^2}. \tag{3.3}$$

This Gaussian beam approach can be used when only HHG wavefront information is available, but does require an assumption for the waist of the generated HHG beam. In strong-field approximation (SFA) models, an effective nonlinear-

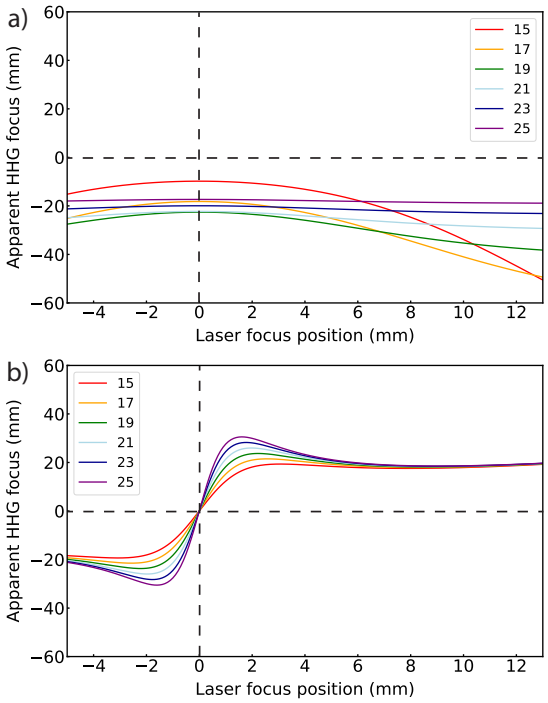

Figure 3.5: Relative contributions to the wavefront and the resulting focus of the HHG beams. a) The calculated apparent focus position only taking into account the dipole phase. b) The calculated apparent focus without dipole phase, only considering transfer of the fundamental wavefront to the harmonics. Note that even for this contribution only, a chromatic effect appears. This is the result of the chosen waist size of the harmonics, which we set as $w_{\mathrm{HHG}} = w_f(z)/\sqrt{m_{\mathrm{eff}}}$ as discussed in the text. For an HHG waist size that scales as $w_f(z)/\sqrt{q}$, this chromatic effect in the phase transfer disappears.

ity m_{eff} is often assumed for plateau harmonics, resulting in a harmonic waist approximation as $w_{\mathrm{HHG}} = w_f(z)/\sqrt{m_{\mathrm{eff}}}$. For all our present single-atom model calculations we have taken $m_{\mathrm{eff}} = 4$. Further details about the procedure to reconstruct the HHG focus position from the measured fundamental field are given in Appendix 3.6.1.

The high accuracy of the focus determination through ptychographic wavefront sensing enables a critical assessment of the dipole phase model. To this end, we calculate the single-atom model predictions using different approximations for the dipole phase, using the experimentally measured fundamental field as the starting point (Fig. 3.6). This field is numerically propagated to the gas jet plane, and its intensity and phase distributions serve as input to Eq. (3.1). This approach enables model predictions for astigmatic and otherwise aberrated beams, as often encountered experimentally. As the model does not include an estimate of the HHG efficiency, we assume Gaussian HHG intensity profiles when calculating the

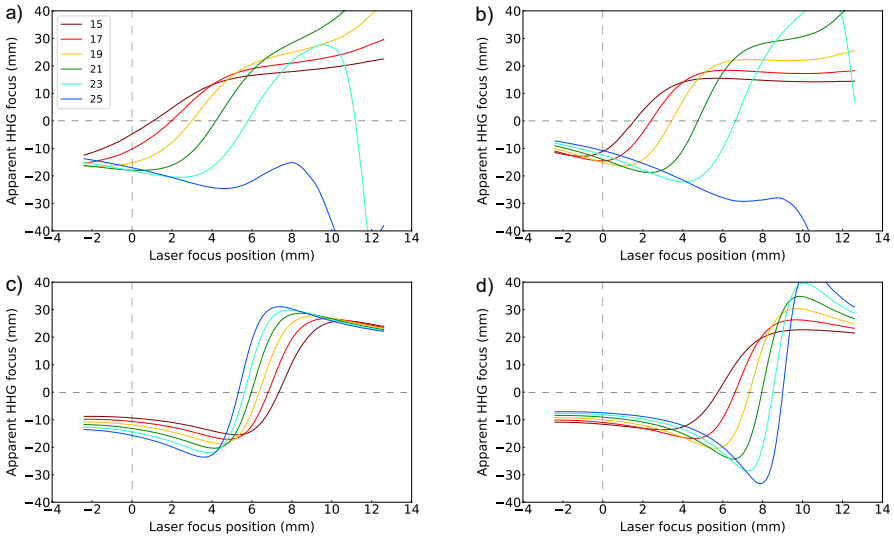

Figure 3.6: Expected wavelength-dependent HHG focusing properties for different dipole phase models, based on the experimentally measured fundamental field. a,b) Calculated a) horizontal and b) vertical focus positions using the $\Phi_i \sim \gamma/I$ model, using $\gamma = 0.9569 \times 10^{-18}$ s^2 W/cm^2. c) Calculation of horizontal focus positions using $\Phi_i \sim \alpha I$, taking a constant value $\alpha = -3 \times 10^{-14}$ cm^2/W. d) Model with $\Phi_i \sim \alpha I$, taking $\alpha \sim q^2$, increasing from -2.025×10^{-14} at $q = 15$ to -7.225×10^{-14} at $q = 25$.

expected HHG focus position.

Figures 3.6a and b show the result for the horizontal and vertical focus positions respectively using the model introduced by Guo et al. [91] and Wikmark et al. [92], based on an analytical derivation resulting in a $1/I-$dependence for the dipole phase. These calculations show a high degree of similarity with the experimental results in Fig. 3.4. In Figs. 3.6c,d) we plot the results of the horizontal focus positions for two other commonly used approaches to model the dipole phase, based on a $\Phi_i \sim \alpha I$ relation, in which the factor α is either constant (Fig. 3.6c)) or quadratically proportional to harmonic order (Fig. 3.6d)). Note that in both cases, the values of α are chosen negative, to ensure that the dipole phase adds a diverging wavefront curvature as physically expected. For the model with constant α, the chromatic aberrations are markedly different from the experimental observations. Making α dependent on harmonic order leads to a qualitative improvement, but this model significantly underestimates the magnitude of the chromatic aberrations when the gas jet is close to the laser focus, and predict variations around positive laser-gas jet positions that are not commensurate with the experimental results.

From this comparison we conclude that the $\Phi_i \sim \gamma/I$ dipole phase model provides an accurate description of the atomic response in our experimental geometry with a thin jet. While nonlinear propagation and phase matching effects cannot be excluded, the close correspondence between the experimental results

and simulations indicates that the observed chromatic effects are well-described by the single-atom response. Since our experiments are performed at high backing pressure, generating sufficient flux to collect the diffraction data needed in ptychographic imaging, self-focusing and plasma-induced defocusing should be considered. For our experimental parameters, we estimate a B-integral of 0.2, and an ionization level of 4% at the peak of the fundamental pulse. From these numbers we estimate that both self-focusing and plasma defocusing separately may lead to additional wavefront curvatures in the range $R \approx 5-10$ cm, and partially cancel as both effects have opposite signs. Such wavefront curvatures will not lead to significant shifts of the HHG foci, and are to first order wavelength-independent. Including such estimates in the calculations of Fig. 3.1b) therefore only leads to a small horizontal shift of all the curves with respect to the laser focus position. Given the quantitative agreement between our single-atom calculations (Figs. 3.6a,b)) and experimental observations (Figs. 3.4a,b)), we conclude that for our parameters propagation-induced effects do not lead to significant modifications of the HHG focusing properties.

For HHG geometries with extended propagation length, more detailed simulations would be required for a quantitative analysis. However, the PWFS approach remains applicable to experimentally characterize the resulting chromatic effects in the HHG beam.

3.5 Conclusion

In conclusion, we have experimentally demonstrated that the wavefronts of the HHG EUV beams can strongly depend on the wavefront and intensity profile of the fundamental laser, as well as the wavelengths of the harmonics themselves. We confirm that the $1/I$-model for the dipole phase can be used for realistic predictions of HHG wavefronts if a measured fundamental laser field is available. Our findings provide guidance for experiments that aim to tightly focus broadband attosecond pulses, where the effects of intrinsic chromatic aberration in the HHG process should be minimized.

3.6 Appendix

3.6.1 Calculating HHG focus position from fundamental beam reconstructions

As stated before, having the measured detailed complex field information for both the fundamental and the HHG beams enables a direct comparison, taking the effect of aberrations in the fundamental beam into account [63]. For the model predictions we initially calculate the phase of the high harmonic field at each frequency $q\omega_l$ according to Eq. (3.1), where the driving laser phase and intensity are known from the ptychographic characterization of the beam at a wavelength close to the central laser wavelength of 830 nm. By numerically propagating the reconstructed wavefront over a range of positions around the focus, we can

simulate the high harmonic generation conditions for the different positions of the focusing lens.

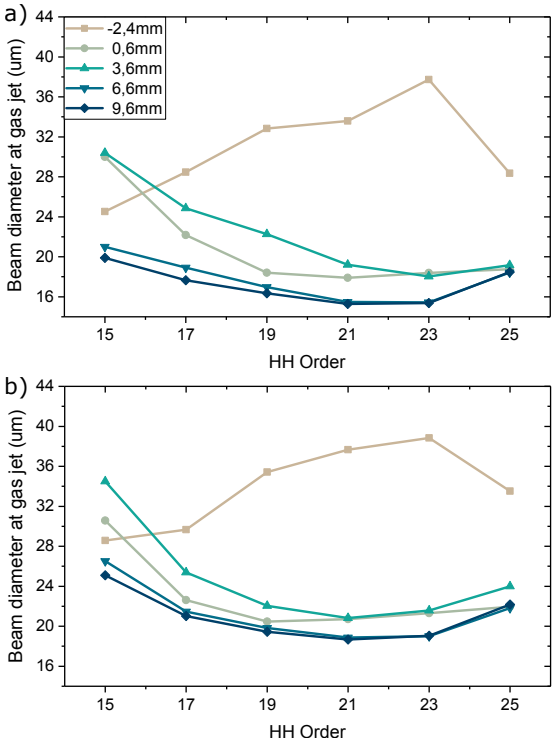

Figure 3.7: Beam diameter of the different harmonics at the gas jet position as reconstructed from the ptychography measurements, for various distances between the gas jet and the fundamental beam waist position. a) horizontal direction, b) vertical direction.

From the estimated phase of the high harmonic wavefronts, we calculate the radius of curvature at the horizontal and vertical directions though fitting a quadratic curve on the 1D wavefront cuts. The radius of curvature for each direction is then

$$R_{x/y} = \frac{k_q}{2a_{2,x/y}}, \tag{3.4}$$

where k_q is the propagation number of the harmonic q, and a_2 is the quadratic term of the fitting curve. The focal distance can then be calculated directly from the radius of curvature using Eq. (3.3), which we apply for the x- and y-directions separately, with the assumption that $w_{\mathrm{HHG}} = w_f(z)/\sqrt{m_{\mathrm{eff}}}$.

To facilitate the quadratic fitting near the saddle point of the fundamental beam, we apply the fit separately to the two phase contributions $\Phi_1 = q\phi$ and $\Phi_2 = \Phi_i$. From these fits we get two radii of curvature per direction $R_{1,x/y}$ and

$R_{2,x/y}$. The total radius of curvature then becomes:

$$R_{x/y} = (\frac{1}{R_{1,x/y}} + \frac{1}{R_{2,x/y}})^{-1}. \tag{3.5}$$

The results from this process are equivalent to the results obtained when we fit a quadratic curve to the total HHG wavefront directly.

For the results shown in Fig. 3.6 we used a peak intensity at the fundamental beam waist of 2.3 $\times 10^{14}$ W/cm^2. At different gas jet positions, the peak intensity is scaled inversely proportional to the increase of the beam size and numerically calculated.

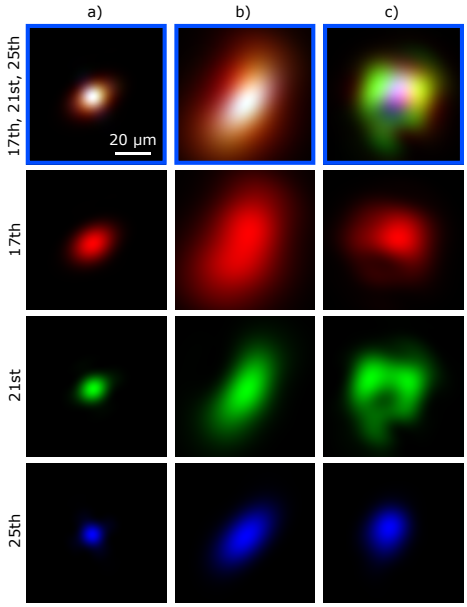

Figure 3.8: Reconstructed beam profiles of harmonics 17, 21 and 25, both overlaid (top row) and separated, at the plane where harmonic 25 has its apparent focus, for three different drive laser positions. The first row corresponds to the last row of Fig. 3.4.

3.6.2 HHG beam diameters at the generation plane

As explained in the main text, the model used to estimate the intensity distribution of harmonics from a known fundamental field assumes a constant effective nonlinearity for plateau harmonics. Numerically propagating the measured harmonic fields to the source plane allows a verification of this assumption. From this data (Fig. 3.7), we actually find significant deviations from this SFA model waist assumption based on a constant effective nonlinearity. This discrepancy may limit the accuracy of a determination of the HHG wavefront based only on

such model calculations, although we find that it does not change the conclusions for our experimental conditions.

3.6.3 Harmonic-resolved beam profile reconstructions

Figure 3.4c shows the reconstructed beam profiles of harmonics 17, 21 and 25 at different positions around the gas jet, for three different generation positions. In those figures, the different harmonics are overlaid as RGB color plots. To provide a more detailed decomposition, we separate the channels of the bottom row of Fig. 3.4c) and plot them together in Fig. 3.8. These are the beam profiles of the respective harmonics, back-propagated to the position where harmonic 25 has its apparent focus. For the left column, which corresponds to a generation condition where the jet is positioned after the fundamental focus, little variation between the harmonics is observed and the spots are generally small. For conditions where the gas jet is placed before the laser focus (Figs. 3.8b,c)), strong chromatic effects are observed. For large focus-jet separation (Fig. 3.8c)), additional aberrations also become more apparent.

Chapter 4

Generation dynamics of broadband extreme ultraviolet vortex beams

Light beams carrying orbital angular momentum (OAM) can be generated in the extreme ultraviolet and soft X-ray spectrum by means of high harmonic generation (HHG). In HHG, phase properties of the drive laser, such as curvature, aberrations and topological charge are upconverted to the harmonic beams and coherently added to the inherent dipole phase. The strong nonlinearity of the HHG process, combined with the rapid phase variations corresponding to large OAM values in these vortex beams, leads to a high sensitivity to small variations in the driving field. However, a study of the generation dynamics via an accurate reconstruction of multi-wavelength OAM beams is challenging. Here we show full complex field measurements of multiple individual harmonics of HHG vortex beams. By using spectrally resolved ptychographic wavefront sensing, we retrieve high-resolution amplitude and phase profiles for harmonics 23 to 29 in parallel, enabling detailed multi-wavelength beam reconstructions. We study the influence of generation conditions and drive laser aberrations on the resulting vortex fields by comparing measured fields to numerical simulations, and retrieve the propagation conditions around the focus and the OAM content of the beams. Specifically, we find that the multimodal content of such vortex beams can significantly influence the propagation and field distributions in the focal region. Such beam propagation analysis allows a prediction of the resulting attosecond pulse trains and associated attosecond light springs that can be generated under realistic driving conditions.

The content of this chapter has been published as: Antonios Pelekanidis, Fengling Zhang, Kjeld S. E. Eikema, and Stefan Witte, *Generation dynamics of broadband extreme ultraviolet vortex beams,* ACS Photonics **12**(3), 1638–1649 (2025).

4.1 Introduction

Light beams carrying orbital angular momentum (OAM) have been of increased interest in recent years and have been proposed for various applications [152, 153], including super-resolution microscopy [154–157], coherent diffractive imaging [37, 69], optical trapping [158, 159], communications [160–162] and quantum entanglement [163, 164]. OAM beams have a helical wavefront that mathematically is described as an azimuthal phase ramp $e^{il\phi}$, where l is the topological charge [77]. OAM light beams with controlled properties have been demonstrated for different applications in a wide spectrum ranging from infrared to X-ray [165, 166]. Especially in the extreme ultraviolet (XUV) and soft-X-ray regime, OAM beams have been extensively studied theoretically [94, 95, 167–170], and demonstrated experimentally [69, 86, 171–182] by means of high harmonic generation (HHG) [81, 131, 183–185]. For HHG OAM beams, the topological charge of the drive laser l_1 is upconverted to ql_1, where q is the harmonic order of each harmonic. The harmonic-order-proportional topological charge leads to the generation of spatio-temporal attosecond light springs [95, 96].

HHG is a fully coherent process, therefore, we can control the properties of the generated XUV and soft-X-ray beams via the drive laser. Thanks to the development of high-power ultrafast commercial lasers that render HHG broadly accessible, there has been extensive research on the configurability of HHG OAM beams. Specifically, earlier studies have demonstrated that we can achieve control over the resulting OAM of the XUV OAM beam by combining drive lasers with different topological charges [172, 175, 176, 181] and polarizations [178, 182]. It has also been shown that a drive laser with a minor impurity of its main OAM mode will lead to a large distribution of the HHG OAM modes [167, 179, 180]. Such an impurity can be caused for instance by astigmatism and other aberrations in the drive laser [179] or by fabrication limitations of the spiral phase plate (SPP) that is inserted in the drive beam in order to convert a Gaussian into OAM beam [180].

Moreover, as HHG is a coherent process, phase matching is required in order to maximize yield. Experimental parameters such as gas pressure, laser intensity, focus position and interaction length contribute to phase matching [186–188]. Phase matching conditions vary for the different quantum paths, namely the short and the long electron trajectory, with the short trajectory usually having easier phase matching conditions [86]. For OAM beams, specific studies revealed the conditions that lead to improved phase matching for HHG with a drive laser of topological charge equal to 1 [86, 170, 189]. All studies confirm that short trajectory harmonic emission has longer coherence length and hence higher HHG yield, and phase matching is better when the gas medium is behind the drive laser focus.

The wavefront of an emitted harmonic beam with harmonic order q can be modelled microscopically as $\Phi_q = q\phi + \Phi_i$, where ϕ is the wavefront of the drive laser at the generation plane and Φ_i is the dipole phase for short ($i = s$) or long ($i = l$) trajectory [91, 92, 190]. This model has been used to predict the high harmonic wavefronts for perfect single OAM mode driving beams [94, 95, 168–

170], but also for driving beams with impurities in the dominant OAM mode [167, 180]. The studies assuming a pure OAM mode in the drive laser showed that the short-trajectory harmonic emission leads to a ring-shaped far-field intensity profile with similar divergence for all emitted harmonics [95, 169]. The properties of these beams are quite constant with respect to the distance between drive laser focus and gas medium [94, 168]. However, the long-trajectory harmonic emission has a more diverse behavior as a function of laser focus-gas distance [94, 168].

HHG OAM beams have been studied experimentally with intensity-based measurements [173, 174, 189] or with single-wavelength wavefront sensors [177, 179, 180]. However, given the significant wavelength-dependence of the dipole phase and extreme sensitivity to drive laser parameters, an accurate assessment of a broadband HHG OAM beam requires a full characterization of all harmonics in terms of amplitude and phase information.

In this paper, we use spectrally resolved ptychographic wavefront sensing (PWFS) measurements [24, 61] to retrieve complex fields of HHG vortex beams at multiple individual harmonics in parallel. By performing such measurements for varying drive laser parameters, we can quantify their influence on the generated HHG OAM beams. From the measured high-resolution field information, we then reconstruct the propagation behavior around the focus and the OAM modal content, which are found to depend on the combined effect of the dipole phase and the drive laser wavefront aberrations.

4.2 Materials and Methods

4.2.1 Experimental design and setup

To test the generation dynamics, we designed a series of experiments in which we perform high-resolution PWFS measurements on high harmonic beams, while varying drive laser properties at the generation plane by adjusting the final focusing lens. Specifically, we vary the lens position along the beam propagation direction, thus changing the relative position between the beam waist and the gas jet, as well as the lens tilt angle to introduce controlled amounts of astigmatism in the fundamental beam.

Our PWFS approach [61, 63] is based on the coherent diffractive imaging concept of ptychography [24, 57], which reconstructs complex field information of an object and the incident illumination profile. By using optimized image masks, PWFS is capable of robust multi-wavelength XUV wavefront sensing of individual harmonics [63, 111], even for complex fields with high OAM [37]. In addition to the HHG wavefront sensing, we perform PWFS measurements on the fundamental beam for all demonstrated generation conditions, so that we can compare the measured HHG wavefronts with theory predictions from a single atom response model (Section 4.2.2).

The complete setup is shown in Fig. 4.1a). An ultrafast ytterbium-based NIR laser system (Pharos from Light Conversion) drives the HHG. The laser system delivers 2 mJ pulses at a center wavelength of 1030 nm, with pulse duration 170 fs and a repetition rate of 1 kHz. For efficient HHG, the pulses are compressed by a

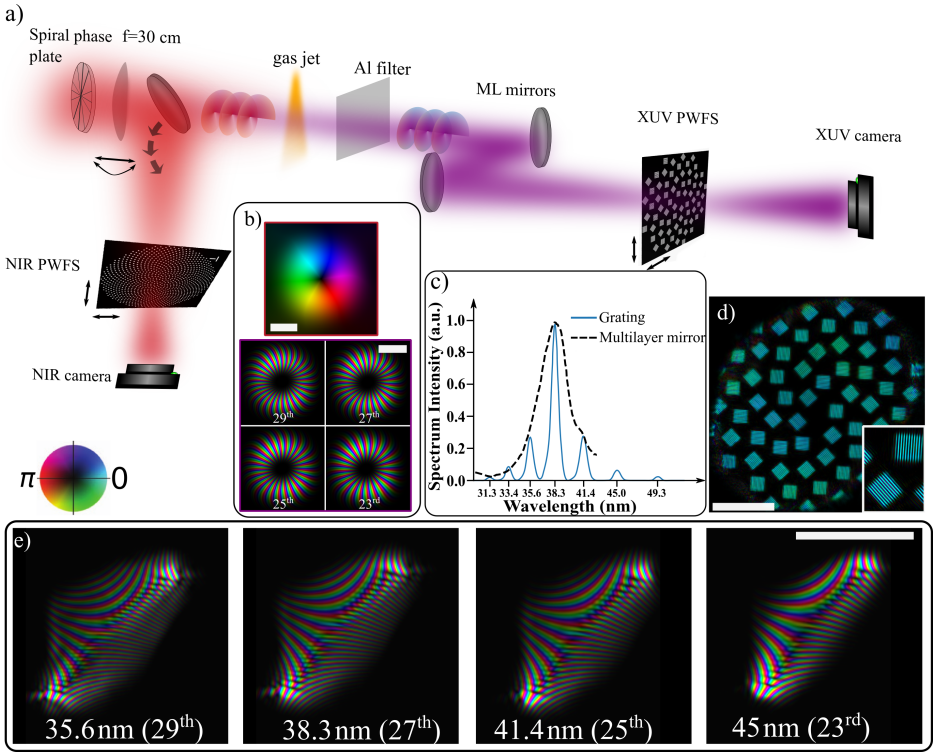

Figure 4.1: Experimental setup. a) A NIR laser with topological charge equal to 1 is focused to a gas jet to generate HHG. The high harmonics propagate to a pair of multilayer mirrors that focus the beam in the vicinity of the ptychographic wavefront sensor plane. An auxiliary beam path in front of the vacuum part is used for ptychographic wavefront sensing of the fundamental beam. b) Example of reconstructed NIR beam (top) and modelled high harmonic wavefronts at the gas jet plane (bottom) for that particular NIR beam. c) High harmonic spectrum behind the multilayer mirrors measured through diffraction from a grating, indicated by the solid line. The dashed line shows the reflectivity of the multilayer mirror pair. d) Ptychographic reconstruction of the wavefront sensor. Inset shows zoomed-in area of the object. e) Wavefronts of harmonics 23 to 29 at measurement plane. In b), d) and e) brightness indicates the amplitude and hue the phase, according to the colormap in the left of the figure. Scale bars in all figures correspond to 50 µm.

home-built pulse compression system to a duration ≈45 fs with an average power of 1.5W [108]. The NIR beam, with FWHM diameter equal to 6 mm, is sent through a spiral phase plate (Vortex Photonics V-1064-20-1) giving topological charge equal to 1 at a nominal wavelength 1064 nm, and is subsequently focused by a 300 mm lens into a jet with 1 mm diameter, filled with argon at a backing pressure of 5 bar. Moreover, an iris with diameter equal to 7.7 mm clips the beam before the focusing lens in order to maximize the HHG flux [191].

Behind the focusing lens a flip mirror can send the beam to an auxiliary beam path, where we perform the PWFS of the fundamental beam at a plane that corresponds to the vicinity of the gas jet. The NIR wavefront sensor is a binary object with 4 µm square holes arranged in a golden spiral configuration of total width 400 µm. The diffraction patterns from the NIR wavefront sensing measurement are recorded by a CCD camera (AVT GT3400, 3384×2704 pixels, pixel size 3.69 µm, 14-bit dynamic range) placed 12.5 mm behind the wavefront sensor.

Within the main beam path an aluminum filter blocks the drive laser and transmits the generated high harmonics, which are then focused by a pair of plane and curved (ROC=500 mm) molybdenum/silicon multilayer mirrors (optiXfab GmbH) onto the wavefront sensor. The HHG spectrum, shown in Fig. 4.1c), is shaped by the efficiency of the multilayer mirrors and includes seven wavelengths ranging from 31 nm to 50 nm. The wavefront sensor is a scaled version of the one proposed in [63], and consists of 10 µm apertures with four orientations and 1 µm pitch gratings inside each aperture. An example of the ptychographic reconstruction of the object is shown in Fig. 4.1d). A CCD camera (Andor Ikon-L 936SO, 2048×2048 pixels, pixel size 13.5 µm, 15-bit dynamic range) is placed approximately 107 mm behind the sample. The numerical aperture of the ptychographic setup is 0.129, leading to a diffraction-limited resolution of 148 nm for the central HHG wavelength of 38.3 nm.

4.2.2 Single atom response model

The reconstructed fundamental complex electric field can be used to estimate the high harmonic wavefronts. Here we adopt the single atom response (SAR) [91, 92] that gives expressions for both the amplitude A and the phase Φ of each high harmonic q in the plateau region:

$$A_q(x,y) = A_f(x,y)^p \tag{4.1}$$

$$\Phi_q(x,y) = q\phi(x,y) + \Phi_i(x,y) \tag{4.2}$$

$$\Phi_i(x,y) = \alpha_i I(x,y) + \frac{\gamma_i}{I(x,y)}(q\omega - \Omega_p)^2 \ + \ const. \tag{4.3}$$

In the above expressions, $A_f(x,y)$ and ϕ are the amplitude and phase of the fundamental beam at the generation plane, and Φ_i is the dipole phase. For the calculation of the spatial distribution of the dipole phase, I and ω are the intensity and frequency of the fundamental laser respectively, and Ω_p is a frequency associated with the ionization potential I_P of the gas $\Omega_p = I_p/\hbar$. The parameter values used to describe the amplitude and short-trajectory dipole phase are taken from [92], with a wavelength scaling for a 1030 nm drive laser wavelength where applicable: $\gamma_s = 0.795 \times 10^{-18}\mathrm{s}^2\mathrm{W}\cdot\mathrm{cm}^{-2}$, $\alpha_s = 0$ and $p = 4$. This model for the dipole phase has been used in previous studies to describe chromatic aberration effects in HHG Gaussian beams and transfer of aberrations from drive beam to the high harmonics, and was in agreement with experimental findings [63, 111]. Figure 4.1b) shows an example of the predicted HHG wavefronts for the four brightest harmonics (23^{rd} to 29^{th} harmonic), using the reconstructed drive laser

information as input for the single atom response model.

4.2.3 Ptychographic reconstruction of high harmonic wavefronts

For the ptychographic wavefront sensing we have placed the object on a translation stage that can move laterally to the beam (Smaract SLC-1730) and acquired a series of 218 diffraction patterns with the object moving in a concentric scan grid covering a field of view equal to 104 µm with an average step size equal to 6 µm. The ptychographic reconstructions are performed via Ptylab.py [110]. The overlap factor, using the definition of the overlap presented in [37], is equal to 68%. The relatively low overlap factor given the complexity of the reconstruction problem with seven unknown structured wavefronts creates some uncertainties in terms of the reconstructed topological charges. Specifically, while the topological charge for every wavelength should be equal to the respective harmonic order, when the drive laser's topological charge is equal to 1, the reconstructed topological charges are in the range between harmonic order ±2. Examples of independently reconstructed beams from the same dataset that exhibit different topological charge are shown and discussed in Appendix 4.5.1. Therefore, the results shown in the following section are based on a constrained reconstruction process, such that the topological charge of each probe, calculated during the reconstruction process as $l = \frac{1}{2\pi} \oint_C d\phi$ [97], is fixed according to the HHG upconversion rule for the topological charges. While the topological charge is a single value that is set by physical properties of HHG, the OAM of the harmonics can be influenced by the generation conditions. As the nonlinear conversion process will influence the exact amplitude and phase profiles of each high harmonic wavefront, the harmonics can carry a distribution of OAM values with a central value that may deviate from the topological charge [167, 179, 180]. The OAM distribution can then be calculated via an azimuthal Fourier Transform (FT) of the complex electric field on a circular path along the beam [180] or via a Laguerre-Gaussian decomposition [179].

4.2.4 Correction of multilayer mirror effects on wavefronts

The presence of the refocusing optics needs be considered for the numerical propagation of the HHG beam between the generation plane and the wavefront sensor plane. The indicated angle of incidence for maximized reflectivity is 5 degrees. For the plane mirror, we assume that there is perfect reflection and neglect any surface defects. However, oblique incidence on the curved mirror leads to astigmatism, as can be clearly observed in the example ptychographic reconstruction of the vortex probes in Fig. 4.1e). The induced astigmatism to the wavefront is equal to $\frac{\eta^2}{2r}(y^2 - x^2)$, with η the incidence angle and r the radius of curvature of the mirror [192]. In practice, the beam has a slight elevation angle and the incidence angle can deviate from exactly 5 degrees for alignment purposes. Therefore, the astigmatism contribution can only be estimated such that the astigmatism-corrected wavefronts have physically reasonable profiles at the fo-

cus, which is an image plane of the generation position. It is also convenient to perform amplitude comparisons between modelled and experimental results at the curved multilayer mirror plane, as the beam intensity profile has not been affected by the astigmatism induced by the curved multilayer mirror. Since the PWFS measurements give high-resolution representation of both the amplitude and phase of the high harmonic wavefronts at the object plane, we can get beam information at the curved multilayer mirror plane via numerical propagation of every reconstructed wavefront assuming paraxial approximation. The numerical propagation can be performed, for instance, with the scaled angular spectrum propagator [120].

4.3 Results and Discussion

4.3.1 Dependence of the HHG beam profiles on the drive laser properties

Firstly, we investigate the HHG beam amplitudes as a function of the laser focus position relative to the gas medium. The measured and reconstructed complex fields of harmonics 23 to 29 are numerically propagated back to the curved mirror plane and compared to simulations. In Fig. 4.2a) we show the results for 3 example laser focus positions (-2.9 mm, -1.5 mm and +1.36 mm), while results for more positions are shown in Appendix 4.5.2. From Fig. 4.2a) we observe the same trend with respect to the rim thickness as modelled in [94], with a single thick ring for the cases when the drive laser focus position is behind the gas medium, whereas the HHG beams exhibit a thinner rim of the main ring and secondary rings with larger diameter when the gas is on the divergent side of the drive laser. The secondary rings appear to be clipped due to an added aluminum foil that was intended to block leaking fundamental light through the flat multilayer mirror towards the camera, but still the presence of these rings is clear, especially in the short wavelengths. In Fig. 4.2a) we also show comparative results from expected far-field high harmonic beam profiles using the SAR model described in section 4.2.2. The drive laser's beam profile at the generation plane assumed in the model is a reconstructed beam from the auxiliary drive laser path shown in Fig. 4.1a), which we numerically backpropagated to different distances along the focus, in order to simulate the generation conditions for varying laser focus positions. Due to small beam drifts between HHG and NIR wavefront sensing measurements, we numerically corrected some of the aberrations in the drive laser at the focusing lens plane before propagating to the respective generation plane and applying the SAR model. The Rayleigh length has been calculated to be approximately 6 mm, so the experiment covers a range of about half a Rayleigh length in both directions from the drive laser focus.

We find that the model captures the trend of the experimentally derived beam profiles' behavior as a function of the laser focus position. For focus positions in front of the gas we predict a thin bright ring and secondary rings with higher divergence, which are more profound for the short wavelengths. On the other hand, when the drive laser focus position is behind the gas, we predict a sin-

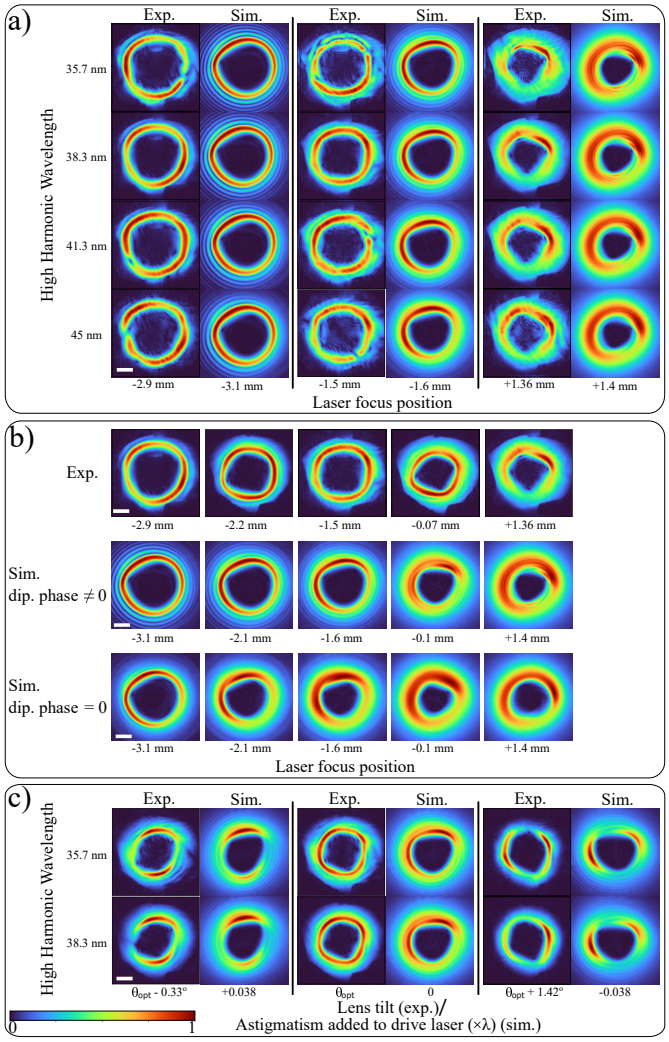

Figure 4.2: Reconstructed and modelled beam amplitudes for four harmonics ranging from 35.7 nm (29^{th} harmonic) to 45 nm (23^{rd} harmonic) at the curved multilayer mirror plane for various generation conditions. a) Beam amplitudes for varying laser focus positions with respect to the gas medium. Positive (negative) laser focus positions means that the laser focus is downstream (upstream) of the gas jet position. b) comparison of reconstructed and modelled beams for 27^{th} harmonic with and without the dipole phase contribution in the model. c) Beam amplitudes of harmonics 29 and 27 for varying tilt positions of the focusing lens. The beam profiles for lower harmonics are similar, and shown in Appendix 4.5.2, along with results for more lens tilt positions. The absolute laser focus positions for experimental data in a) and b) are approximate, based on the fit with the modelled results. Scale bars in all figures are equal to 3 mm.

gle ring with increased rim thickness. We should note here that these results consider only short electron trajectory contributions to the HHG, as long trajectories have very short phase matching length [86] and their efficiency is considered negligible for our generation conditions. In previous work, secondary rings were predicted [94] and observed [174] for positive laser focus positions, and associated to long trajectories. The appearance of ring structures attributed to long trajectory emission has some analogy to experimental studies [89, 193] for Gaussian beams. It is likely that the shorter Rayleigh length and longer medium used in our HHG setup results in phase matching conditions that suppress the long trajectories. The influence of the dipole phase of the short trajectory is illustrated in Fig. 4.2b), where we compare far-field HHG profiles for different γ_s values in the SAR model for the 27^{th} harmonic, with $\gamma_s = 0.795 \times 10^{-18}\text{s}^2\text{W} \cdot \text{cm}^{-2}$ and $\gamma_s = 0$. From this figure it can be seen that the secondary rings are caused by the dipole phase and subsequent beam propagation. For reference, in Appendix 4.5.3 we present modelled HHG wavefronts that would correspond to long electron trajectories. For the specific drive wavelength, pulse duration and pulse energy in our experiments we observe that the wavefronts associated to long trajectories would diverge strongly and not be captured by the refocusing optics. In Appendix 4.5.2 we also show far-field beam intensities from short trajectory contributions, when the drive beam is an ideal circularly symmetric non-aberrated vortex beam. In the case of this ideal drive beam, the far-field HHG beam profiles for varying drive laser focus positions with respect to the generation plane closely resemble other theoretical results [94], with secondary rings not present in the beam. Therefore, our conclusion is that the experimentally observed rings (Fig. 4.2a)) are caused by the combination of focusing geometry, fundamental beam profile and dipole phase. Note that this conclusion does not exclude the possibility of forming additional rings in a geometry where long trajectories are generated more efficiently.

Similarly, in Fig. 4.2c) we compare experimental and model results for varying astigmatism of the drive laser. For these measurements, the distance between the gas jet and the non-aberrated laser focus was set to -0.54 mm. The astigmatism is adjusted by tilting the focusing lens in a controlled way in a range of 1.75° around the optimized tilt denoted as θ_{opt}. This optimized tilt angle leads to a polychromatic HHG beam at the camera with the most uniform intensity around the ring. We model the astigmatism by numerically adding astigmatism in the beam used to generate the simulated results in Fig. 4.2a). We observe a close similarity of the beam amplitudes, with the doughnut shape of the HHG beams transforming into two bright lobes either on the vertical or horizontal direction. Note that adding drive laser astigmatism of only 0.038λ already leads to the emergence of bright lobes in the HHG beams, due to the strong nonlinearity of the upconversion to the high harmonics.

4.3.2 Propagation of vortex beams around a focus

As mentioned in Section 4.2.4 the phase of the HHG beams can be corrected at the curved multilayer mirror plane for each investigated generation condition if

we numerically remove the astigmatism induced by the mirror due to the non-zero angle of incidence. Since the precise astigmatism of the mirror is not known with sufficient accuracy, we used fitted astigmatism coefficients for the results shown henceforth such that they maximize the OAM modal purity of the most circular and azimuthally homogeneous beam profile from the beam profiles of Fig. 4.2a). This assumption implies that a beam with amplitude profile that resembles a pure $\mathrm{LG}_{q,0}$ mode, with q the harmonic order, is more likely to have phase that corresponds to a pure $\mathrm{LG}_{q,0}$ mode, too. We selected the 27^{th} harmonic (38.3 nm) from the dataset that corresponds to laser focus position -1.5 mm as the beam with maximized OAM purity, which gave astigmatism coefficients equal to $\alpha_1 = 4.959k{\cdot}10^{-3}$ and $\alpha_2 = -4.934k{\cdot}10^{-3}$, with k the wavenumber for the 27^{th} harmonic and α_1, α_2 such that $\Phi_{astigm\,correction} = e^{-i\left(\alpha_1\rho^2\cos(2\phi)+\alpha_2\rho^2\sin(2\phi)\right)}$, where ρ and ϕ are the polar coordinates. For reference, the expected astigmatism according to [192], for angle of incidence equal to 5 degrees and radius of curvature equal to 50 cm, is $7.62k \cdot 10^{-3}(x^2 - y^2)$.

In Fig. 4.3 we show example propagation plots of the four reconstructed harmonic beams along the measurement plane without (Fig. 4.3a)) and with (Fig. 4.3b)) the astigmatism correction, starting from the reconstructed fields for the laser focus position at -1.5 mm. We show two different cross sections, the xz and yz planes, as well as two-dimensional amplitude plots at selected planes. In Appendix 4.5.4 we show propagation results across the diagonal cross sections as well, where we see similar behavior as in the xz and yz planes. Figures 4.3c-g) show in-plane plots of the 27^{th} harmonic at different planes along the focus position. The astigmatism from the spherical multilayer mirror leads to distorted beam profiles, where at some planes the doughnut shape has degenerated into a thin line (Figs. 4.3d) and f)). After removing the astigmatism term at the multilayer mirror plane and propagating again forward along the focus, all harmonic beams maintain the doughnut-shaped amplitude profile and can be refocused to a smaller spot size (Figs. 4.3h-l)). However, even for the numerically corrected beams for the astigmatism from the spherical multilayer mirror, we observe in Figs. 4.3h-l) that there is a slight intensity variation across the beam as the beam propagates along the focus. This is an indication of a remaining OAM modal impurity, with the coherent superposition of the different OAM modes creating this intensity variation effect.

Figure 4.4 shows the propagated beams around the focal region for different laser focus positions. Propagation is performed directly with the retrieved fields (Fig. 4.4a)) and after numerical astigmatism removal (Fig. 4.4b)). While the retrieved field results do not require an assumption on the mirror-induced astigmatism, the corrected fields provide better insight into the HHG beam properties at the vicinity of the generation plane. Figures 4.4e-g) show overlapped, for different laser focus positions, in-plane plots of the 27^{th} harmonic at 3 planes around the focus. From these reconstructions, we find that the rim width and the ring diameter of the vortex beams are influenced by the laser focus position in different ways. These quantities are plotted in Fig. 4.4e): the diameter is measured between intensity maxima, and the rim thickness is defined as the FWHM, both azimuthally averaged. The focal plane of the HHG beam is taken as the plane

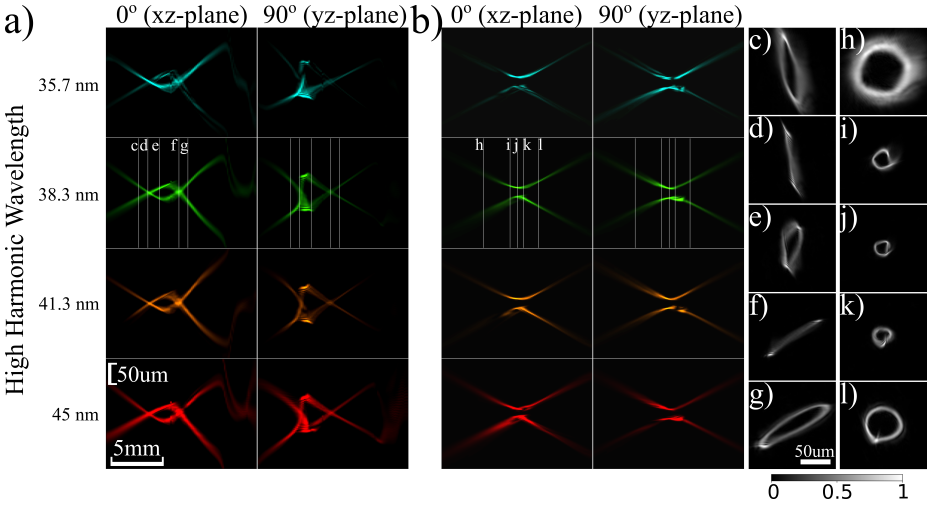

Figure 4.3: Propagation of harmonic beams along the focal plane after refocusing. a,b) Cross sections along horizontal and vertical cuts for a) the reconstructed wavefronts from the PWFS measurement, b) the astigmatism-corrected beams at the curved multilayer mirror plane which are subsequently forward propagated around the focus, c-g) in-plane amplitude profiles of the 27^{th} harmonic (38.3 nm) for planes denoted in the second row of a), h-l) same as (c-g), for the astigmatism-corrected beams at planes denoted in b). Scale bars are shared between (a-b) and (c-l).

where the diameter is minimized. Using these two parameters to describe the OAM beams, we observe that the drive laser focus position affects both diameter and rim thickness, as shown in Fig. 4.4c) and Fig. 4.4d) for experiment and model respectively. The model is based on the drive laser that was used to generate the amplitude results of Fig. 4.2a).

A striking feature is the local increase in rim thickness near the focal plane, which depends on the generation conditions. The simulations are in agreement with the experiment and can qualitatively explain this feature. In the simulations, the peak in rim thickness coincides with the generation plane. The amplitude of the HHG beams at the generation plane is modelled as the drive laser amplitude to the power 4 (which is typical in the strong-field approximation). In Fig. 4.4h) we show a simplified simulation example to better explain the HHG beam behavior around the generation plane. Taking the drive laser as a pure $\text{LG}_{1,0}$ mode, the 29^{th} harmonic will have the amplitude and phase profile of the beam shown at the left panel of Fig. 4.4h) at the generation plane. Compared to a pure $\text{LG}_{29,0}$ mode (right panel of Fig. 4.4h)), such a beam has a clear difference in the rim thickness. Therefore, the 29^{th} harmonic should be described as a superposition of different radial modes $\text{LG}_{29,n}$ [179], which at the generation plane are coherently added to create a ring with increased thickness. However, as this beam propagates, the radial modes have different relative phases and are no longer added constructively. This effect causes the rim to become narrower initially, as it is

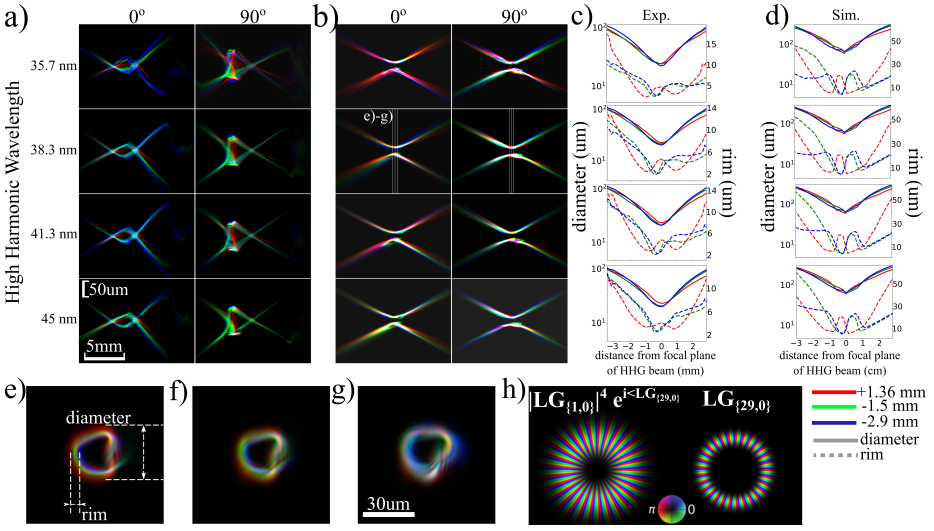

Figure 4.4: Propagation of harmonic beams along the focal plane after refocusing, overlapped for different drive laser focus positions. Red: +1.36 mm, green: −1.5 mm, blue: −2.9 mm. a,b) Cross sections along horizontal and vertical cuts for a) the reconstructed wavefronts from the PWFS measurement, b) the astigmatism-corrected beams at the curved multilayer mirror plane which are subsequently forward propagated around the focus, c-d) Experimental and model results for the variation of diameter and rim thickness, as defined in (e), of the astigmatism-corrected beams, for different wavelengths and generation conditions. In (a-d) all horizontal rows are aligned and correspond to the same wavelength. e-g) overlapped in-plane amplitude profiles of the 27$^{\text{th}}$ harmonic (38.3 nm) for planes denoted in the second row of b), h) example of a 29$^{\text{th}}$ harmonic beam driven by a $LG_{1,0}$ fundamental laser (left) compared to a $LG_{29,0}$ mode (right). Brightness indicates amplitude and hue the phase. a-b) and e-g) share the same scale bar.

mainly determined by the dominant $LG_{29,0}$ mode, until it starts expanding again due to propagation. The effect of the dipole phase is a local divergent wavefront on the rim, which favors the expansion of the rim and partially counteracts the aforementioned effect. Further insight on the effect of the dipole phase is given in Appendix 4.5.4, where we show modelled results excluding the contribution of the dipole phase.

The reasoning above also explains the position of this local maximum in rim thickness relative to the HHG focal plane. The rim local maximum occurs at the generation plane, where the phase properties of the drive laser are transferred to the harmonic wavefronts. Therefore, for positive laser focus positions, the harmonic beams have a converging phase and the focus is real and downstream of the generation plane, whereas for negative laser focus positions the harmonic beams are diverging at the generation plane and have a virtual focus. Note that the scales are different between experiment and model, because experiment has been conducted at the (corrected) image plane with a demagnification ratio of

2.76 between gas jet and image plane.

The comparison between experimental and modelled results shown in Figs. 4.4c,d) can provide insight on the exact value of the non-perturbative scaling power p in Eq. 4.1, as p can vary depending on the generation conditions and other values have been proposed except $p = 4$ [94]. However, as the modelled results presented in Fig. 4.4d) have been calculated with the SAR model, a more quantitative comparison between experimental and simulated results can only be accurate for HHG configurations with a thin generation medium, where phase matching conditions can be excluded. In our experiments, we can safely consider the generation medium to be thin compared to the drive laser's Rayleigh length, but still such a quantitative comparison would likely require a more accurate modelling of the HHG process [90].

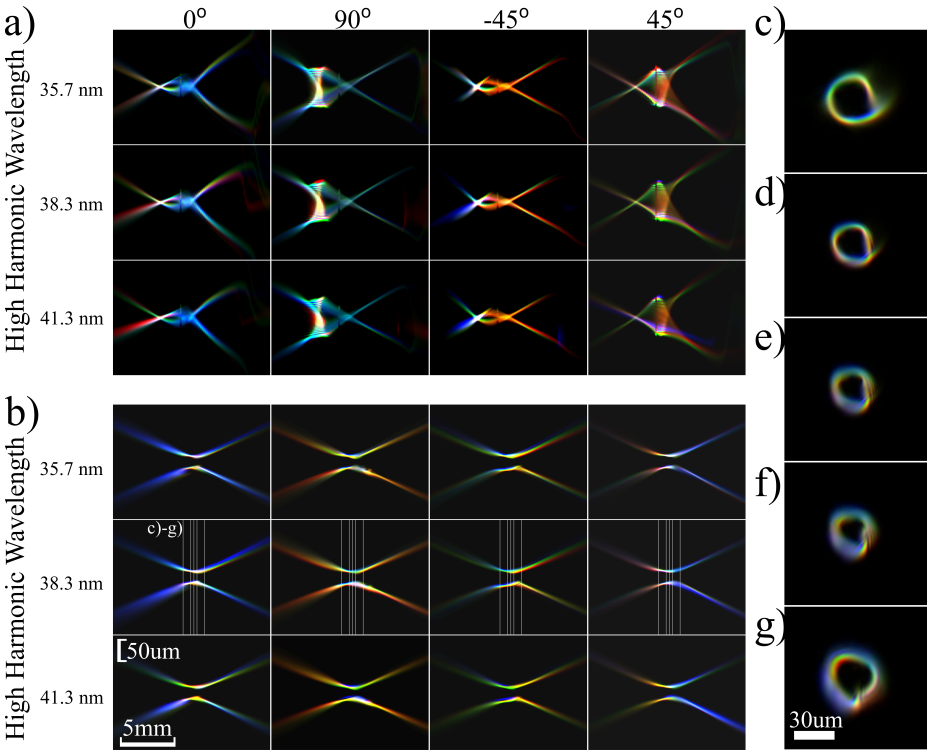

Figure 4.5: Propagation of harmonic beams along the focal plane after refocusing overlapped for different astigmatism levels of the drive laser. Lens tilt positions of red: $\theta_{opt} - 0.33°$, green: θ_{opt}, blue: $\theta_{opt} + 1.42°$. a,b) Cross sections along different cuts (horizontal, vertical and diagonal) for a) the reconstructed wavefronts from the PWFS measurement, b) the astigmatism-corrected beams at the curved multilayer mirror plane which are subsequently forward propagated around the focus, c-g) overlapped in-plane amplitude profiles of the 27^{th} harmonic (38.3 nm) for planes denoted in the second row of b).

The influence of drive laser astigmatism on the harmonic beam propagation

around the focal region can also be visualized using overlapping propagation plots (Fig. 4.5). In Figs. 4.5a,b) we show overlapped propagated beams that correspond to different astigmatism levels of the drive laser. Here we do not show results for the 23$^{\text{rd}}$ harmonic (45 nm), because of the lack of reconstruction for that harmonic from lens tilt equal to $\theta_{opt} + 1.42°$. We notice that, when the drive laser is astigmatic, leading to harmonic beams denoted as red and blue curves, there is clear presence of lobes that dominate on the y direction for negative lens tilt (red curve), and on the x direction for positive tilt (blue curve). Also on the diagonal directions, the lobes rotate from one direction to the other as the beam propagates through the focus. In Appendix 4.5.4, we show individual plots of the in-plane overlapped plots of Fig. 4.5c-g), in order to have clear visualization of the beam properties for each generation condition.

4.3.3 OAM modal purity analysis

Another important aspect that we can investigate via the spectrally resolved PWFS technique is the OAM modal content and purity and how they vary with the generation conditions. For this purpose we have numerically propagated the wavefronts to the curved multilayer mirror plane and removed the astigmatism caused by the off-axis mirror reflection, as was calculated in Section 4.3.2, as well as remaining tip, tilt and defocus phase terms before calculating the OAM modal content.

As mentioned in Section 4.2.3, the modal content can be calculated by either performing azimuthal FT or through LG decompositions. Due to the slightly elliptic beam profiles, we estimate that the LG decompositions, presented in Fig. 4.6, can give more accurate conclusions, as azimuthal FT along a circular path on an elliptical beam may underestimate the actually present OAMs. However, for comparison reasons we provide an example of the angular FT method for the case of a circular beam in Appendix 4.5.5, showing very similar results to the LG decomposition. We perform the OAM modal content calculation at the curved multilayer mirror plane for convenience, as it is the reference plane where we correct the effect of the refocusing optics. However, the LG decomposition would be equivalent at any other plane, since the LG modes are solutions to the Helmholtz equation and are propagation-invariant.

Figure 4.6a) displays the experimentally retrieved complex fields of the 27$^{\text{th}}$ harmonic for different laser focus positions, together with the OAM modal content from the experimental data and SAR model results. The OAM modal content of the other reconstructed harmonic beams between 35.7 nm and 45 nm is shown in Fig. 4.6b). The selected laser focus positions are the same five positions with respect to the gas medium as in Fig.4.8. For the experimental data, we use a truncated basis of LG modes including 5 radial modes, similar to [179], and 42 azimuthal modes, whereas for modelled results we use fewer azimuthal modes for computational efficiency. We calculate the basis modes and the coefficients individually for each harmonic beam in our analysis, such that the fitting error between the actual beam and its modal description is minimized. As the LG decomposition gives the coefficients c_{mn} of the complete basis for azimuthal modes

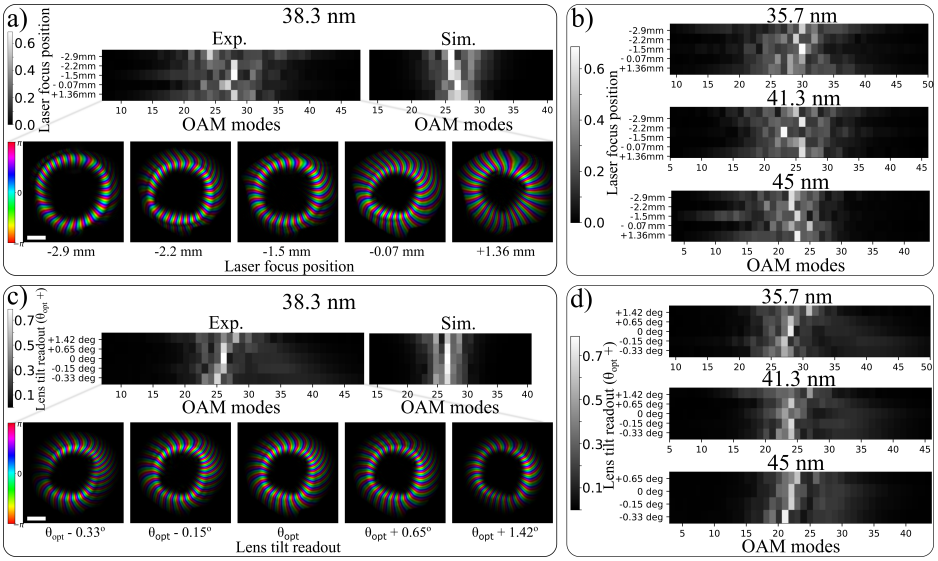

Figure 4.6: Orbital angular momemtum (OAM) modal content of experimental HHG wavefronts for varying drive laser focus positions with respect to the gas medium. a) top: OAM calculated for the 27$^{\text{th}}$ harmonic (38.3 nm) and compared to modelled results. bottom: complex-valued visualization of the 27$^{\text{th}}$ harmonic that gave the above LG decomposition. b) OAM content calculated for three harmonic wavelengths, besides the 27$^{\text{th}}$ harmonic. c,d) same as a,b) with results from drive laser astigmatism scan. For the beam plots in a,c), brightness indicates amplitude and hue the phase. The scale bars are equal to 3 mm.

m and radial modes n, we calculate the OAM modal content C_m by summing the coefficients with the same m index $C_m = \sqrt{\sum_n |c_{mn}|^2}$. In Appendix 4.5.5 we show the complete LG decomposition c_{mn} for the 27$^{\text{th}}$ harmonic and laser focus position -1.5 mm, where we observe that most energy is included in the radial modes with $n = 0$.

The OAM modal content depends on the generation conditions, with the purity being maximized at the laser focus position equal to -1.5 mm (see Section 4.3.2). In principle, a broadening of the OAM can be either due to an inhomogeneity in the drive laser amplitude distribution along the vortex ring, or due to a deviation of the (unwrapped) phase from a linear behavior in the azimuthal direction. From simulations, the strongest influence is found to result from phase effects, and we attribute the OAM broadening that is shown in Figs. 4.6a,b) predominantly to phase aberrations. As discussed in Section 4.2.2, the phase of an HHG wavefront is the sum of the drive laser intensity-dependent dipole phase and the drive laser phase, which both vary significantly with respect to the drive laser focus position. LG decomposition results of modelled HHG OAM beams also give a broadening of the OAM modal content for certain laser focus positions. The simulation results in Fig. 4.6a) show qualitative agreement with the experimental data, but

the variations with laser focus position are not fully reproduced.

The dependence of OAM modal content on drive laser astigmatism is shown in Figs. 4.6c,d). For increasing astigmatism, we observe a broadening of the OAM distribution. In addition, there appears to be a small linear increase of the mean OAM value as a function of lens tilt. The OAM broadening, which is qualitatively reproduced by the simulations, is related to the impurity that is injected to the pure LG_q, with q the harmonic order, when an astigmatism phase term and an amplitude modulation are added to an azimuthally symmetric beam. The astigmatism phase term leads to local deviations from the linear azimuthal phase ramp for an ideal LG_q mode, resulting in variations in OAM. However, from symmetry considerations, any effect of the lens tilt should be independent of the sign, as a positive and negative lens give rise to the same induced astigmatism. SAR simulations of the drive laser beam as pure $LG_{1,0}$ mode with added astigmatism confirm that expectation. Therefore, the observed linear trend is likely due to other experimental uncertainties resulting from changes in lens alignment, which may influence both the fundamental wavefront and the HHG process. Determining the origin of this OAM variation will require further study.

4.3.4 Synthesis of attosecond pulse trains

The spectrally resolved amplitude and phase reconstruction of multiple high harmonics enables the reconstruction of the attosecond pulse train (assuming the harmonics are phase-locked) by Fourier-transforming the reconstructed frequency-domain fields to the time domain. For ideal drive laser conditions, the attosecond pulse is expected to form a double-sided helix [95, 96]. However, the influence of dipole phase and drive laser aberrations to the HHG wavefronts can distort the double helix structure. In Appendix 4.5.6 we show synthesized attosecond pulse trains from the reconstructed harmonic wavefronts under certain assumptions for the spectral phase that would correspond to Fourier-transform limited pulses. However, a conclusive analysis would require a measurement that is sensitive to the relative phase between the harmonics [194].

4.4 Conclusion

In conclusion, we have utilized the spectrally resolved PWFS method for characterizing HHG OAM beams for different generation conditions. We showed how changing the laser focus position with respect to the gas jet leads to different far field HHG beam profiles. We attributed this behavior to the dipole phase associated with the short electron trajectory. Furthermore, any astigmatism in the drive laser is upconverted to the high harmonics such that even a slight astigmatism of the drive laser leads to the emergence of bright and dark areas along the doughnut-shaped beam. Except for observations related to the amplitude of the HHG beams, we could investigate more properties of the multi-wavelength vortex beams under the assumption that we know precisely the astigmatism induced by the refocusing optics. The influence of laser focus position and drive laser aberrations around the focal region could be characterized in this way. By

performing LG decompositions on the beams for each generation condition, we found that these differences can be also associated with broadening of the OAM modal content of the beams. Finally, we proposed a simplified approach to reconstruct the attosecond pulse train for different generation conditions, assuming prior knowledge on the spectral phase. In Appendix 4.5.6 we show results from this approach, where we observed how impurities in the OAM modal content distort the double-helix light spring structure that is theoretically predicted in [95, 96]. In particular, aberrations in the harmonic fields are found to lead to a modification of the double helix structure, both in intensity and position.

Overall the PWFS method is a high-fidelity technique for characterizing multiple HHG wavefronts with high resolution from a single measurement, and in this work we have extended this capability to highly structured XUV beams carrying high topological charge. The complex-valued reconstructions of the wavefronts enable numerical backpropagation to the generation plane, where we can study the upconversion mechanisms and experimentally validate theoretical models about the generation of such XUV vortex beams.

An interesting follow-up of this work could be on performing PWFS measurements for more complex multi-wavelength vortex HHG beams, such as the beams demonstrated in [172, 175, 176, 178, 181, 182]. In these cases, the topological charge values of the harmonics are relatively unknown and we would need to implement unconstrained ptychographic reconstructions in terms of the topological charge values. Preliminary PWFS measurements with single-wavelength HHG vortex beams, not presented in this work, showed that, for this less complicated parameter space, the topological charge was reconstructed accurately without any prior knowledge requirement on the topological charge. Furthermore, for multi-wavelength Gaussian beam PWFS, we have demonstrated high-fidelity unconstrained wavefront reconstructions by increasing the overlap factor between adjacent scan positions to a value above 90% [63]. Therefore, we believe that PWFS on more complex multi-wavelength vortex HHG beams is possible, but would require many scan positions in order to satisfy a high overlap factor, and possibly high exposure times, so that the recorded diffraction patterns have high SNR even for the first- and second-order diffraction signal. The design and implementation of such a measurement requires a very stable HHG beam in terms of long-term beam drifts and intensity fluctuations.

This work on HHG vortex beams generated by a single vortex drive beam offers an insight on how critical parameters such as drive laser focus and aberrations can be in achieving desired properties for the attosecond pulse. We believe that this work is a first step towards more efficient design and experimental implementation with attosecond OAM beams.

4.5 Appendix

4.5.1 Ptychographic reconstruction without constraint on topological charges

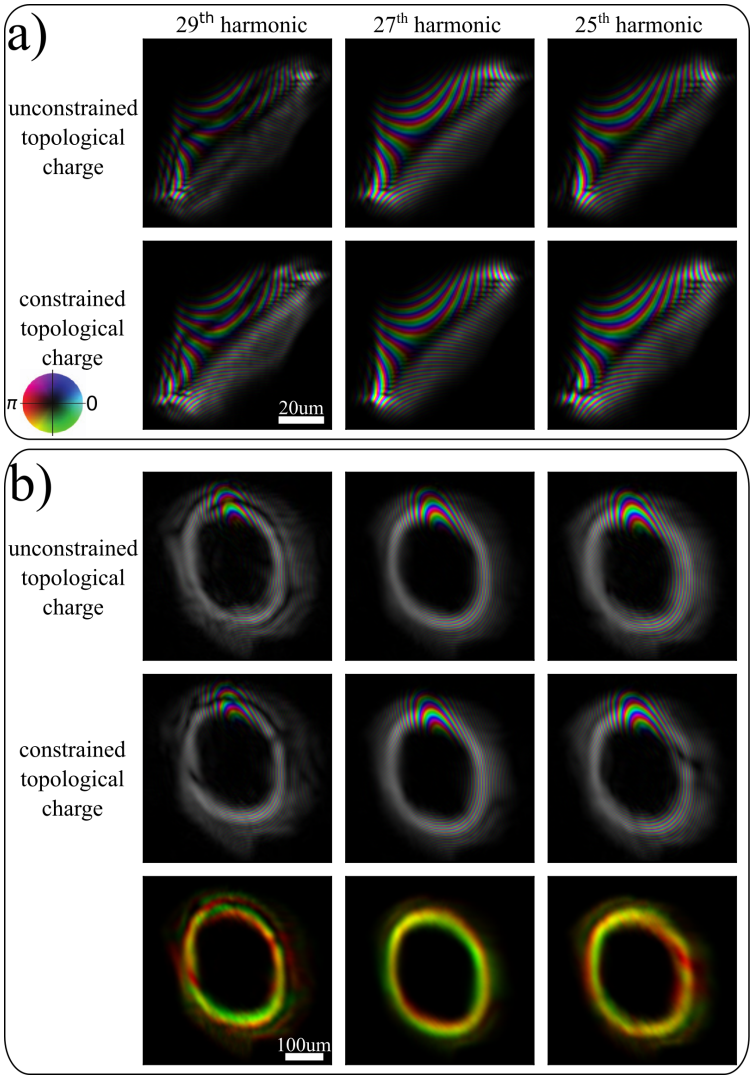

Figure 4.7: Reconstructed beams with and without imposing constraints on the topological charges. a) Complex-valued plots of the reconstructed beams for three harmonics ranging from 35.7 nm (29^{th} harmonic) to 41.3 nm (25^{th} harmonic) at the PWFS plane. All figures share the same scale bar. b) Propagated beams from a) to a plane 10 mm upstream, where the beam shape looks more like a doughnut. Topological charges are calculated as (29,27,25) from the constrained reconstruction, and (27,25,23) from the unconstrained reconstruction, for harmonics (29,27,25) respectively. The last row shows overlapped intensity plots of the uncostrained (red) and constrained (green) results. All figures share the same scale bar.

As mentioned in Section 2.3 of the main text, the resulting topological charges of the reconstructed harmonic wavefronts may vary between independent recon-

structions, due to the low overlap between scan positions and the complexity of the beams. In Fig. 4.7a) we show example reconstructions of wavefronts with the correct and incorrect topological charges. The correct topological charges were achieved via imposing constraints during the reconstruction process. We observe that the intensity profile of the beams at the ptychographic wavefront sensor (PWFS) plane exhibits large areas of low intensity and fast fringe-like features at the vicinity of the bright lobes. This structure of the beams renders the wavefront reconstruction very sensitive to the the phase, which is undefined when intensity values are (near) zero.

In Fig. 4.7b) we show backpropagated beams to a plane where the beam profile has a doughnut shape and the topological charge can be calculated via integration following a closed loop with non-negligible intensity values. Overlapping the intensity plots between correct and incorrect reconstructions reveals that even a difference of 2 between topological charges does not affect strongly the beam propagation behavior. Therefore, we consider that a deviation of ± 2 in the resulting topological charge of the reconstructed beams is to be expected and a constraint on the topological charge during the reconstruction was necessary to further constrain the reconstruction process and lead to a unique solution.

4.5.2 HHG far field beam amplitudes for varying generation conditions

Laser focus position scan

To complement Fig. 4.2a) of the main manuscript in which we showed data for 3 lens positions, Fig. 4.8 presents results from the complete dataset of 5 lens positions that aimed to investigate how the drive laser focus position with respect to the gas jet affects the HHG beam amplitudes in the far field. Experimental results in Fig. 4.8a) can be compared with simulation results (Fig. 4.8b)). We observe a close agreement between simulations and experiment, especially with related to the rim thickness and the presence of secondary concentric grids.

Drive laser astigmatism scan

Complementing Fig. 4.2c), Fig. 4.9 displays results from the complete dataset of 5 lens tilt positions that lead to different astigmatism levels of the drive laser. The experimental results (Fig. 4.9a)) can be compared with simulation results (Fig. 4.9b)).

Laser focus position scan for ideal drive beam

In the main text we have shown that the exact drive beam properties influence the far-field HHG beam intensity profiles, with secondary rings appearing when the drive laser focus position is upstream of the generation plane. We have also shown that the presence of the rings can be explained and modelled considering only short trajectory contributions within the HHG process. In this section we

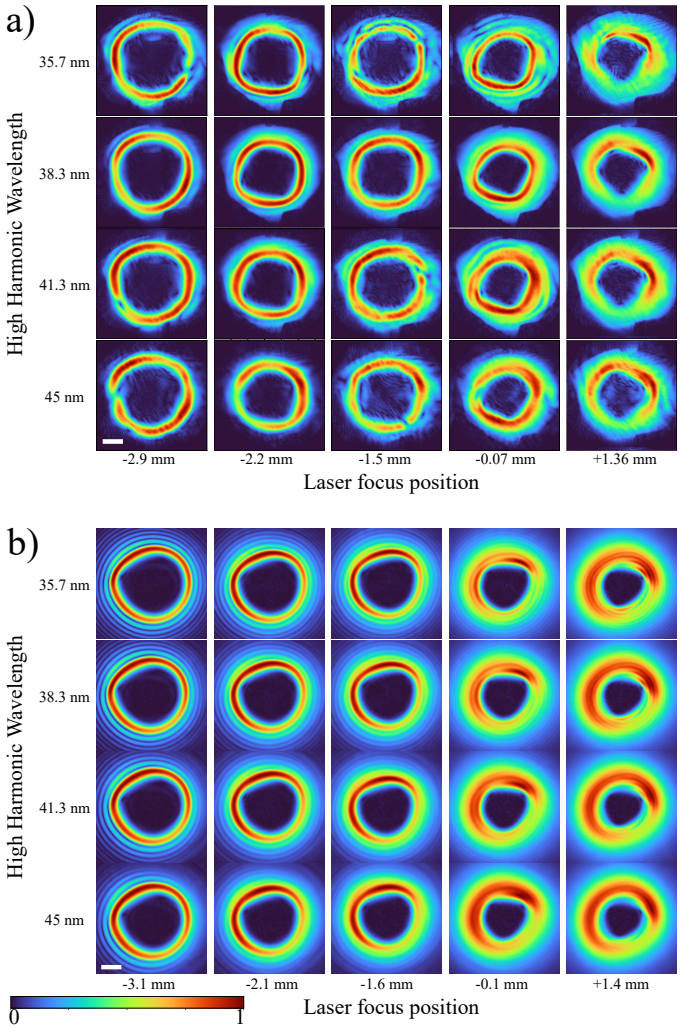

Figure 4.8: Reconstructed beam amplitudes for four harmonics ranging from 35.7 nm (29^{th} harmonic) to 45 nm (23^{rd} harmonic) at the curved multilayer mirror plane for various laser focus positions with respect to the gas medium. Positive (negative) laser focus positions means that the laser focus is downstream (upstream) of the gas jet position. a) Reconstructed beams from experimental data, b) modelled beams. Scale bars are equal to 3 mm.

repeat the simulation of generation and numerical propagation of HHG beams for a drive beam with perfect circular symmetry and without aberrations.

In order to be consistent with other parameters, such as drive beam size at the (varying) generation plane, we simulate the drive beam in the same way as we did to generate the modelled results of Figs. 4.2, 4.8 and 4.9. We started with the reconstructed IR Gaussian wavefront from the fundamental ptychography recon-

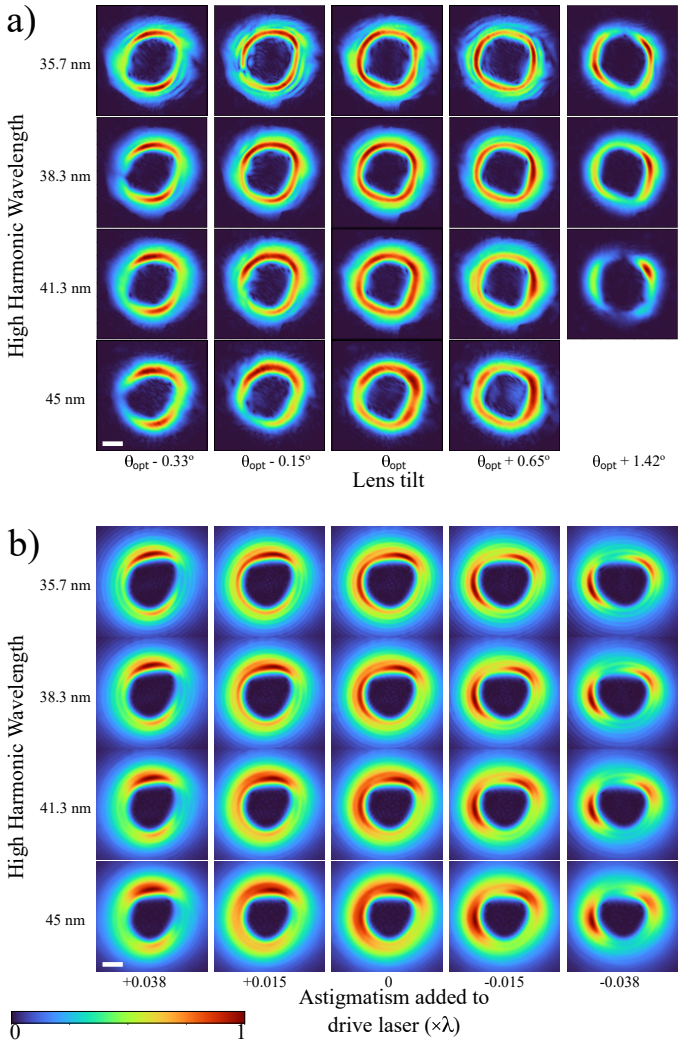

Figure 4.9: Reconstructed beam amplitudes at curved multilayer mirror plane for varying tilts of the focusing lens of the drive laser. a) Reconstructed beams from experimental data, b) modelled beams. In a) the reconstructed beam at 45 nm wavelength and $\theta_{opt} + 1.42°$ tilt angle is missing because the reconstruction was not trustworthy due to low signal within the beam profile. Scale bars are equal to 3 mm.

struction, which we propagated numerically to the lens plane. At the lens plane we fitted a circularly symmetric Gaussian profile to the beam intensity, removed the existing phase and added manually a quadratic phase that corresponds to an ideal lens with focal length equal to 30 cm.

The results of the far-field HHG beam amplitudes for varying drive laser focus positions is shown in Fig. 4.10 for the 27^{th} harmonic (38.3 nm) as an example.

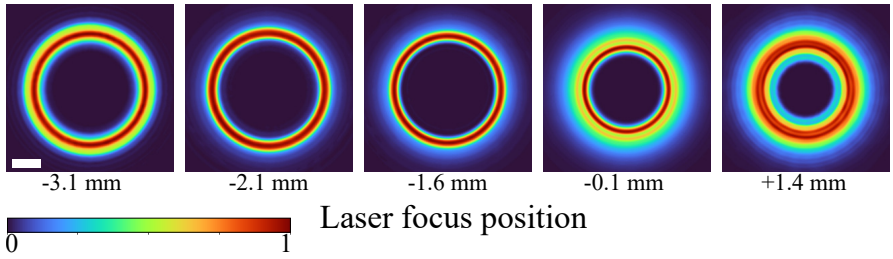

Figure 4.10: Modelled beam amplitudes for the 27$^{\text{th}}$ harmonic (38.3 nm) at the curved multilayer mirror plane for various laser focus positions with respect to the gas medium. The drive beam is simulated with an ideal circularly symmetric intensity profile and a non-aberrated phase. Here we consider only short trajectory contributions. Scale bar is equal to 3 mm.

The intensity profiles for different harmonics in the examined range of harmonic orders (23-29) are slightly different but exhibit the same trend. We observe a single ring in the far field, with a varying thickness for different laser focus positions. These results are in good agreement with other reported theoretical results [94]. Therefore, we can conclude that the appearance of the multiple rings is due to the specific drive beam properties.

4.5.3 Simulated long trajectory contributions

To complement the analysis of the modelled high harmonic wavefronts, we present the simulated wavefronts that would correspond to the long trajectory contributions. As mentioned in the main text, we use the single atom response (SAR)[91, 92] model that gives the following expressions for the amplitude A and the phase Φ of each high harmonic q in the plateau region for the long trajectories:

$$\begin{aligned} A_q(x,y) &= A_f(x,y)^p \\ \Phi_q(x,y) &= q\phi(x,y) + \Phi_{l,q}(x,y) \\ \Phi_{l,q}(x,y) &= \alpha_l I(x,y) + \frac{\gamma_l}{I(x,y)}(q\omega - \Omega_p)^2 \ + \ const. \end{aligned}$$

The values of the constant factors are adjusted from [92] for a drive laser wavelength equal to 1030 nm, $\alpha_l = -5.08 \times 10^{-13}$ W^{-1}cm^2, $\gamma_l = -0.685 \times 10^{-18}$ s^{2}Wcm^{-2}. The drive beam parameters and identical to the ones used in the main text to calculate the short trajectory contributions (pulse energy $E \approx$1.3 mJ, and pulse duration $\Delta t = 45$ fs). Example for the 27$^{\text{th}}$ harmonic (38.3 nm) of the complex-valued beam profile at the gas jet plane for varying drive laser focus position is shown at Fig. 4.11. All harmonics in the examined range of harmonic orders 23-29 have a similar behavior. We observe a very strong quadratic behaviour for the phase in radial direction, which we have verified that is caused by the term $\alpha_l I(x,y)$. Upon propagation to the far field, this beam

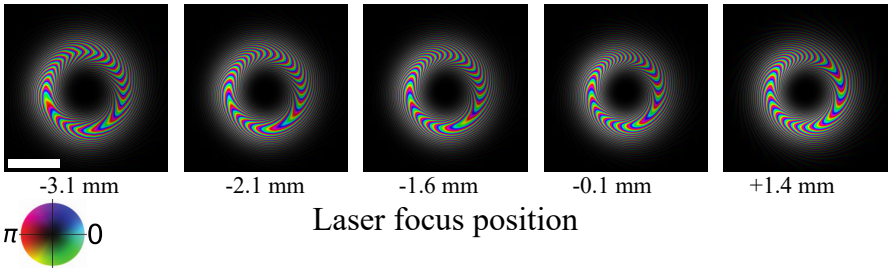

Figure 4.11: Modelled long trajectory contributions of the 27$^{\text{th}}$ harmonic (38.3 nm) at the generation plane, for various laser focus positions with respect to the gas medium. Scale bar is equal to 50 µm.

does not remain well-defined and we cannot detect it.

4.5.4 Propagation of HHG OAM beams

Diagonal cross-sections of propagation plots

Ptychographic reconstruction of the complex fields of individual harmonics enables numerical propagation of the beams. In the main text we have shown horizontal and vertical cross-sections of the numerical propagation for the reconstructed and astigmatism-corrected HHG wavefronts. However, since the studied beams exhibit strong asymmetries azimuthally, we also show diagonal cuts for a more complete view of the beam propagation behavior in Fig. 4.12.

Effect of dipole phase on rim thickness

From overlapping propagation plots of HHG beams for different laser focus positions, we observed in the main text that there is a local peak in the rim thickness of which the position varies with respect to the focal plane. From the simulations we could confirm that this peak is located at the generation plane. Figure 4.13a) shows the effect of the dipole phase on the rim for the 27$^{\text{th}}$ harmonic (38.3 nm), where we observe a subtle, but observable effect of the dipole phase. Specifically, we notice that the falling edge of that local maximum in the rim shifts slightly downstream. This finding supports our explanation in the main text that the dipole phase, which has a profile inversely proportional to the drive laser intensity, creates local divergent wavefronts that lead to expansion of the rim. This tendency to expand is eventually counteracted by an opposite effect caused by the fact that the present LG modes in the beam move out of phase upon propagation. The results shown in Fig. 4.13a), as well as in the main text, are averaged plots over all azimuthal angles. Due to asymmetries in the HHG OAM beam profiles, both diameter and rim can vary for different azimuthal angles. For completeness, in Figs. 4.13b) and 4.13c) we show standard deviation plots for the diameter and rim respectively, of the results of Fig. 4.13a). We observe that the standard deviation is always considerable smaller than the mean value for all datasets and

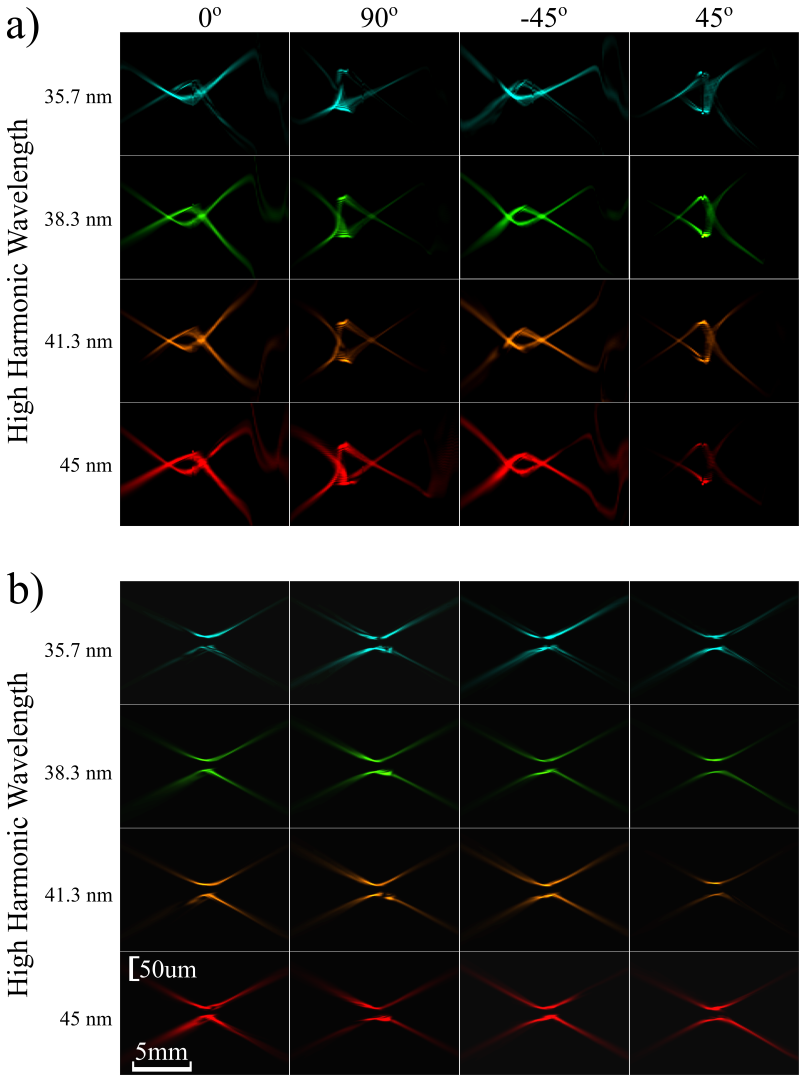

Figure 4.12: Propagation of harmonic beams along the focal plane after refocusing. a,b) Cross sections along different cuts (horizontal, vertical and diagonal) for a) the reconstructed wavefronts from the PWFS measurement, b) the astigmatism-corrected beams at the curved multilayer mirror plane which are subsequently forward propagated around the focus.

propagation positions.

Propagation of astigmatic HHG OAM beams

In the main text we show overlapped in-plane plots of HHG OAM beams for different drive laser astigmatism levels. In Fig. 4.14 we separate the three color

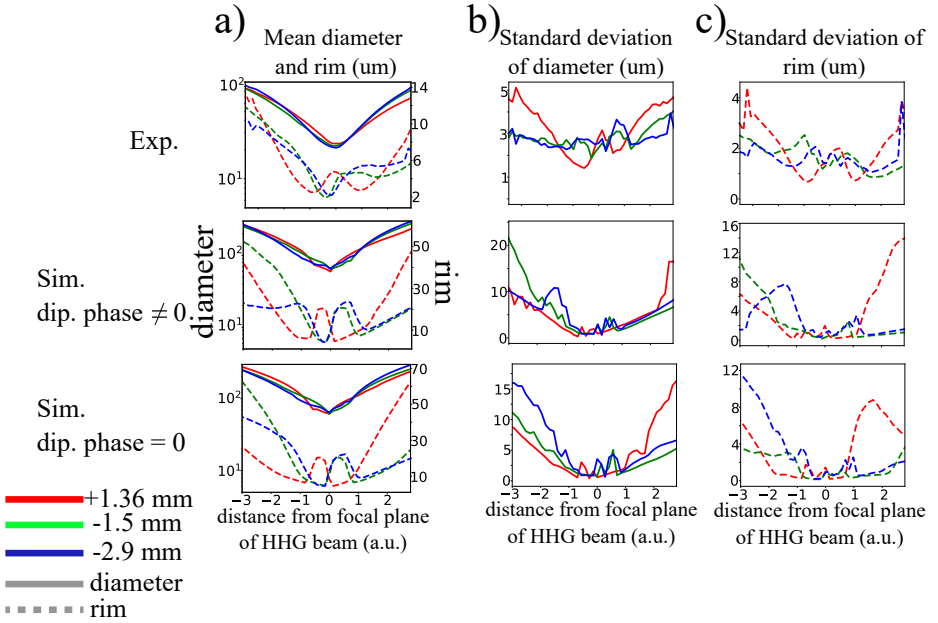

Figure 4.13: Experimental and model results for the variation of diameter and rim for the 27$^{\text{th}}$ harmonic (38.3 nm), with comparison of the model with and without the dipole phase contribution.

channels, so that it is clear how the 27$^{\text{th}}$ harmonic (38.3 nm) beam looks for different laser astigmatism conditions, as it propagates through the focus.

4.5.5 Calculation of OAM modal content

The OAM modal content of an OAM beam can be determined either by a Laguerre-Gaussian (LG) decomposition of the beam or by performing 1D azimuthal Fourier Transform (FT) along the beam. In the analysis presented in the main text, we used LG decomposition as the experimental beams were not perfectly circular and an azimuthal FT would potentially not be accurate. However, for a circular beam, which occurred when we minimized the drive laser astigmatism, the results from LG decomposition and FT are quite similar, as shown in Fig. 4.15. We have performed azimuthal FT along 5 rings with varying radius, in a range where the beam intensity is significant and present the results in Fig. 4.15c). The results are in very close agreement with the LG decomposition results shown in Fig. 4.6a) for the same beam, which corresponds to laser focus position equal to -1.5 mm.

Furthermore, in Fig. 4.15b) we show the complete LG decomposition of the same beam, with coefficients for all radial and azimuthal modes. We observe that there is a dominant LG mode with zero radial nodes, but higher radial modes are also present. Assuming the LG coefficients are preserved over their propagation from the gas jet to the far field, the presence of many radial modes

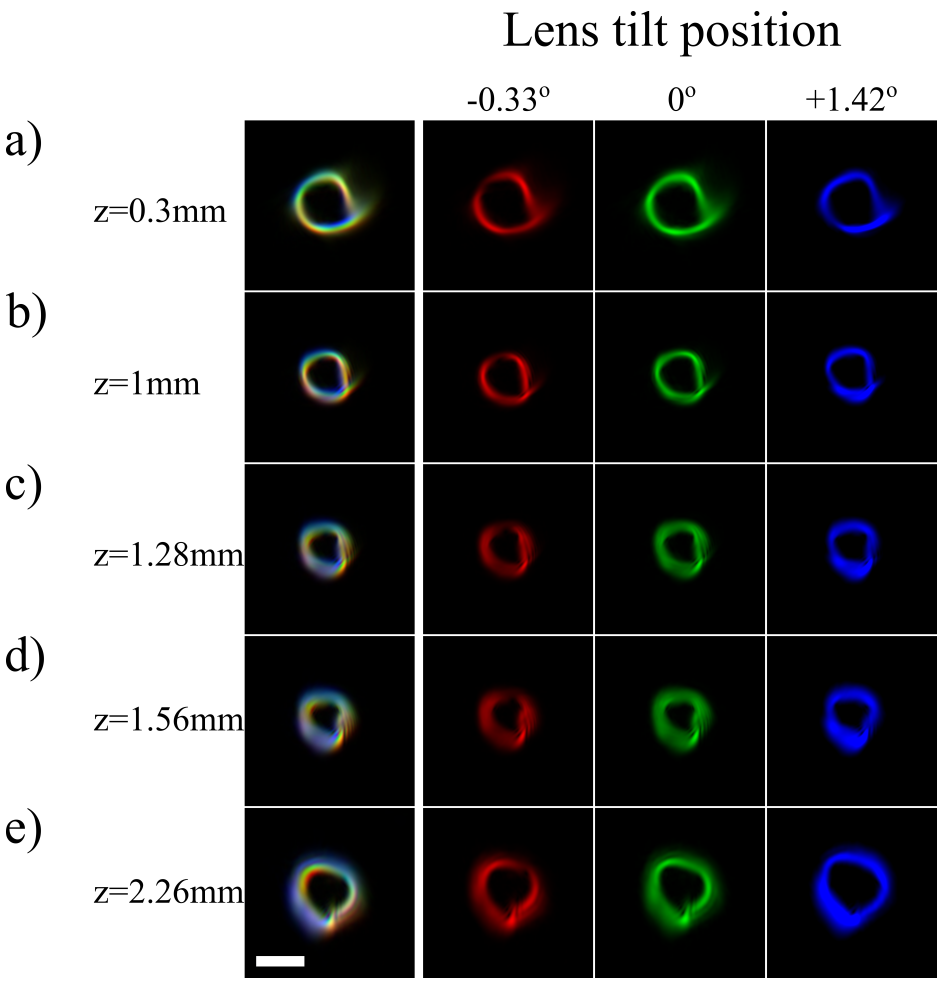

Figure 4.14: Decomposition of the overlapped beam plots of Fig. 4.5c-g) of the main text into separate color channels. Note that the $\theta_{opt} + 1.42°$ results are shown in a reduced dynamic range for better visibility. The scale bar is equal to 30 µm.

with a dominant zeroth order radial mode explains why the rim exhibits the behavior shown in Fig. 4.13a).

4.5.6 Synthesis of attosecond pulse trains from ptychographic reconstructions

In this analysis we are interested in studying how the generation conditions affect the generated attosecond pulse, thus we remove all known effects of the multilayer mirrors, namely the shaping of the spectral weights and the astigmatism induced

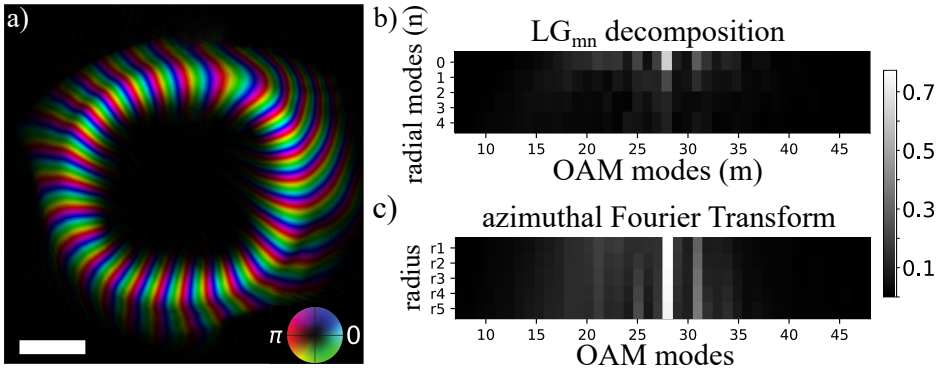

Figure 4.15: Orbital angular momemtum (OAM) modal content of the 27$^{\text{th}}$ harmonic (38.3 nm) for drive laser focus position equal to -1.5 mm. a) beam amplitude and phase, b) complete c_{mn} LG modal decomposition into azimuthal and radial modes, c) calculated OAM content via azimuthal Fourier Transform on varying radii. The scale bar in a) is equal to 3 mm.

by the spherical multilayer mirror.

The ptychographic reconstruction algorithm treats the wavefronts as independent incoherent modes and is insensitive to the relative phase between the harmonic beams. Therefore, we can only assume phase coherence between the harmonics, and numerically fix the phase of all harmonic beams at a manually selected bright part of the polychromatic beam at time $t = 0$. This assumption ensures that all harmonics constructively interfere to create one of the two helices. The resulting spatial and temporal intensity profiles are shown for different laser focus positions in Fig. 4.16a), and for different amounts of astigmatism in Fig. 4.16b). We also show examples of the temporal evolution of the attosecond pulse train over an extended period of 6 fs for laser focus position equal to +1.36 mm (Fig. 4.16a)) and drive laser astigmatism from lens tilt equal to $\theta_{opt} + 0.65°$ (Fig. 4.16b)). Here we have assumed that we have a periodic signal with a slight amplitude modulation that follows the Gaussian temporal shape of the drive laser. From the comparisons between different generation conditions, we observe that the generation conditions only have limited effect on the temporal shape of the attosecond pulse train, although the broadened OAM modal content of the harmonic wavefronts lead to pre- and post-pulses that are sensitive to the laser focus position.

However, the spatial properties of the pulse train are more significantly affected by the generation conditions. From the spatial properties of the pulse at $t = 0$ we can distinguish the manually fixed bright spot, which is located either at the top right part or at the bottom right part of the beams. Interestingly, at the opposite side of the ring, the second helix appears weaker, which indicates that matching the phases for the one helix does not ensure perfectly constructive interference at the second helix in the presence of aberrations in the harmonic

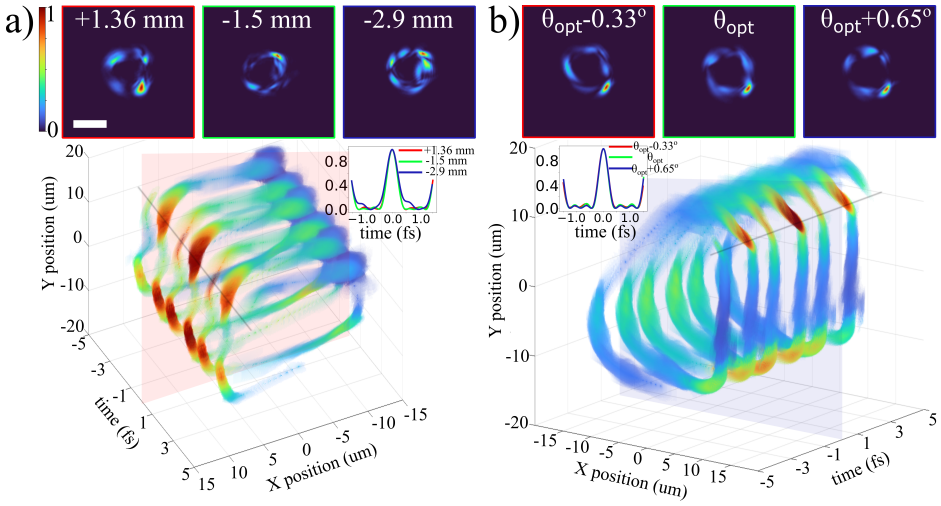

Figure 4.16: Comparison of attosecond pulse trains for a) different drive laser focus positions, and b) different drive laser astigmatism levels, expressed as lens tilt positions of the focusing lens to the gas jet. Top: spatial intensity profiles at time $t = 0$, bottom: Temporal evolution of the high-harmonic signal for a) laser focus position +1.36 mm and b) lens tilt position $\theta_{opt} + 0.65°$. The colored planes indicate the $t = 0$ plane. The insets show the comparison of the temporal evolution at a specific point in space with high intensity at $t = 0$, as indicated with the solid gray line in the 3D plots. Scale bar is shared among all spatial intensity profile figures and is equal to 20 µm.

wavefronts. Instead, there are secondary bright parts spread at various azimuthal angles, which appear as pre- and post-pulses in the temporal plots of Fig. 4.16. Finally, in Fig. 4.16b) we notice that the astigmatism of the drive laser leads to either clockwise or counterclockwise shift of the second helix compared to the stigmatic case, depending on the positive or negative tilt angle of the focusing lens. These results give an indication of the possible spatiotemporal structure of the attosecond pulse train that can be synthesized with the experimentally observed harmonic fields.

Chapter 5

Illumination diversity in multi-wavelength extreme ultraviolet ptychography

With the development of high harmonic generation (HHG), lensless extreme-ultraviolet (XUV) imaging at nanoscale resolution has become possible with table-top systems. Specifically, ptychographic phase retrieval using monochromatic XUV illumination exhibits extraordinary robustness and accuracy to computationally reconstruct both the object and the beam profile. In ptychography, using structured illumination has been shown to improve reconstruction robustness and image resolution by enhancing high-spatial-frequency diffraction. However, broadband imaging has remained challenging, as the required multi-wavelength algorithms become increasingly demanding. One major aspect is the ability to separate the available information into different physically meaningful states, such as different spectral components. Here we show that introducing spatial diversity between spectral components of a HHG beam can significantly improve the reconstruction quality in multi-wavelength XUV ptychography. We quantify the diversity in the polychromatic illumination by analyzing the diffraction patterns using established geometry- and information theory-based dissimilarity metrics. We experimentally verify the major influence of diversity by comparing ptychography measurements using HHG beams with Gaussian and binary structured profiles, as well as with beams carrying wavelength-dependent orbital angular momentum. Our results demonstrate how structured illumination separates the spectral information in a single diffraction pattern while providing maximized added information with every new scan position. We anticipate our work to be a starting point for high-fidelity polychromatic imaging of next-generation nanostructured devices at XUV and soft-X-ray wavelengths.

The content of this chapter has been published as: Antonios Pelekanidis, Fengling Zhang, Matthias Gouder, Jacob Seifert, Mengqi Du, Kjeld S. E. Eikema, and Stefan Witte, *Illumination diversity in multiwavelength extreme ultraviolet ptychography,* Photonics Research **12**(12), 2757–2771 (2024).

5.1 Introduction

Advances in diffraction-based imaging technology [195, 196] have pushed the achievable resolution well beyond the capabilities of conventional microscopes. In particular, coherent diffraction lensless imaging (CDI) in the extreme ultraviolet (XUV) regime has become an active research area. The short wavelengths in the XUV region give a better diffraction-limited resolution [3] compared to visible or infrared light, while it is still possible to generate coherent light at these wavelengths with tabletop sources via high harmonic generation (HHG) from a near-infrared (NIR) driving laser [81, 131, 183–185, 197]. One specific technique for CDI is ptychography, in which the object is translated laterally to the source and a series of correlated diffraction patterns are captured [23, 24]. The reconstruction algorithm can then computationally retrieve the missing phase of the measured diffraction patterns and reconstruct complex-valued expressions for the object and the illumination source. Ptychography has been investigated extensively in the XUV [31, 32, 34, 35, 38–40, 63, 111, 198, 199] and X-ray ranges [28, 62, 200, 201], and has been proven to be a robust method to image both the object and the illumination, called probe hereafter, in principle without the necessity for support constraints or other prior knowledge.

In HHG a number of high harmonics of the driving laser field are generated. This large bandwidth in principle allows for broadband imaging, which can reveal element-specific information of a sample due to the material-specific transmission windows in the XUV spectral range [202]. However, the polychromatic beam lacks the necessary longitudinal coherence for diffraction-based methods such as ptychography. In many recent works, coherence is achieved by spectrally filtering the HHG beam and selecting a single harmonic [35, 38, 39, 198], which is effective for single-wavelength object reconstruction, but removes the ability for spectroscopic imaging. Retrieving full spectral information from broadband diffraction can be achieved through two-pulse Fourier-transform methods [18, 21], but the need for two coherent sources and the required temporal scanning make this concept challenging to combine with ptychography. A more efficient and flexible approach is multi-wavelength ptychography [31, 34, 44, 63, 201, 203, 204]. In multi-wavelength ptychography, the probe and object are typically modeled as a set of incoherent modes, similar to the mixed states approach for partially coherent beams [43], with each mode corresponding to a different wavelength. However, due to the presence and the necessity to reconstruct complex-valued expressions for all probe and object modes, the demands on the reconstruction algorithm become increasingly challenging.

Experience from earlier works has shown that structured illumination improves the reconstruction quality and algorithm convergence [35, 50, 70–72, 76, 205, 206]. A structured beam provides higher illumination NA and reduces the dynamic range of the diffraction pattern, which leads to more efficient use of the full chip of the camera. For ptychography with HHG beams, structure can be accomplished either by structuring directly the XUV beam with the use of a mask [35, 62, 72] or a phase-shifting diffuser in the beamline [75] or indirectly by structuring the driving laser beam, which transfers amplitude and phase properties to the high

harmonics [91, 173]. A specific example of such phase transfer is the upconversion of beams carrying orbital angular momentum (OAM) [95, 167, 169, 171, 172, 177–181], for which it was shown that the q^{th} harmonic of a driving beam with OAM l_1 will have an OAM of $l_q \approx q \cdot l_1$, with the exact OAM depending on the fundamental beam properties [167, 179]. Wang *et al.* [69] showed that ptychography on periodic structures can be improved significantly by using an XUV beam with nonzero OAM, as its large intrinsic divergence leads to overlapping diffraction orders in the far field.

In addition to the amount of structure in individual diffraction patterns, a key aspect of ptychography is the diversity between scan positions. Similarly, multimode ptychography can be expected to benefit in situations where the diffraction resulting from different modes is clearly distinct. Especially when such modes are well-defined physical states, such as different wavelengths, it should be possible to engineer the illumination such that the resulting diffraction data can be more accurately processed by multimode ptychography algorithms.

In this paper we investigate and experimentally demonstrate the improvement in ptychographic multi-wavelength reconstructions with directly and indirectly structured HHG probe beams compared to smooth Gaussian beams. To systematically explore the suitability of a probe for a given object and experimental ptychographic setup, we introduce the concept of diversity in the diffraction patterns and use dissimilarity metrics [207] to characterize our probes. We observe a strong correlation between these diversity metrics and the achieved image reconstruction quality. Based on these observations, we conclude that analyzing and optimizing diversity between wavelengths (or other modes) is an important aspect in the design of any multimode ptychography experiment.

5.2 Diversity considerations

In multi-wavelength ptychography the reconstruction algorithms are usually based on ptychographical information multiplexing (PIM) [44], which models measured polychromatic diffraction data as an incoherent sum of individual monochromatic diffraction patterns. For objects with grating-like structures, probe modes corresponding to different wavelengths have distinct diffraction angles and illuminate different areas of the detector [63, 151], which facilitates the reconstruction algorithm to identify the monochromatic components of the polychromatic diffraction pattern. However, for general imaging purposes, objects with arbitrary features do not guarantee spectral diversity. This creates a challenge for the reconstruction algorithm to reliably converge and accurately reconstruct all probe and object modes. Here we explore the influence of illumination diversity on successful ptychographic reconstructions.

The concept of diversity enhancement is illustrated in Fig. 5.1. We consider a binary object illuminated by an XUV beam consisting of the 27^{th} and the 29^{th} harmonic of a 1030 nm wavelength drive laser, with either low or high diversity. The two harmonic beams are assumed to have equal photon flux for both diversity cases. As a low-diversity beam we assume a flat wavefront with top-hat

intensity distribution for both wavelengths (Fig. 5.1a)), while for high diversity we consider a beam with similar intensity profiles but having an OAM phase proportional to the harmonic order (Fig. 5.1b)). We model the propagation of the two-color beams from the sample plane to a camera plane that is placed in the far field. Figures 5.1c) and 5.1d) show images of the difference between the two wavelength components in the far-field diffraction patterns for the flat and OAM beam respectively in a saturated dynamic range in order to highlight the differences. It is clear that the diversity introduced by the wavelength-dependent OAM phase leads to strongly enhanced differences in diffraction between the modes.

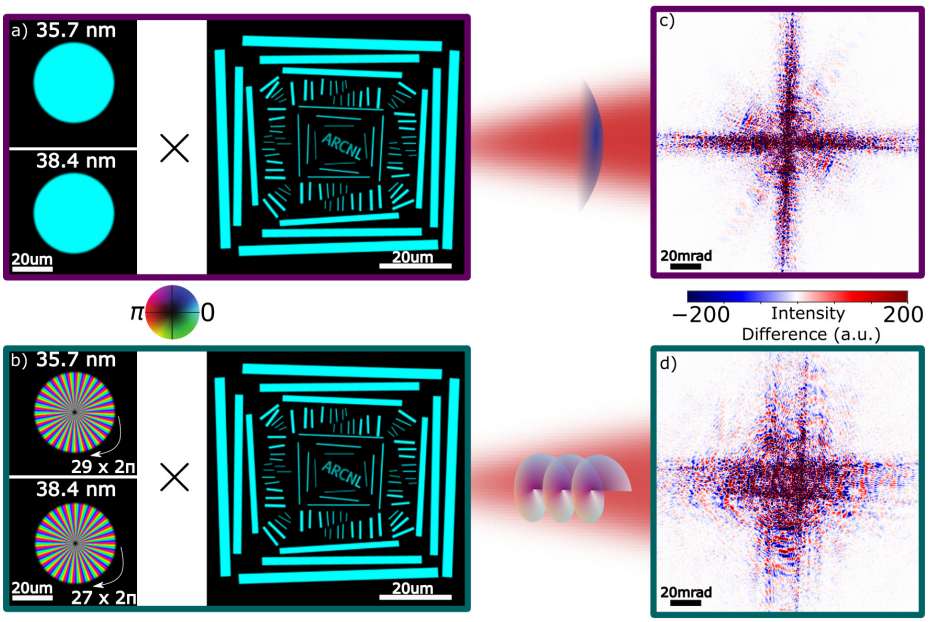

Figure 5.1: Spectral diversity in diffraction. (a, b) A binary object is illuminated by a beam containing the 27^{th} and 29^{th} harmonics (at 38.4 nm and 35.7 nm wavelength), either with (a) a flat intensity and phase or (b) with order-dependent OAM. (c, d) Difference of the monochromatic diffraction patterns between the two wavelengths ($I_{35.7nm} - I_{38.4nm}$) for (c) flat and (d) OAM beam illumination. The dynamic range of the camera is set to ≈20-bit and 15-bit for the flat beam and OAM beam respectively such that the number of photons in the incoherent sum of the monochromatic diffraction patterns is equal to 2.27×10^8 photons in both cases.

The diversity in diffraction patterns can be quantified using various dissimilarity metrics [207], such as the *L1* norm, the *L2* norm, the *cosine* metric and the *Jensen-Shannon divergence* (JSD). The former three metrics treat the $N \times N$-

sized diffraction patterns as one-dimensional vectors with size equal to N^2 and calculate the distance or angle between the vectors. JSD is a metric borrowed from information theory that compares two or more probability density functions (PDFs). To evaluate the JSD we treat each diffraction pattern as the PDF of the diffracted beam over all detector pixels. The mathematical expressions for these metrics are:

$$D_{p-norm} = \frac{\Big(\sum_{x,y} |I_1(x,y) - I_2(x,y)|^p\Big)^{1/p}}{\max_{k\in[1,2,\dots,K]}\Big(\sum_{x,y}\big(I_k(x,y)\big)^p\Big)^{1/p}} \tag{5.1}$$

$$D_{cosine} = 1 - \frac{\sum_{x,y}\big(I_1(x,y)\cdot I_2(x,y)\big)}{\big(\sum_{x,y} I_1(x,y)^2\big)^{\frac{1}{2}}\big(\sum_{x,y} I_2(x,y)^2\big)^{\frac{1}{2}}} \tag{5.2}$$

$$D_{JSD} = S\Big(\sum_{j=1}^{2}\frac{1}{2}I_j\Big) - \sum_{j=1}^{2}\frac{1}{2}S(I_j) \tag{5.3}$$

where $p = 1$ or $p = 2$ for calculating the diversity according to L1 or L2 norm respectively, K is the number of scan positions, I is the diffraction pattern for a scan position and $S\big(I(x,y)\big) = \sum_{x,y} I(x,y)\log I(x,y)$, with $\log\alpha$ the natural logarithm of α, is the spatial entropy functional as defined in [34]. The cosine metric and JSD are bounded metrics with $0 \leq D_{cosine} \leq 1$ and $0 \leq D_{JSD} \leq \log 2$. The L1 norm and L2 norm are instead unbounded metrics and the absolute values of distances give practically no information about the similarity of two diffraction patterns, as they depend on the dynamic range that is assumed for the calculation of the norms. For this reason, we use a relative L1 norm and L2 norm metric, which are normalized with respect to the largest magnitude in the diffraction pattern series. The relative norms, albeit still unbounded, give more insight about the similarity of two diffraction patterns. Using these metrics, we can compare pairs of monochromatic diffraction patterns at a single scan position and calculate the *spectral diversity*. Similarly, we can compare pairs of polychromatic diffraction patterns that correspond to two adjacent scan positions in the ptychographic measurement and compute their *scanning diversity*.

Scanning diversity, where each additional scan position contributes new information to the ptychographic reconstruction algorithm, is highly beneficial. This is because the robustness of ptychography relies on the aggregated information from diffraction patterns recorded at partially overlapping areas of the object. With HHG beams it is challenging to isolate the effects of spectral and scanning diversity in an experiment, and to tune the amount of diversity in a continuous way. To get more insight in the diversity provided by structuring the HHG beam, and the subsequent improvement in the ptychographic reconstructions, we performed a series of numerical simulations. In these simulations we consider an object that is illuminated by a monochromatic Gaussian-shaped probe beam with increasing divergence, keeping all other relevant parameters constant (beam size: 30.5 µm; scanning pattern: concentric, 200 scan positions; overlap: 87%; photon flux of probe: 8.4×10^8 photons; distance between object and detector: 105 mm;

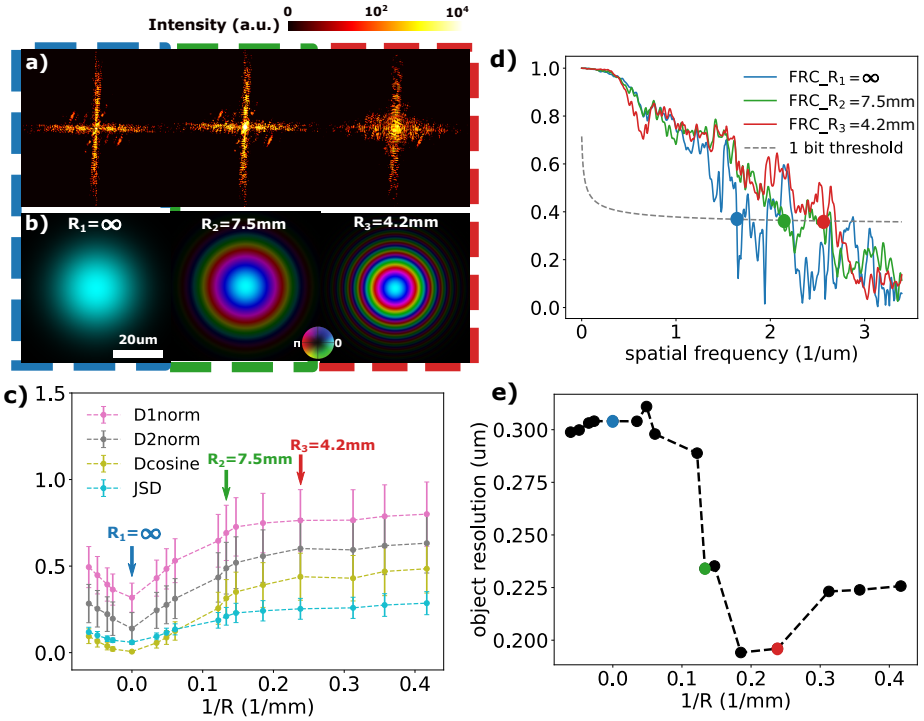

Figure 5.2: Scanning diversity and reconstruction quality of simulated datasets. a) Logarithmic scale diffraction patterns are shown for beams with radii of curvature $R = \infty$, $R = 7.5\,\mathrm{mm}$, and $R = 4.2\,\mathrm{mm}$, all illuminating the center of the object at scan position 0. b) Three monochromatic probes at 38.25 nm wavelength with increasing quadratic phase and identical Gaussian intensity profile (30.5 µm $1/e^2$ diameter). c) Diversity metrics $D_{1\,norm}$, $D_{2\,norm}$, cosine and JSD by comparing diffraction patterns between adjacent scan positions for a scan grid with the first 20 scan points, as a function of the quadratic phase of the probe. d) The example FRC by comparing independent reconstructions within the datasets of three monochromatic probes. The intersection of FRC curves and one-bit threshold line determines the object resolution. e) Reconstruction quality calculated from the FRC as a function of the quadratic phase of the probe. The colored dots are extracted from d).

probe wavelength: 38.25 nm; noise statistics: mixture of Poisson and Gaussian $\mathcal{N}(0, 50)$.) Probe divergence can be considered as a simple, continuously tunable version of spatial beam structure, resulting in similar diversity variation as observed for the binary masks and OAM beams that we study experimentally (see below). Since the actual object is known, the quality of ptychographic reconstruction can be calculated with the Fourier ring correlation (FRC) for the object [208]. The object used in simulation is shown in Fig. 5.1. The examples of probes with increasing quadratic phase and the corresponding diffraction patterns are given in Figs. 5.2a-b).

The magnitudes of the various diversity metrics as a function of beam diver-

gence are shown in Fig. 5.2c). The diversity is calculated by comparing diffraction patterns from adjacent scan positions. We observe that all diversity metrics exhibit a similar trend with slight variations: the lowest diversity occurs when the object is illuminated by a flat wavefront, while diversity stabilizes after a certain degree of curvature is added to the beam phase. For each probe curvature, we performed independent ptychography reconstructions, with the achieved object resolution determined using FRC. As examples, Fig. 5.2d) shows the FRC results of three beams with increasing quadratic phase, demonstrating that the achieved resolution improves as beam divergence increases. Figure. 5.2e) summarizes the achieved object resolution. As beam divergence increases, diversity between the diffraction patterns also improves. Consequently, the aggregated information from diffraction patterns recorded during each scan position increased. Therefore, we attribute the better reconstructions obtained with more divergent beams to the higher scanning diversity they provide.

5.3 Results

5.3.1 Experiment design

To test the use of diversity metrics in ptychography, we designed a series of experiments in which we perform multi-wavelength ptychography in the extreme-ultraviolet wavelength range, while introducing varying degrees of diversity both between the different wavelength components and scan positions. We use HHG as the illumination source, as it naturally provides coherent XUV radiation at multiple wavelengths in parallel. The concept extends to other broadband XUV sources such as pink beam synchrotrons and free-electron lasers. To control the amount of diversity, we use two ways to structure the illumination beams, as schematically indicated in Fig. 5.3. The first approach is the introduction of a binary mask in the HHG beam just before the imaging target. This mask leads to a finely structured beam at the object location, thus increasing the scanning diversity. In addition, the diffraction from the mask leads to increased spectral diversity at the object location as well. The second approach is to structure the HHG radiation by shaping the fundamental laser beam. Here we use the property of the HHG process that OAM is upconverted in an order-dependent way, which naturally leads to a large spectral diversity at the object location while maintaining efficient HHG. The rapid angular phase profiles of these OAM beams also result in a high scanning diversity. With these different HHG beams, we perform ptychography scans on a resolution test chart. The resulting data is reconstructed using our PIE-based algorithm [110] and analyzed to determine the link between diversity and image reconstruction quality.

5.3.2 Experimental setup

The experimental setup is shown in Fig. 5.3a). A NIR laser is focused in an argon gas jet to generate high harmonics. Detailed information about the HHG source is given in Appendix 5.6.1. Before the focusing lens we can insert a spiral phase

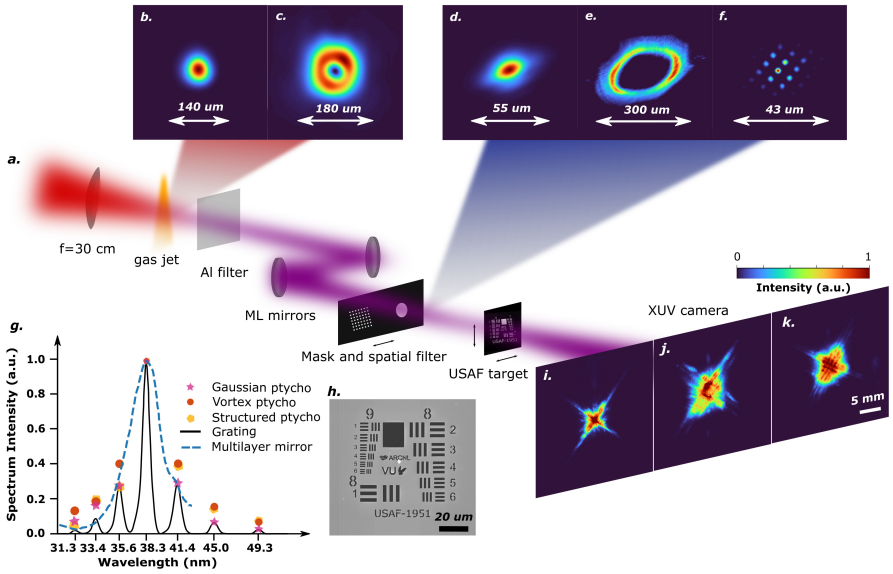

Figure 5.3: Experimental setup. (a) The driving NIR laser is focused by a $f = 300\,\text{mm}$ focal length lens into an argon gas jet. An Al filter blocks the fundamental and the high harmonics are refocused by a pair of broadband multilayer mirrors onto the sample. A CCD camera is placed approximately 10 cm from the focal plane. (b, c) Intensity profile of the driving laser at the gas jet plane for generating (b) Gaussian and (c) OAM XUV beams. (d-f) Polychromatic beam intensities for (d) Gaussian, (e) vortex, and (f) structured beam, computed upstream from the sample plane at distances 8.1 mm, 6 mm, and 1.625 mm (mask plane), respectively. (g) Measured and reconstructed spectrum of the XUV radiation after the mirrors, plotted along with the reflectivity curve of the XUV mirrors. (h) Scanning electron microscope image of the imaging target. (i-k) Polychromatic diffraction patterns from illumination of the central part of the object with (i) Gaussian, (j) vortex, (k) structured beam.

plate (Vortex Photonics V-1064-20-1 [209]) in the beamline to generate a vortex fundamental beam with OAM equal to 1.

Behind the gas jet, a 200 nm aluminum membrane filters out the fundamental beam and the high harmonics are directed and focused by a pair of plane and curved (ROC=500 mm) multilayer mirrors onto the sample. A secondary sample stage is placed at 1.62 mm distance in front of the sample plane, allowing us to place a binary beam-structuring mask or a circular aperture with 50 µm diameter. The binary mask consists of a set of 2 µm holes oriented in a slightly distorted periodic grid separated by an average distance of 5 µm. The 50 µm aperture acts as a spatial filter for the XUV Gaussian beam and minimizes the leakage of the fundamental beam on the camera, while no mask or aperture is used for the vortex beam measurements. As the Gaussian beam at the focus is smaller compared to

the structured beams, the measurement with the Gaussian probe is performed with the sample placed 4 mm behind the focus, where the beam has expanded to a comparable size with respect to the focused vortex or mask-structured beam.

The imaging object is a home-built USAF-1951 resolution target with printed logos of VU and ARCNL at the center of the target (Fig. 5.3h)). It is oriented in a 45-degree configuration so that the diffraction of the bars is along the diagonal of the camera, where the detection NA is maximized. A typical multi-spectral HHG diffraction pattern corresponding to illumination of the central area of the sample is shown in Figs. 5.3i-k) for the three considered beams (Gaussian, vortex, structured), assuming equal photon budgets for the three beams. From the individual polychromatic diffraction patterns it can be seen that the vortex beam leads to the highest NA data, as the diffraction pattern has spread to higher angles on the detector. However, we expect that the overall reconstruction quality is not merely a function of the effective NA, but it will be described more completely by the spectral and scanning diversity metrics.

Figure 5.3g) shows the XUV spectrum, measured from the diffraction of the HHG beam through a transmission grating with 500 nm pitch (solid line) and compared with the spectral weights of the reconstructed probes shown in the next section. The Gaussian-shaped envelope of the spectrum has been formed by the efficiency of the XUV mirrors (dashed line in Fig. 5.3g)) that favour the reflection of the 27^{th} harmonic (38.3 nm), while harmonics 25 and 29 have about three times lower first-order diffraction signal on the camera, and harmonics 23 and 31 have about ten percent of the signal strength of the brightest harmonic.

5.3.3 Ptychographic imaging with different probes

In order to have a fair comparison for the reconstruction quality of ptychographic imaging experiments with different beam types, it is important that other experimental settings, such as sample to camera distance, illumination overlap between adjacent scan positions and probe energy are identical. However, in practice the distance between object and camera is slightly different for measurements with different beam types, and varies between 104.8 mm and 108 mm to achieve a desired beam size at the sample plane. The variation in the distance leads to a 3% variation of the achievable diffraction-limited resolution. Moreover, in order to maximize the captured information from each ptychography scan, we aimed for the utilization of the full dynamic range of the camera via adjusting exposure times and preamplification gain of the camera. This strategy inevitably leads to unequal photon budget of the diffraction patterns for different beam types, as smooth beams more readily saturate the zeroth order diffraction at the center of the camera. A possible solution to this issue would be high dynamic range exposures [30, 31, 69, 199] during the measurement of the Gaussian beam, which however significantly increases measurement time, and increases long-term drift and stability requirements.

The ptychographic datasets for the Gaussian and vortex beams consist of 218 scan positions in a concentric scan grid with 6 µm step size and 104 µm field of view. For the structured beam we used a scan grid with smaller step size (2.45 µm)

and field of view (44 µm) due to an underestimation of the probe size. Due to the irregular intensity profile of the non-smooth beam types, characterization of the overlap with a linear overlap factor $1 - \frac{\text{step size}}{\text{beam diameter}}$ [41] is not accurate. Therefore, we have defined the overlap as the two-dimensional average cross-correlation of a binarized version of the polychromatic beam with a translated version of itself to an adjacent scan position. According to this definition, the overlap is equal to 74% with a standard deviation of 5.8% for the Gaussian beam, 68% with a standard deviation of 8.3% for the vortex beam and 88.6% with a standard deviation 10% for the structured beam.

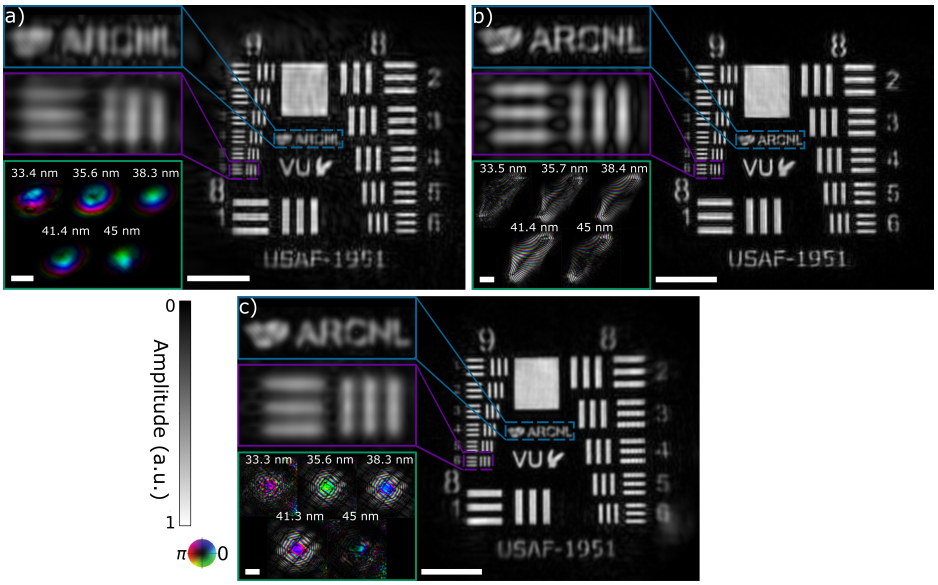

Figure 5.4: Reconstruction results from ptychographic measurements for (a) Gaussian, (b) vortex, (c) structured probes. Right: amplitude of reconstructed objects; top left: zoomed-in areas of the object; bottom left: dominant modes of the reconstructed probes of the five brightest harmonics. Scale bars in all figures correspond to 20 µm.

Figure 5.4 shows the reconstruction results from the ptychography measurements with the three different beam types. These results were obtained using two incoherent probe modes for each wavelength, similar to [40], in order to account for decoherence and other sources of noise in the forward model [35, 40]. To reduce the complexity of the problem, we constrained the object to look identical for all wavelengths, given that we use a binary, non-dispersive object. More details on the PIE-based reconstruction algorithm and the reconstruction results are given in Appendices 5.6.2 and 5.6.3 respectively. The reconstruction quality of the object upon vortex and structured beam illumination is clearly better than for Gaussian beam illumination, with fewer artifacts and sharper edges. Since the reconstructions give complex-valued expressions for the both the object and the probe, the object has been numerically propagated to remove a defocus term

that is caused by calibration errors of the wavelengths or the sample to camera distance.

In Fig. 5.4 we also show reconstructions for the dominant mode of the five brightest probes that range from 33.4 nm to 45 nm. The vortex probes are elongated due to the presence of astigmatism, as is explained in more detail in Appendix 5.6.1. For all beam shapes, the spectral weights reconstructed from ptychography are consistent with the grating measurement (Fig. 5.3g)). Small variations are apparent, as the ptychography scan effectively measures the average diffracted radiation flux from the object across the scanned area for all wavelength components. The resulting spectrum may differ from the grating measurement that was acquired by only sampling part of the Gaussian beam. For the smooth beam, the wavefronts of the weaker harmonics have more artifacts and are less trustworthy compared to the weak harmonics of the structured and vortex beam.

The significant difference in the quality of the reconstruction for the smooth beam can be attributed either to the smaller photon budget on the camera or the lower illumination diversity, likely to the combination of the two factors.

5.3.4 Simulations with reconstructed probes under comparable experimental conditions

To determine the cause of the difference in imaging performance and exclude the potential influence of experimental conditions, we set up simulations using the actual reconstructed probes and the SEM image of the object. In this simulation we ensured identical parameters such as object to camera distance $z = 106.8$ mm, spectral weights, overlap OV=90% and probe energy. Specifically, the probe energy was normalized such that the dataset with the vortex beams would have a 15-bit dynamic range. A combination of Poisson noise and Gaussian noise with standard deviation $\sigma = 40$ counts was added to the ptychograms.

The object and probe reconstructions of the synthetic ptychographic data are shown in Fig. 5.5. The improved imaging results with non-smooth beams (Figs. 5.5e,f,i,j)) compared to results with smooth beams (Figs. 5.5a,b)) remain clear, with similar trends as in Fig. 5.4. Note that there are slight discrepancies between the probes in Figs. 5.4 and 5.5, because the synthetic data were generated based on single-mode reconstructed beams, since no instability or decoherence effects were considered during the simulation. The assumption of perfectly coherent harmonic probes does not influence the hypothesis that is examined during this simulation, of how diversity caused by a structured beam can enhance the reconstructed image quality.

The achieved object resolution is determined using FRC between the true simulated object and one object reconstruction per probe beam and is shown in Figs. 5.4d,h,l). The resolution using the one-bit criterion is equal to 400 nm for the vortex beam, 1251 nm for the Gaussian beam and 414 nm for the structured beam. For the current experimental parameters, the highest achievable, diffraction-limited, resolution is 129 nm, assuming the shortest contributing wavelength component is 33.4 nm.

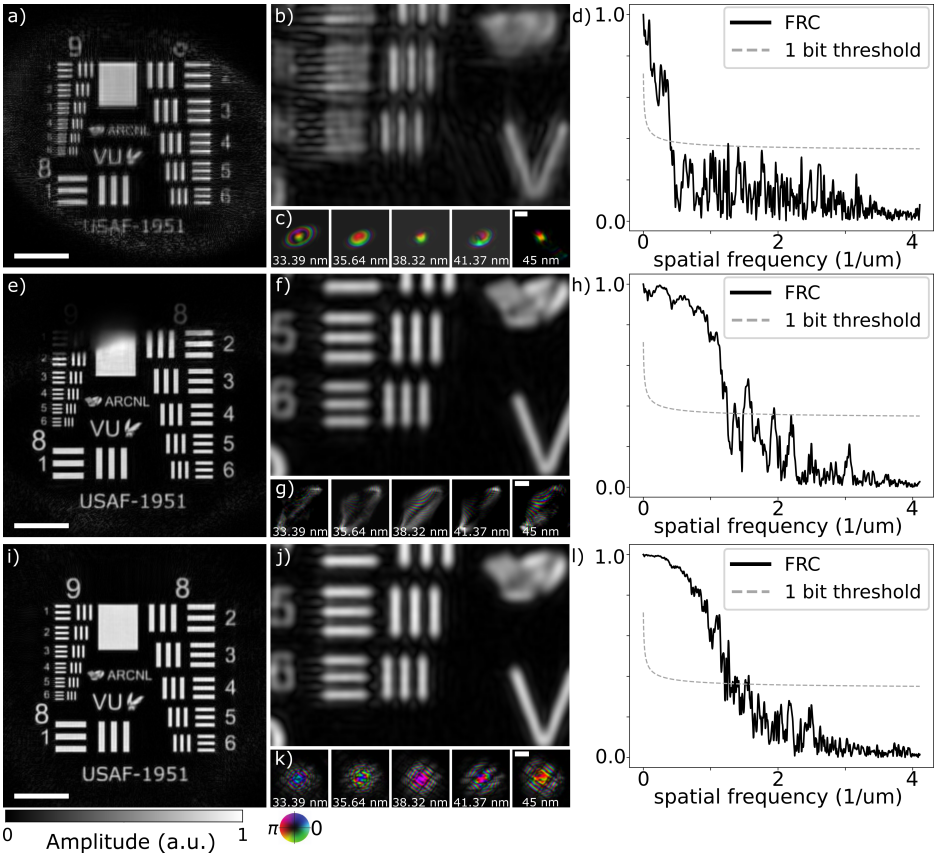

Figure 5.5: Reconstruction results from synthetic ptychographic datasets with (a-d) Gaussian, (e-h) vortex, (i-l) structured probes. (a,e,i) Amplitude of the reconstructed object. (b,f,j) Zoomed-in area of the object group 9/elements 5 and 6. (c,g,k) Probe reconstructions of the five brightest harmonics. (d,h,l) FRC computed by comparing object reconstructions with true object. Scale bars in all figures correspond to 20 µm.

5.3.5 Characterization of probe diversity

To compare the spectral and scanning diversity for the different beam types, we calculate spectrally resolved diffraction patterns at the detector plane. The probes, object and scan grid are identical to what we used in the simulations presented in Section 5.3.4, so that we can correlate the diversity metrics to the reconstruction results in Fig. 5.5. Moreover, the diversity metrics are calculated based on stable and coherent harmonic beams, without any long-term drifts.

The diversity is calculated according to the dissimilarity metrics presented in Section 5.2, and the results are shown in Fig. 5.6. The diffraction patterns used as input to Eqs. (5.1,5.2) for the calculation of diversity according to L1 norm, L2 norm, and the cosine metric were normalized with respect to the maximum

pixel value over the full dataset ($\max_{x,y,k} I_k(x,y) = 1$). We selected this normalization approach as it conserves relative intensity differences among different patterns, which contains relevant information that influences ptychography algorithm performance. On the other hand, for the diversity metric according to JSD (Eq. (5.3)), each diffraction pattern was normalized independently such that $\sum_{x,y} I_k(x,y) = 1$, $\forall k$, in accordance with the original definition of entropy from information theory. Different normalization strategies can be chosen: diversity results for different cases are given in Appendix 5.6.4 (Figs. 5.9, 5.10), which show different absolute values but very similar trends.

As shown by the calculated diversity metrics in Fig. 5.6, the vortex beam leads to the largest scanning diversity and spectral diversity, while the structured beam follows closely with high diversity values, especially according to cosine metric and JSD. These results are in close agreement with the reconstruction results of Fig. 5.5, where the vortex and structured beams were shown to lead to better object reconstructions than the Gaussian beam. Out of the four different metrics, both the JSD and cosine metrics reflect this difference in ptychography performance, showing significantly higher diversity values for the vortex and structured beams in a way that correlates with the image reconstruction quality. In comparison, the L1- and L2-norms are less clear, showing both larger variance and smaller differences between the beams.

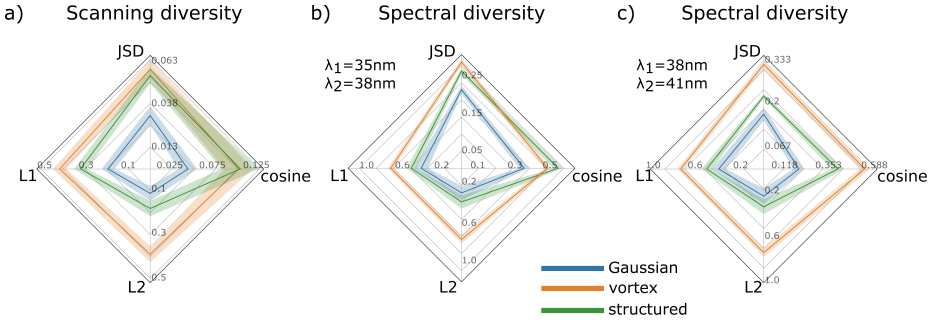

Figure 5.6: Diversity metrics for different probe beam structures. (a) scanning diversity of polychromatic diffraction patterns, (b) spectral diversity between diffraction patterns at wavelengths of 35.6 nm and 38.3 nm, (c) spectral diversity between diffraction patterns at wavelengths of 38.3 nm and 41.4 nm. The solid lines indicate the mean values of comparing adjacent scan positions (for scanning diversity) or wavelengths (for spectral diversity) over the whole diffraction patterns series, while the shaded areas have a width of one standard deviation.

5.3.6 Fisher information analysis

To further analyze the influence of structured illumination on the ptychographic reconstruction quality, we compare the Fisher information for the three previously described and experimentally reconstructed probes: Gaussian, vortex, and structured beam. The Fisher information quantifies the amount of information

a measured diffraction pattern contains about an unknown parameter θ, thereby setting a lower bound on the achievable precision in estimating that parameter (the Cramér-Rao lower bound). Given the observed improvement in ptychographic reconstruction quality with increased illumination diversity, it is worth investigating whether this improvement is accompanied by an increase in Fisher information. Such a finding would bolster our claim that the increased diversity in diffraction patterns achieved through structured illumination leads to more informative measurements, which subsequently enable better object reconstructions.

In general, the Fisher information is defined as $\mathcal{J}(\theta) = \mathbb{E}([\partial_\theta \ln p(X;\theta)]^2)$, where $\mathbb{E}$ denotes the expectation operator with respect to noise fluctuations, and $p(X;\theta)$ denotes a probability density function of a random variable X representing the observed data [210, 211]. The term $\partial_\theta \ln p(X;\theta)$ represents the partial derivative of the natural logarithm of the probability density function with respect to the parameter θ. In other words, the Fisher information describes how sensitive the measurement is to changes in θ. This sensitivity is directly related to the concept of diversity in diffraction patterns, as a more diverse set of patterns can be expected to contain more information about the object and its parameters.

In the case of ptychography, where the measurement noise is assumed to follow a Poisson distribution, the Fisher information associated with the l-th diffraction pattern for a single parameter θ can be expressed as [212]:

$$\mathcal{J}_l(\theta) = \sum_k \frac{1}{I_{k,l}} \left(\frac{\partial I_{k,l}}{\partial \theta} \right)^2 , \tag{5.4}$$

where I_k is the expected photon count at detector pixel k, and the sum runs over all pixels of the detector.

To explore the relationship between structured illumination and Fisher information, we consider two types of object parameters: a dimensionless scaling factor Δs, representing overall changes in the object's size, and a phase shift $\Delta\phi$ in radians, representing changes in the object's optical thickness. We study the same object shape as previously used in section 5.2, but as a transparent phase object instead of a binary amplitude object. Assuming a sample to camera distance of $z = 105\,\mathrm{mm}$ and the same experimental design as used in our experimental setup featuring an HHG source, we can numerically calculate the diffraction patterns for each parameter θ using the multi-wavelength XUV probes that were reconstructed and presented in section 5.3.3. The probe intensities are all normalized to a total photon count of 10×10^6 photons, and the object is scanned through the beams in a concentric pattern comprised of 219 positions. Using a centered finite difference scheme, we can then estimate the Fisher information as

$$\mathcal{J}_l(\theta) = \sum_l \frac{1}{I_{k,l}(\theta) + \epsilon} \left[\frac{I_{k,l}(\theta + \Delta\theta) - I_{k,l}(\theta - \Delta\theta)}{2\Delta\theta} \right]^2 , \tag{5.5}$$

where $\epsilon = 1 \times 10^{-6}$ denotes a regularization parameter with the physical interpretation of the expected value of additive Poissonian noise, and the step sizes

$\Delta\theta$ are chosen as $\Delta s = 5 \times 10^{-3}$ for the scaling factor, and $\Delta\phi = 1 \times 10^{-6}$ rad for the phase shift, respectively.

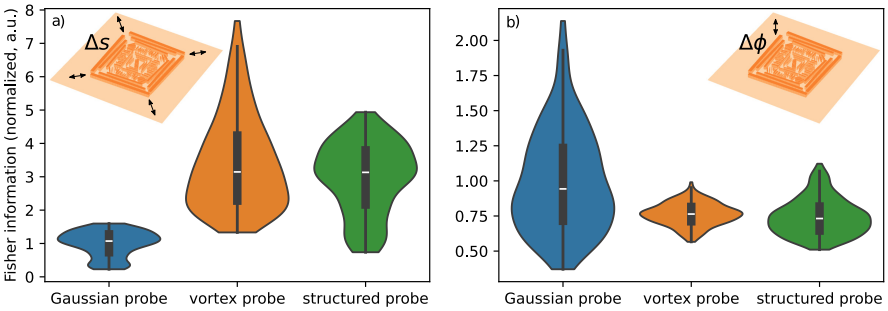

Figure 5.7: Fisher information for different probe beam structures. The shape of the violin plots describes the distribution of Fisher information per diffraction pattern (for a total of 219 scanning positions). The Fisher information is normalized by the average information achievable with a Gaussian probe. (a) Fisher information associated with a parameter s that determines the overall size and scale of the phase object shown as an inset plot. (b) Fisher information associated with the phase ϕ of the phase object shown as an inset plot.

For both object parameters, the Fisher information is shown in Fig. 5.7 independently of each other. To assess the distribution of information across the whole ptychography scan, we visualize the Fisher information per diffraction pattern as violin plots and normalize them by the average information that is achieved by Gaussian beam illumination. For the object scaling parameter s (Fig. 5.7a)), we observe a significant increase of information using structured illumination. Specifically, the vortex probe exhibits a total Fisher information about 3.4 times higher than the Gaussian probe. This translates into a reduction in the standard deviation of the estimate for this parameter by about 1.8 times, calculated as the square root of the inverse of the Fisher information (from the definition of the Cramr-Rao lower bound).

This finding supports our expectation that the increased diversity in the diffraction patterns leads to a higher sensitivity to changes of a parameter that is closely linked to the faithful reconstruction of the object's size and shape. The scaling factor directly affects the spatial frequencies in the diffraction patterns, which are crucial for achieving high-resolution reconstructions. Moreover, the scaling factor is intrinsically related to experimental parameters such as the wavelength and object-to-detector distance [46]. The enhanced sensitivity to the scaling factor through structured illumination can therefore lead to more accurate and precise object reconstructions, as well as improved retrieval of the experimental geometry from the ptychographic dataset.

Interestingly, we do not observe a significant difference in the Fisher information between structured and unstructured illumination for the phase parameter ϕ (Fig. 5.7b)). This suggests that phase sensitivity in ptychography may depend

on additional factors beyond beam structure, such as phase matching conditions as discussed in Ref. [213]. It is important to note that estimating the single parameter of the object's phase assumes prior knowledge of its shape. This assumption reduces the complexity of the ptychographic algorithm by alleviating the need to simultaneously retrieve spatial features, which may explain the relative invariance of the achievable estimation precision to the illumination diversity used.

5.4 Discussion

The concept of diversity metrics using diffraction patterns as a means to assess the expected image quality in ptychography is found to work well. Both the diversity among scan positions and the spectral diversity in a multi-wavelength ptychography experiment can be characterized with such metrics. From the Fisher information analysis, it follows that beams with high spatial and spectral diversity lead to increased sensitivity to spatial properties in ptychography datasets. As a result, ptychography with such high-diversity beams can be expected to lead to better image reconstructions at similar photon numbers and scan times. Although diversity metrics provide less quantitative insight than Fisher information, they consider the overall information content between measurements rather than the sensitivity to single parameters, which makes them well-suited in the assessment of imaging performance. Diversity metrics based on estimated diffraction patterns can therefore provide a way to optimize illumination beam profiles and secondary experimental parameters. From our experiments, we find that the JSD and cosine metric show clear correlation with image quality. These metrics have the additional advantage that they are bounded, meaning that the calculated diversity can be compared to the maximum possible diversity of a given dataset. While this correlation is not a direct predictor of image quality, they do allow a comparison of the expected imaging performance with different beams and objects, giving valuable insight already in the design phase of a ptychography experiment.

In contrast, the L1- and L2-norms show larger variations and less sensitivity to image reconstruction quality for different beams. This is likely due to the structure of these metrics (Eq. 5.1), which are more sensitive to absolute differences in intensity. Therefore, they are less reliable in quantifying structural changes between different diffraction patterns, in which the information for ptychography reconstructions is mainly contained.

Our experiments were designed in such a way that we could compare the spatial and spectral diversity when using beams without structure, with mainly spatial diversity induced by a binary mask, and with mainly spectral diversity through wavelength-dependent OAM. We find that both of these structured beam approaches provide enough spectral and scanning diversity to enable object reconstructions with improved resolution and fewer artifacts. Furthermore, individual probe modes that correspond to different wavelengths of the polychromatic beam are reconstructed in a more robust and reproducible way. While the structured

beams indeed lead to improved image reconstructions, an interesting finding is that both types of structuring result in comparable image quality and resolution. A possible explanation is the strong wavelength dependence of far-field diffraction, as a larger separation between diffraction orders results in better wavelength-resolved patterns as well. Strikingly, the spectral diversity between some harmonic orders is actually higher for the binary mask structuring than for the OAM beams (Fig. 5.6b)).

In the present work, the available HHG flux was the limiting factor in the experiments, as the measurements required exposure times that made the ptychography scans susceptible to drifts in beam pointing and ambient changes. In particular for the vortex XUV beam, the required exposure time was almost twice as long as for the diffraction-based structured beam to reach similar flux. This additional measurement time may also have led to a reduced reconstruction quality, which could offset the present conclusions given that the OAM beam shows the highest diversity among all the beams. Improving the HHG flux and using additional long-term stabilization systems would remove these uncertainties. Nevertheless, even though the beam structuring methods reduce the available HHG flux, the increased diversity remains a driver for reconstruction improvements.

First demonstrations of nanoscale-resolution ptychography on dispersive samples used monochromatic XUV light [35, 38]. The spectrally resolved probe reconstruction with multi-wavelength structured illumination in this work paves the way for broadband imaging of dispersive samples, aided by diversity metrics to design the required illumination profiles. This approach can unlock the full use of the potential of broadband XUV imaging systems for semiconductor wafer metrology and biological materials.

5.5 Conclusion

In conclusion, in this study we introduce diversity metrics in order to quantify the suitability of a coherent illumination type for ptychography experiments. We performed comparative measurements with various multi-wavelength XUV beam types, namely Gaussian, OAM, and structured by diffraction from a binary mask. Both simulation and experimental results verify that increased scanning and spectral diversity of diffraction patterns leads to improved imaging results at a given photon flux and measurement time. These diversity metrics therefore provide an intuitive design guideline for ptychography experiments, enabling a comparison of expected image reconstruction quality for different beam profiles and objects.

5.6 Appendix

5.6.1 Materials and methods

Drive laser for high harmonic generation

Our table-top HHG source is driven by an ultrafast NIR laser system. With an ytterbium-based laser system (Pharos from Light Conversion) delivering 170 fs pulses at a center wavelength of 1030 nm, 2 mJ pulses are obtained at a repetition rate of 1 kHz. For efficient high-harmonic generation, the pulses are compressed by a home-built post-compression system to a pulse duration ∼35 fs with an average power of 1.5 W [108]. The NIR beam is subsequently focused by an $f = 300$ mm lens into an argon gas jet confined in a 1 mm diameter metal tube, at a backing pressure of 5 bar. Moreover, an iris clips the beam before the focusing lens in order to improve the phase matching conditions for HHG.

Sample preparation

The binary USAF 1951 resolution target as used in the experiments is fabricated on a 120 nm thick gold layer sputter coated on a 50 nm silicon nitride free-standing membrane (Ted Pella Inc.). Patterning was performed with a 30 keV focused gallium ion beam (FEI Helios Nanolab 600) with a current of 0.28 nA and dwell time of 1000 ms. SEM image of the USAF is shown in Fig 5.3h). In our case, the sample thickness $\Delta z = 170$ nm and the smallest structure in the sample $\Delta x \approx 0.3$ µm meet the condition $\Delta z < 2(\Delta x)^2/\lambda$, which is referred to here as the projection approximation [214]. Therefore, the sample is mathematically represented by a two-dimensional transmission function, which is obtained by a projection of the refractive index along one spatial dimension.

Extreme ultraviolet optics

The XUV mirrors that have been used for focusing the HHG beams to the sample are molybdenum/silicon multilayer mirrors fabricated by optiXfab GmbH [215]. We use one plane and one curved mirror to steer and refocus the beam respectively. The bandwidth coverage of the mirrors is broadband (20 nm-55 nm) for the plane mirror and narrowband centered at 39 nm for the curved mirror, at an average reflectivity of 20% per mirror.

The indicated angle of incidence for maximized reflectivity is 5 degrees. However, oblique incidence on the curved mirror leads to astigmatism, as can be clearly observed in the ptychographic reconstruction of the vortex probes in Fig. 5.4b). A small amount of astigmatism is also noticeable in the smooth beam reconstruction (Fig. 5.4a)). The induced astigmatism to the wavefront is equal to $\frac{I^2}{2r}(y^2 - x^2)$, with I the incidence angle and r the radius of curvature of the mirror [192]. OAM beams have larger divergence compared to Gaussian beams, so the beam has a larger size on the curved mirror and the effect of astigmatism becomes stronger.

Data acquisition

The XUV camera in our experimental setup (Andor Ikon-L 936SO, 2048×2048 pixels, pixel size 13.5 µm, 15-bit dynamic range) has a constant background offset of approximately 320 counts for unbinned data when cooled to −60 °C. The CCD pixels were read-out at a rate of 1 MHz with preamplifier gain 2× for the vortex and structured beam measurements, where the signal was decreased compared to the smooth beam measurement.

To fully utilize the dynamic range of the camera, we set different exposure times for each measurement, equal to 10 s, 350 ms and 6 s for the vortex, Gaussian and structured beams respectively. This difference in exposure times per diffraction pattern creates different sensitivities to possible beam drifts and spectral jitter. To monitor slow drifts, we recorded a diffraction pattern at one specific scan position several times throughout the ptychographic measurement, as well as the polychromatic bare beam position before and after the measurement, and we did not observe any significant drift for either measurement. Spectral and pointing jitter can lead to blurring of the diffraction patterns, especially for long exposure times. The jitter can be modelled as a degree of incoherence in the beam, which we treated algorithmically by decomposing each high harmonic wavefront into incoherent modes. Given the limited amount of jitter, we found that using two modes is sufficient for ptychographic reconstruction.

The sample is mounted on a three-dimensional translation stage (Smaract SLC-1730). The translation lateral to the beam is required to perform ptychography scans and the longitudinal translation allows us to select a desired beam size and divergence at the sample plane.

5.6.2 Ptychographic reconstruction algorithm

The ptychographic reconstructions were performed with Ptylab.py [110]. In Ptylab, the PIM [44] algorithm has been implemented to describe the measured far-field diffraction pattern at position j as the incoherent sum of monochromatic diffraction patterns. For the specific experimental settings of Fig. 5.3 we have modified the general forward model expression to the following:

$$I_j \sim \sum_{\Lambda} \sum_{k\in\{0,1\}} \left(\mathscr{P}_{\Lambda}[P_{k,\Lambda}(\mathbf{r}) \cdot O(\mathbf{r}-\mathbf{r}_j)] \right)^2 + I_B$$

where Λ denotes the wavelength, k refers to the incoherent mixed states of each probe that account for sources of decoherence [35], the binary object O is identical for all wavelengths and $\mathscr{P}_{\Lambda}$ is the scaled angular spectrum propagator [110, 120] that permits the propagation of an electromagnetic wave under the Fresnel approximation [5] with wavelength-independent pixel size at the object plane. The mixed states of the probes are orthogonalized during the reconstruction via singular value decomposition. In Fig. 5.4 we show the probes with the highest singular values that correspond more to the physical representation of the beams, while for all simulations we do not use mixed states. Furthermore, the general forward model expression allows for the object to be different for every wavelength, but

in our demonstration we have simplified the formula by using a single object that looks identical for all wavelengths. The phase plots of the object shown in Fig. 5.8 verify that the object is binary and there is no requirement for considering different object representation for each wavelength. I_B is a constant background, iteratively updated according to [216], that is added to the forward model in order to take into account leakage of the fundamental beam to the detector. The update rules in the $(n+1)^{\text{th}}$ iteration for probe and object are then, according to [44, 110]

$$P_{n+1,k,\Lambda}(\mathbf{r}) = P_{n,k,\Lambda}(\mathbf{r}) + \beta_P \cdot \frac{O_n^*(\mathbf{r}-\mathbf{r}_j)\big(\psi - P_{n,k,\Lambda}(\mathbf{r})O_n(\mathbf{r}-\mathbf{r}_j)\big)}{\alpha_p|O_n(\mathbf{r})|^2_{max} + (1-\alpha_p)|O_n(\mathbf{r}-\mathbf{r}_j)|^2}$$

$$O_{n+1}(\mathbf{r}-\mathbf{r}_j) = O_n(\mathbf{r}-\mathbf{r}_j) + \beta_O \cdot \sum_{\Lambda}\sum_{k} \frac{P_{n,k,\Lambda}^*(\mathbf{r})\big(\psi - P_{n,k,\Lambda}(\mathbf{r})O_n(\mathbf{r}-\mathbf{r}_j)\big)}{\alpha_o|P_{n,k,\Lambda}(\mathbf{r})|^2_{max} + (1-\alpha_o)|P_{n,k,\Lambda}(\mathbf{r})|^2}$$

Since we use a single object representation for all wavelengths, we have modified the update rule given in [110] accordingly. Specifically, the update for the object is derived via the accumulated gradients from all spectral and decoherence modes of the probe. Moreover, for the reconstructions shown in Fig. 5.4, the regularization parameters α_p and α_o, which were first introduced in [217], were chosen equal to 0.99 in order to penalize updates of pixels with low signals, $\beta_p = 0.3$ and β_o was adjusted manually during the reconstruction from 0 to 0.3. Since the polychromatic beam on the camera plane was recorded before each ptychographic measurement, we implemented the modulus enforced probe technique [51] within the reconstruction process. A good initial guess based on earlier reconstructed results was used for the object in the results shown in Fig. 5.4, but the algorithms also converged with slightly worse performance if prior knowledge was assumed only for the probes and not for the object.

5.6.3 Additional information about the reconstruction of experimental data

Object reconstruction

In ptychography the imaging results are typically complex-valued expressions for the probe and object that correspond to the laser beam amplitude and phase and to the transmission (or reflection) function of the sample under examination. In this work we demonstrated our concept in a binary sample that is either fully opaque or fully transparent to all wavelengths. However, the reconstruction algorithm was not restricted to converge to a real-valued object. The complete object reconstruction results, after numerical propagation that remove any defocusing effects, are shown in Figs. 5.8a-c) for the three tested beam cases. We observe that indeed the algorithm has converged to a flat-phased object reconstruction for all beam cases, with only a minor residual phase variation of $\approx$0.65 rad at the edge of the object when illuminated by a vortex beam.

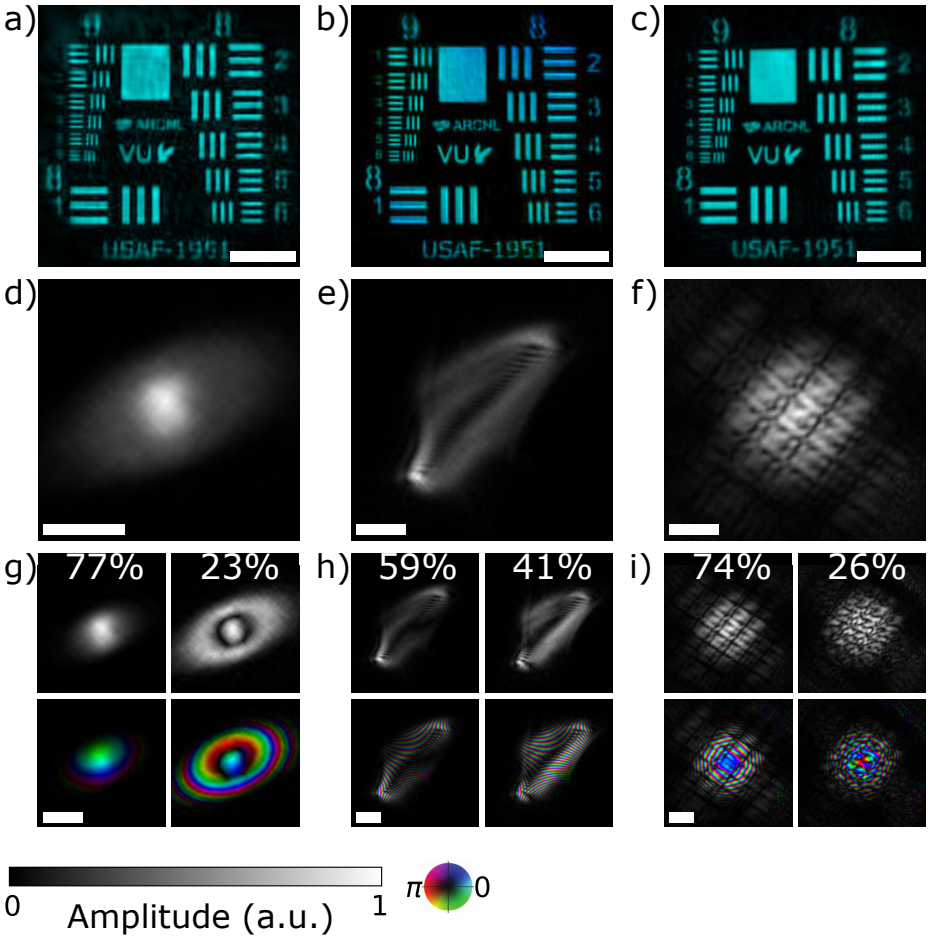

Figure 5.8: Complementary object and probe reconstructions for experimental data. (a-c) Complex-valued representations of the reconstructed object for (a) Gaussian, (b) vortex and (c) structured beam. (d-e) Amplitude of the partially coherent 27^{th} harmonic (38.3 nm) beams at the object plane. (g-i) Amplitude and complex-valued plots of the incoherent modes of the 27^{th} harmonic. In all complex-valued plots, brightness corresponds to amplitude and hue to phase. Scale bars in all figures are equal to 20 µm.

Probe reconstruction

As mentioned in Section 5.3.3 and Appendix 5.6.2, during the reconstruction we use two incoherent probe modes, also called mixed states, per wavelength. Figures 5.8d-f) show the amplitudes of the incoherent sums of the modes of the 27^{th} harmonic (38.3 nm) for the three different beam types, which correspond to a physical representation of the beam amplitude at this wavelength. We observe that both proposed methods to structure the HHG beam (diffraction mask-based and introducing OAM) lead to highly structured beam profiles. Fi-

nally, Figs. 5.8g-i) show amplitude and complex-valued plots of the incoherent probe modes of the 27^{th} harmonic, with the percentage of the total energy that is included in each mode.

5.6.4 Diversity metrics using different normalization strategies

The diversity metrics that have been used throughout this work, namely the L_1, L_2 norms, the cosine metric, and Jensen-Shannon divergence (JSD), were proposed by Iwasaki et al. [207] as appropriate to describe similarity between diffraction patterns, but originally have been defined and used in other disciplines. The L_p norms measure distance between vectors, making the results strongly dependent on the magnitude of the vectors, which in this application translates to the absolute intensity of the diffraction patterns. The cosine metric only measures the angle between two vectors, giving a result that is independent of any arbitrary scaling of the vector magnitudes. The JSD, on the other hand, has been defined as similarity metric between probability density functions (PDFs), so the two diffraction patterns that are inputs in the JSD equation need to be normalized accordingly, such that the integrated intensity over the whole detector area is equal to 1. If we abide by this normalization, JSD is a bounded metric, with the supremum $JSD_{max} = log2$ indicating maximum diversity.

For ptychography, the absolute value of the signal is an important parameter for successful reconstructions, as high pixel values imply better signal-to-noise ratio (SNR), although this aspect is not specifically relevant for diversity. However, it certainly affects the reconstruction quality if within the diffraction patterns series there are many low-signal diffraction patterns that mathematically give high diversity, but practically do not contain any significant information due to the low SNR. Therefore, it is relevant to assess the effect of including diffraction signal strengths in the diversity metrics on the achieved reconstruction quality.

Figure 4 in the main text shows L_1, L_2, and cosine results for normalization of the diffraction patterns such that the maximum pixel value over the whole series of diffraction patterns is equal to 1. This approach ensures that relative intensity variations among the diffraction patterns are included in the diversity metrics. For JSD a different choice was made, and each diffraction pattern has been normalized individually such that $\sum_{x,y} I(x,y) = 1$, in order to be consistent with the definition of entropy. In addition to this choice of normalization, we can consider alternative normalization methods to calculate both scanning and spectral diversity, and investigate their effect on the different metrics and their correlation to the ptychographic image reconstruction results. The normalization procedures that we considered can be listed as follows:

1. Global normalization: normalize all diffraction patterns that correspond to different scan positions (and different wavelengths if applicable) by the same number, such that $\max_{x,y,k} I_k(x,y) = 1$, with $x, y \in [1, N], k \in [1, K]$

2. Local normalization: normalize each diffraction pattern that corresponds

to a different scan position (and a different wavelength if applicable) individually, such that $\max_{x,y} I_k(x,y) = 1$, with $x, y \in [1, N], k \in [1, K]$

3. Local normalization on total flux: normalize each diffraction pattern that corresponds to a different scan position (and a different wavelength if applicable) individually, such that $\sum_{x,y} I_k(x,y) = 1$, with $x, y \in [1, N], k \in [1, K]$

4. Local normalization including spectral weights: normalize two monochromatic diffraction patterns that correspond to the same scan position by the same number, such that $\max_{x,y,\lambda} I_{k,\lambda}(x,y) = 1$, with $x, y \in [1, N], k \in [1, K], \lambda \in \{\lambda_1, \lambda_2\}$

where K is the number of scan positions and $N \times N$ is the size of the detector.

In Figs. 5.9, 5.10 we show results of scanning and spectral diversity respectively for these different normalization strategies as applied to all four metrics. The results indicate that the L_1 and L_2 norms are very sensitive to the normalization strategy, even to the point where their difference becomes insignificant when using local normalization (Fig. 5.9b)). We attribute this behaviour to the situation as described above, where the local normalization results in an increased weight of low-intensity diffraction patterns on the diversity metrics. As such low-intensity patterns contain significant noise, overestimating their weights will lead to higher diversity estimates, as white noise in principle has very high diversity between separate measurements. Therefore, when using L_p norms as a diversity metric, global normalization is required to properly account for true signal variations across the ptychography scan. In contrast, the cosine norm is independent of the normalization, which is to be expected as the angle between vectors is not affected by relative amplitude differences. This feature makes the metric more robust against the choice of normalization and therefore more flexible. However, its independence of the magnitude may form a limitation, as it may become less clear how to identify the influence of low SNR in a ptychography dataset. As long as data of sufficiently high SNR can be guaranteed, the cosine metric is a suitable way to assess diversity in a dataset.

The JSD is quite different from the other considered metrics, as it does not consider measurements as vectors, but rather as probability distributions. Diversity is then quantified as the difference in information content instead of norms or projections of vectors. This concept seems naturally suited to assess diversity in measured diffraction 'information', but does require a different treatment to allow such an interpretation. Interpreting a diffraction measurement as a probability distribution requires the total probability of all registered events to add up to one. This corresponds to the approach of local normalization on flux, as used in Figs. 5.9c) and 5.10d). With this approach, the JSD is a bounded metric with a clear interpretation of diversity in terms of new information added by each next diffraction pattern, which is clearly attractive for experiment design and analysis. However, such a local normalization approach does have the risk of becoming too sensitive to noise when there are many low-SNR diffraction patterns in a dataset, as was discussed above for the L_p norms. Therefore, one could

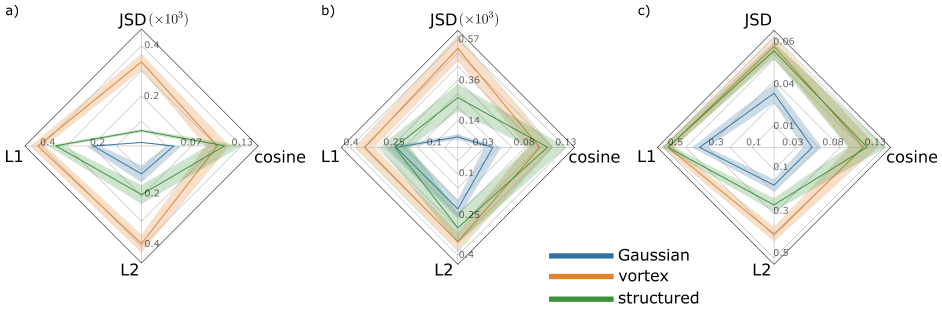

Figure 5.9: Scanning diversity metrics for different normalization strategies. (a) Global normalization, (b) Local normalization, (c) Local normalization on total flux. The solid lines indicate the mean values of comparing adjacent scan positions for scanning diversity over the whole diffraction patterns series, while the shaded areas have a width of one standard deviation. Note the different horizontal and vertical scales.

argue that JSD with a global normalization approach has advantages, as it significantly reduces this noise sensitivity. Comparing the JSD results in Figs. 5.9 and 5.10, we find that the trends in JSD for our datasets are largely independent of the chosen normalization, although the variance is significantly reduced for global normalization. This does make it easier to assess trends in JSD, but global normalization removes the absolute upper bound and reduces the JSD to a relative metric.

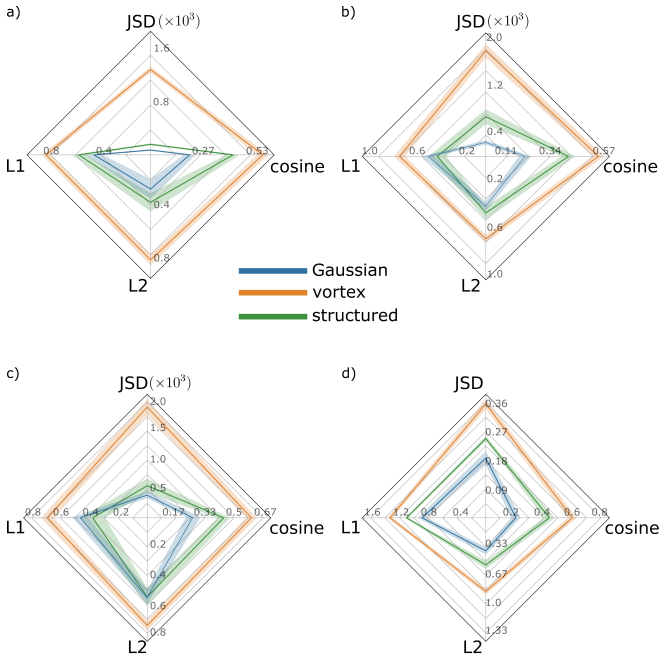

Figure 5.10: Spectral diversity metrics for monochromatic diffraction patterns at 38.3 nm and 41.4 nm for different normalization strategies. (a) Global normalization, (b) Local normalization, (c) Local normalization including spectral weights, (d) Local normalization on total flux. The solid lines indicate the mean values of comparing wavelengths over the whole diffraction patterns series, while the shaded areas have a width of one standard deviation. Note the different horizontal and vertical scales.

List of publications

Chapter 2

A. Pelekanidis, K.S.E. Eikema, and S. Witte, "Far-field optical propagators with user-defined object-plane pixel size for ptychography," Opt. Continuum **4**, 804–825 (2025).

Author contributions: AP, KSE and SW conceived the idea and designed the experiments. AP derived the mathematical formulas. AP performed simulations, experiments and the ptychographic reconstructions. AP developed analysis codes and performed data analysis. AP, KSE and SW interpreted data. KSE and SW supervised research. AP wrote the manuscript, which was reviewed and edited by all authors.

Chapter 3

X. Liu, A. Pelekanidis, M. Du, F. Zhang, K.S.E. Eikema, and S. Witte, "Observation of chromatic effects in high-order harmonic generation," Phys. Rev. Res. 4, 5:043100 (2023).

Author contributions: XL, AP, MD, FZ, KSE and SW conceived the idea and designed the experiments. XL fabricated the wavefront sensors. XL, AP and FZ conducted the experiments. XL performed the ptychographic reconstructions. AP performed the simulations. FZ calculated the focal positions from the experimental data. XL, AP, MD, FZ, KSE and SW interpreted data. KSE and SW supervised research. XL, AP and SW wrote the manuscript, which was reviewed and edited by all authors.

Chapter 4

A. Pelekanidis, F. Zhang, K.S.E. Eikema, and S. Witte, "Generation dynamics of broadband extreme ultraviolet vortex beams," ACS Photonics **12**, 1638–1649 (2025).

Author contributions: AP, FZ, KSE and SW conceived the idea and designed the experiments. FZ fabricated the wavefront sensors. AP and FZ conducted the experiments. AP developed analysis codes and performed data

analysis. AP, FZ, KSE and SW interpreted data. KSE and SW supervised research. AP wrote the manuscript, which was reviewed and edited by all authors.

Chapter 5

A. Pelekanidis, F. Zhang, M. Gouder, J. Seifert, M. Du, K.S.E. Eikema, and S. Witte, "Illumination diversity in multiwavelength extreme ultraviolet ptychography," Photonics Research **12**, 2757–2771 (2024).

Author contributions: AP, FZ, MG, MD, KSE and SW conceived the idea and designed the experiments. FZ fabricated the sample and the binary mask. AP and FZ conducted the experiments. FZ performed simulations with smooth beam with increasing divergence. AP performed the ptychographic reconstructions with experimental data. AP performed simulations with reconstructed probes under comparable experimental conditions. AP developed analysis codes and performed diversity characterization and data analysis. JS performed Fisher information analysis. AP, FZ, MG, JS, KSE and SW interpreted data. KSE and SW supervised research. AP and FZ wrote the manuscript, which was reviewed and edited by all authors.

The author also contributed to the following publications:

[1]M. Du, X. Liu, A. Pelekanidis, F. Zhang, L. Loetgering, P. Konold, C.L. Porter, P. Smorenburg, K.S.E. Eikema, and S. Witte, "High-resolution wavefront sensing and aberration analysis of multi-spectral extreme ultraviolet beams," Optica 10:255-63 (2023).

[2]L. Loetgering, M. Du, D.B. Flaes, T. Aidukas, F. Wechsler, D.S. Penagos Molina, M. Rose, A. Pelekanidis, W. Eschen, J. Hess, T. Wilhein, R. Heintzmann, J. Rothhardt, and S. Witte, "PtyLab. m/py/jl: a cross-platform, open-source inverse modeling toolbox for conventional and Fourier ptychography," Opt. Express 31:13763-97 (2023).

[3]F. Zhang, A. Pelekanidis, A. Karpavicius, M. Gouder, J. Seifert, K.S.E Eikema, and S. Witte "Characterizing post-compression of mJ-level ultrafast pulses via loose focusing in a gas cell," Opt. Express 32:40990-1003 (2024).

Summary

The need to accurately image microscopic features that cannot be simply resolved by the human eye has led to the development of microscopes and complicated imaging techniques. Imaging systems can be divided into lens-based systems, that use a series of lenses between the object of interest and the detector to achieve a magnified image of the object, and lensless systems, where there are no optics between the object and the detector. In this thesis we study one specific lensless imaging technique called ptychography. In ptychography the object of interest is illuminated by a coherent light source, such as light from a monochromatic laser. As the light transmits through or reflects from the object, it gets diffracted. A camera is placed at a certain distance from the object and captures the diffraction pattern. The object is placed on a moving stage and can move laterally to the laser beam. In this configuration, we expose the camera to a series of diffraction patterns from different, but overlapping illuminated areas of the objects. Finally, we run a numerical reconstruction algorithm that gives complex-valued expressions of the object, which corresponds to the object transmission (or reflection) function, and of the laser beam, which describes the wavefront at the object plane. Since it is a lensless imaging technique, applicability of ptychography is not constrained by availability of focusing optics, such as lenses or mirrors, for a desired illumination wavelength. We can, therefore, perform a ptychography experiment with any type of coherent light source, while achieving resolution levels proportional to the wavelength of the light source.

Imaging resolutions in the nanometer range can be achieved with illuminating light sources in the extreme ultraviolet (XUV) and soft-x-ray (SXR) spectrum. Coherent XUV and SXR can be generated with tabletop sources via high harmonic generation (HHG), which is a highly non-linear process during which we generate high harmonics of a drive laser with wavelength typically in the infrared or visible spectrum. The output of the HHG process is a number of odd harmonics of the drive laser extending to the XUV and SXR range, with each harmonic exhibiting high spatial coherence properties. Depending on the application we can either select one harmonic to illuminate our object of interest or use the polychromatic beam and apply a modified reconstruction algorithm designed for multi-wavelength ptychography measurements. Here we implement this multi-wavelength ptychographic approach for XUV beams generated via HHG.

In the second chapter we study the computational models for the propagation of the light wave from the object plane to the camera plane. In the most common

ptychographic configuration with monochromatic light, the propagation of light to the far field can be calculated via a discrete Fourier transform, provided the pixel size at the object plane is properly defined as $dx = \frac{\lambda z}{N dq}$, where λ, z, N, dq are the wavelength, the distance between object and camera, the number of pixels of the camera along one dimension and camera pixel size, respectively. In the case of polychromatic illumination of the sample, it may be convenient for the user to define a universal pixel size for the object and the illumination that is independent of the wavelength. In chapter 2, we compare three propagation models suggested in the literature with user-defined pixel sizes for the object. We demonstrate that all three of them are equivalent, as they all originate from the Fresnel integral that describes the propagation of light under the paraxial approximation. However, each model has two alternative versions, which we also study and compare.

The third chapter is dedicated to the investigation and experimental validation of chromatic aberration effects in HHG. For this purpose we perform ptychographic wavefront sensing (PWFS) measurements. In PWFS measurements the object is a specially designed binary mask that facilitates the accurate and robust reconstruction of multiple harmonic wavefronts. By numerically backpropagating the reconstructed wavefronts to the generation plane of HHG, and associating the backpropagated wavefronts with the drive laser wavefront, we can draw conclusions about the physical processes that take place during HHG. Specifically in this work we did a series of PWFS measurements where we varied the drive laser focus position with respect to the generation plane and calculated the -real or virtual- focus positions of each high harmonic beam. The experimental results showed that there is strong chromatic aberration among the harmonic beams when the laser focus position is behind the generation plane, whereas chromatic aberration is minimized for the laser focus position in front of the generation plane. We also implemented a theoretical model that is in close agreement with the experimental findings.

In chapter 4 we perform PWFS measurements for HHG beams carrying orbital angular momentum (OAM) generated by an OAM drive laser. OAM is a property of laser beams associated with a doughnut-shaped intensity profile and a topological charge, which is a phase term of the form $e^{il\phi}$, where i is the imaginary unit, l is the topological charge and ϕ is the azimuthal angle in polar coordinates. In this work we also perform a series of PWFS measurements, for varying laser focus positions and varying astigmatism levels in the drive laser, and study how the doughnut shape is affected in the far field and through the propagation of the HHG beams along the focus. We also study the broadening of the OAM modal content of the high harmonics when the drive laser beam has modal impurities, such as increased aberrations. The experimental results are compared with theoretical predictions that help us explain the physical mechanisms of HHG with a drive beam carrying OAM.

Finally in the last chapter we shift the emphasis to the imaging of an object using a multi-wavelength HHG beam. We introduce the concept of diversity, claiming that as ptychography is a scanning technique, the diffraction pattern from every new scan position should add new information compared to previous

scan positions in order to get an optimized imaging result. The same principle should hold when comparing monochromatic diffraction patterns comprising the measured polychromatic diffraction pattern, as independent reconstruction at multiple wavelengths is more challenging when the information from different monochromatic diffraction patterns is strongly overlapped on the camera. To confirm our hypothesis, we perform ptychographic imaging measurements and simulations with different illumination diversities. Two ways to add diversity to an HHG beam are by inserting a diffractive mask in the beamline upstream of the sample or by generating harmonics carrying OAM, as shown in chapter 4. We observe enhanced resolution and imaging quality when the beams are characterized by high diversity.

Acknowledgments

This PhD thesis booklet signals the end of a journey that lasted more than four years in ARCNL in Amsterdam. It has been an exciting journey, where I have learned, sometimes from the basics, a lot of things about optics, imaging, laser physics, but also more tangible stuff related to the work in a laser lab. I feel very lucky and happy to have worked with my colleagues, who contributed more than they may think to the contents of this thesis.

First of all I would like to thank Stefan, my promotor. Stefan, you gave me the opportunity to be part of your team and trusted me to work initially in the NIR and later in the HHG lab, even though I had no relevant lab experience and had a background of Electrical Engineering. During the PhD, you always supported my work and helped me with the problems and challenges that emerged. You seemed to not be bothered with every rant I sent you on Teams, with long messages sharing my tiny progress every time and thoughts on the results; you were supportive and patient and used to reply even on late evenings and weekends. I appreciate all the trust, the support and the assistance.

I would also like to thank my co-promotor, Kjeld, for all the contributions during Tuesday meetings and paper reviews. Your expertise and experience were always helpful and appreciated.

Most of the experimental work in this thesis would not be completed without the immense help and contribution of Fengling. You started your PhD in the group one year later than me, but caught up in the lab very quickly. I could always count on you for your help during the HHG ptychography measurements. Also I appreciate how you were always eager to discuss research-related topics during our short journal club and at the office room, among other random, sometimes gossip, stuff. We went to a summer school in Poland and conferences in Germany, France and the Netherlands and we organized the defense party for our friend Kevin with much success. I always praised your skills in the lab, but I should mention that your assistance and contributions extended far beyond the lab work, and thank you for that. It is worth remarking that the nice collaboration we had, led to the successful publication we share, included as Ch. 5 in this thesis.

Kevin, thank you for teaching me how to work in the lab, for all the patience and the trust in me when we worked together during your last year in ARCNL. A particular thanks for not being angry when I messed up in the lab, while you were under pressure to finish your projects. Of course, our efficient collaboration also led to a publication, which I include as Ch. 3 in the thesis.

A special thanks should go to Maisie and Lars, the two postdocs in the HHG subgroup, for mentoring me during my beginning as a PhD student, for sharing with me all the knowledge and experience they had in ptychography and for their tutoring on how to use their codes for ptychographic reconstructions. They both guided me on my first ptychographic measurements in the NIR laser lab, teaching me how to use the optics and doing alignment 101. Their ideas resonated with the group and inspired a lot of the new projects that were assigned to me and newer PhDs even years after they had left.

I would also like to thank Jan for all the help in the lab, for teaching me how to use equipment such as the FROG and the autocorrelator, for giving ideas, but also practically helping with alignment problems and every single small or big issue that happened in the lab.

Matthias, you joined the group approximately when I entered the second half of my PhD, and your passion for learning and trying out new ideas in the lab inspired us all and gave us more energy, even in periods when we had stagnated with the lab work. Thank you for the cool ideas, the discussions and the rivers of questions, for doubting everything and putting me in a position that I had to think twice before I give an answer. Thank you for not accepting as an answer what I commonly said "this is how we've been doing this all this time in the lab".

I should also say a big thanks to Nik for the technical help in the lab, but also the software engineers in AMOLF and Arend-Jan for his help in the lab during the last few months after Nik left the group.

Jacob, I've known you a bit since you did your PhD in Utrecht, but I got to know you better during the few months you spent as a postdoc in the EUVGI group. Despite the short time you spent here, your contributions to everyone's work were very important and helped make our scientific papers better.

Augustas and Aaron, thank you for your participation and contributions in all the endless discussions during the subgroup meetings, where we tried to make sense out of the experimental data. But a big thanks to the rest of the EUVGI group as well, to current and old members, Maksym and Matthijs, Randy, Zeudi, Edcel with your questions and your suggestions you had an active contribution to the results and conclusions presented in this thesis.

As I am approaching the end of the acknowledgements, I would like to also thank everyone in ARCNL for the nice environment. It felt like home to be coming to the institute and I will remember the friendly atmosphere. I would like to especially thank the management team during my PhD time, Joost, Wim and Marjan, for managing the institute with these high standards.

My PhD life would not be the same without my good friends in the Netherlands that have been a family to me. A big thanks to Tworit, Spiros, Athina, Dimitris P, but also a big thanks to my old friends from Greece, Pantelis, Roksani, Athina V, Tasos, Manos to whom I knew I always had a safe space to grumble when things didn't go smoothly.

To my mum, my dad and my brother Theo, I know you've been happier than me with my successes and even sadder than me with all the challenges. You have supported me all along practically and mostly emotionally and I thank you deeply for that.

Finally, I would like to thank Despoina, my partner, flatmate and best friend for this amazing journey we have made together in the Netherlands. We've lived through COVID isolation times, house movings, happy moments and successes, but also sad events and hardships. In the end, you've been always there and supported every small or big step we made together.

-Antonios

Bibliography

[1] A. Ozcan and E. McLeod, *Lensless Imaging and Sensing*, Annual Review of Biomedical Engineering **18**:77–102 (2016). 1

[2] T. Latychevskaia, *Chapter One - Phase retrieval methods applied to coherent imaging*, in M. Htch and P. W. Hawkes (editors), *Advances in Imaging and Electron Physics*, vol. 218 of *Advances in Imaging and Electron Physics*, pp. 1–62, Elsevier (2021). 1

[3] E. Abbe, *Beiträge zur Theorie des Mikroskops und der mikroskopischen Wahrnehmung*, Archiv für mikroskopische Anatomie **9**(1):413–468 (1873). 1, 20, 90

[4] L. Loetgering, S. Witte, and J. Rothhardt, *Advances in laboratory-scale ptychography using high harmonic sources*, Optics Express **30**(3):4133–4164 (2022). 2, 4, 8, 12

[5] J. W. Goodman, *Introduction to Fourier optics*, Roberts and Company publishers (2005). 2, 20, 22, 107

[6] D. Gabor, *A new microscopic principle*, Nature **161**:777–78 (1948). 3

[7] E. N. Leith and J. Upatnieks, *Reconstructed wavefronts and communication theory*, Journal of the Optical Society of America **52**(10):1123–1130 (1962). 3

[8] G. W. Stroke, *Lensless Fourier-transform method for optical holography*, Applied Physics Letters pp. 201–203 (1965). 3

[9] I. McNulty, J. Kirz, C. Jacobsen, E. H. Anderson, M. R. Howells, and D. P. Kern, *High-Resolution Imaging by Fourier Transform X-ray Holography*, Science **256**(5059):1009–1012 (1992). 3

[10] S. Eisebitt, J. Lüning, W. Schlotter, M. Lörgen, O. Hellwig, W. Eberhardt, and J. Stöhr, *Lensless imaging of magnetic nanostructures by X-ray spectroholography*, Nature **432**(7019):885–888 (2004). 3

[11] W. Hoppe and J. Gassmann, *Phase correction, a new method to solve partially known structures*, Acta Crystallographica Section B: Structural Crystallography and Crystal Chemistry **24**(1):97–107 (1968). 3

[12] J. R. Fienup, *Reconstruction of an object from the modulus of its Fourier transform*, Optics Letters **3**(1):27–29 (1978). 3

[13] R. P. Millane, *Phase retrieval in crystallography and optics*, Journal of the Optical Society of America A **7**(3):394–411 (1990). 3

[14] J. Miao, P. Charalambous, J. Kirz, and D. Sayre, *Extending the methodology of X-ray crystallography to allow imaging of micrometre-sized non-*

crystalline specimens, Nature **400**(6742):342–344 (1999). 3

[15] R. L. Sandberg, A. Paul, D. A. Raymondson, S. Hädrich, D. M. Gaudiosi, J. Holtsnider, R. I. Tobey, O. Cohen, M. M. Murnane, and H. C. Kapteyn, *Lensless diffractive imaging using tabletop coherent high-harmonic soft-x-ray beams*, Physical Review Letters **99**(9):098103 (2007). 3

[16] H. N. Chapman and K. A. Nugent, *Coherent lensless X-ray imaging*, Nature Photonics **4**(12):833–839 (2010). 3

[17] D. F. Gardner, B. Zhang, M. D. Seaberg, L. S. Martin, D. E. Adams, F. Salmassi, E. Gullikson, H. Kapteyn, and M. Murnane, *High numerical aperture reflection mode coherent diffraction microscopy using off-axis apertured illumination*, Optics Express **20**(17):19050–19059 (2012). 3

[18] S. Witte, V. T. Tenner, D. W. Noom, and K. S. Eikema, *Lensless diffractive imaging with ultra-broadband table-top sources: from infrared to extreme-ultraviolet wavelengths*, Light: Science & Applications **3**(3):e163–e163 (2014). 4, 15, 90

[19] K. Itoh and Y. Ohtsuka, *Fourier-transform spectral imaging: retrieval of source information from three-dimensional spatial coherence*, Journal of the Optical Society of America A **3**(1):94–100 (1986). 4

[20] G. S. M. Jansen, D. Rudolf, L. Freisem, K. S. E. Eikema, and S. Witte, *Spatially resolved Fourier transform spectroscopy in the extreme ultraviolet*, Optica **3**(10):1122–1125 (2016). 4, 15

[21] G. S. M. Jansen, A. d. Beurs, X. Liu, K. S. E. Eikema, and S. Witte, *Diffractive shear interferometry for extreme ultraviolet high-resolution lensless imaging*, Optics Express **26**(10):12479–12489 (2018). 4, 15, 46, 90

[22] A. C. C. de Beurs, X. Liu, G. S. M. Jansen, A. P. Konijnenberg, W. M. J. Coene, K. S. E. Eikema, and S. Witte, *Extreme ultraviolet lensless imaging without object support through rotational diversity in diffractive shearing interferometry*, Optics Express **28**(4):5257–5266 (2020). 4, 15

[23] J. Rodenburg, A. Hurst, and A. Cullis, *Transmission microscopy without lenses for objects of unlimited size*, Ultramicroscopy **107**(2):227–231 (2007). 4, 6, 20, 90

[24] J. M. Rodenburg and H. M. L. Faulkner, *A phase retrieval algorithm for shifting illumination*, Applied Physics Letters **85**(20):4795–4797 (2004). 4, 20, 63, 90

[25] J. M. Rodenburg, A. Hurst, A. G. Cullis, B. R. Dobson, F. Pfeiffer, O. Bunk, C. David, K. Jefimovs, and I. Johnson, *Hard-x-ray lensless imaging of extended objects*, Physical Review Letters **98**(3):034801 (2007). 4

[26] P. Thibault and M. Guizar-Sicairos, *Maximum-likelihood refinement for coherent diffractive imaging*, New Journal of Physics **14**(6):063004 (2012). 6

[27] J. Seifert, Y. Shao, R. van Dam, D. Bouchet, T. van Leeuwen, and A. P. Mosk, *Maximum-likelihood estimation in ptychography in the presence of Poisson–Gaussian noise statistics*, Optics Letters **48**(22):6027–6030 (2023). 6

[28] P. Thibault, M. Dierolf, A. Menzel, O. Bunk, C. David, and F. Pfeiffer, *High-resolution scanning X-ray diffraction microscopy*, Science

321(5887):379–382 (2008). 6, 7, 20, 90

[29] M. Guizar-Sicairos and J. R. Fienup, *Phase retrieval with transverse translation diversity: a nonlinear optimization approach*, Optics Express **16**(10):7264–7278 (2008). 6

[30] A. M. Maiden and J. M. Rodenburg, *An improved ptychographical phase retrieval algorithm for diffractive imaging*, Ultramicroscopy **109**(10):1256–1262 (2009). 6, 7, 97

[31] P. D. Baksh, M. Odstrčil, H.-S. Kim, S. A. Boden, J. G. Frey, and W. S. Brocklesby, *Wide-field broadband extreme ultraviolet transmission ptychography using a high-harmonic source*, Optics Letters **41**(7):1317–1320 (2016). 6, 20, 90, 97

[32] M. D. Seaberg, B. Zhang, D. F. Gardner, E. R. Shanblatt, M. M. Murnane, H. C. Kapteyn, and D. E. Adams, *Tabletop nanometer extreme ultraviolet imaging in an extended reflection mode using coherent Fresnel ptychography*, Optica **1**(1):39–44 (2014). 6, 90

[33] P. D. Baksh, M. Ostrčil, M. Miszczak, C. Pooley, R. T. Chapman, A. S. Wyatt, E. Springate, J. E. Chad, K. Deinhardt, J. G. Frey, and W. S. Brocklesby, *Quantitative and correlative extreme ultraviolet coherent imaging of mouse hippocampal neurons at high resolution*, Science Advances **6**(18):eaaz3025 (2020). 6, 7, 13

[34] L. Loetgering, X. Liu, A. C. C. D. Beurs, M. Du, G. Kuijper, K. S. E. Eikema, and S. Witte, *Tailoring spatial entropy in extreme ultraviolet focused beams for multispectral ptychography*, Optica **8**(2):130–138 (2021). 6, 8, 9, 20, 46, 47, 48, 90, 93

[35] W. Eschen, L. Loetgering, V. Schuster, R. Klas, A. Kirsche, L. Berthold, M. Steinert, T. Pertsch, H. Gross, M. Krause, *et al.*, *Material-specific high-resolution table-top extreme ultraviolet microscopy*, Light: Science & Applications **11**(1):117 (2022). 6, 8, 9, 13, 20, 90, 98, 105, 107

[36] C. Liu, W. Eschen, L. Loetgering, D. S. Penagos Molina, R. Klas, A. Iliou, M. Steinert, S. Herkersdorf, A. Kirsche, T. Pertsch, *et al.*, *Visualizing the ultra-structure of microorganisms using table-top extreme ultraviolet imaging*, PhotoniX **4**(1):6 (2023). 6, 7, 13, 20

[37] A. Pelekanidis, F. Zhang, M. Gouder, J. Seifert, M. Du, K. S. E. Eikema, and S. Witte, *Illumination diversity in multiwavelength extreme ultraviolet ptychography*, Photonics Research **12**(12):2757–2771 (2024). 6, 20, 62, 63, 66

[38] M. Tanksalvala, C. L. Porter, Y. Esashi, B. Wang, N. W. Jenkins, Z. Zhang, G. P. Miley, J. L. Knobloch, B. McBennett, N. Horiguchi, S. Yazdi, J. Zhou, M. N. Jacobs, C. S. Bevis, R. M. Karl, *et al.*, *Nondestructive, high-resolution, chemically specific 3D nanostructure characterization using phase-sensitive EUV imaging reflectometry*, Science Advances **7**(5):eabd9667 (2021). 6, 13, 20, 90, 105

[39] H. Lu, M. Odstril, C. Pooley, J. Biller, M. Mebonia, G. He, M. Praeger, L. Juschkin, J. Frey, and W. Brocklesby, *Characterisation of engineered defects in extreme ultraviolet mirror substrates using lab-scale extreme ultraviolet reflection ptychography*, Ultramicroscopy **249**:113720 (2023). 6,

7, 13, 90

[40] Y. Shao, S. Weerdenburg, J. Seifert, H. P. Urbach, A. P. Mosk, and W. Coene, *Wavelength-multiplexed multi-mode EUV reflection ptychography based on automatic differentiation*, Light: Science & Applications **13**(196) (2024). 6, 7, 13, 21, 90, 98

[41] O. Bunk, M. Dierolf, S. Kynde, I. Johnson, O. Marti, and F. Pfeiffer, *Influence of the overlap parameter on the convergence of the ptychographical iterative engine*, Ultramicroscopy **108**(5):481–487 (2008). 6, 98

[42] J. Spence, U. Weierstall, and M. Howells, *Coherence and sampling requirements for diffractive imaging*, Ultramicroscopy **101**(2-4):149–152 (2004). 6, 31

[43] P. Thibault and A. Menzel, *Reconstructing state mixtures from diffraction measurements*, Nature **494**(7435):68–71 (2013). 6, 11, 14, 90

[44] D. J. Batey, D. Claus, and J. M. Rodenburg, *Information multiplexing in ptychography*, Ultramicroscopy **138**:13–21 (2014). 7, 14, 20, 22, 90, 91, 107, 108

[45] M. Odstrcil, P. Baksh, S. Boden, R. Card, J. Chad, J. Frey, and W. Brocklesby, *Ptychographic coherent diffractive imaging with orthogonal probe relaxation*, Optics Express **24**(8):8360–8369 (2016). 7

[46] L. Loetgering, M. Du, K. S. Eikema, and S. Witte, *zPIE: an autofocusing algorithm for ptychography*, Optics Letters **45**(7):2030–2033 (2020). 7, 103

[47] A. de Beurs, L. Loetgering, M. Herczog, M. Du, K. S. Eikema, and S. Witte, *aPIE: an angle calibration algorithm for reflection ptychography*, Optics Letters **47**(8):1949–1952 (2022). 7

[48] F. Zhang, I. Peterson, J. Vila-Comamala, A. Diaz, F. Berenguer, R. Bean, B. Chen, A. Menzel, I. K. Robinson, and J. M. Rodenburg, *Translation position determination in ptychographic coherent diffraction imaging*, Optics Express **21**(11):13592–13606 (2013). 7

[49] P. Li and A. Maiden, *Multi-slice ptychographic tomography*, Scientific Reports **8**(1):2049 (2018). 7

[50] A. M. Maiden, M. J. Humphry, F. Zhang, and J. M. Rodenburg, *Superresolution imaging via ptychography*, Journal of the Optical Society of America A **28**(4):604–612 (2011). 7, 90

[51] D. F. Gardner, M. Tanksalvala, E. R. Shanblatt, X. Zhang, B. R. Galloway, C. L. Porter, R. Karl Jr, C. Bevis, D. E. Adams, and H. C. Kapteyn, *Subwavelength coherent imaging of periodic samples using a 13.5 nm tabletop high-harmonic light source*, Nature Photonics **11**(4):259–263 (2017). 7, 108

[52] K. Giewekemeyer, M. Beckers, T. Gorniak, M. Grunze, T. Salditt, and A. Rosenhahn, *Ptychographic coherent x-ray diffractive imaging in the water window*, Optics Express **19**(2):1037–1050 (2011). 7

[53] M. Rose, T. Senkbeil, A. R. von Gundlach, S. Stuhr, C. Rumancev, D. Dzhigaev, I. Besedin, P. Skopintsev, L. Loetgering, J. Viefhaus, *et al.*, *Quantitative ptychographic bio-imaging in the water window*, Optics Express **26**(2):1237–1254 (2018). 7

[54] I. Mochi, P. Helfenstein, I. Mohacsi, R. Rajeev, D. Kazazis, S. Yoshitake, and Y. Ekinci, *RESCAN: an actinic lensless microscope for defect*

inspection of EUV reticles, Journal of Micro/Nanolithography, MEMS, and MOEMS **16**(4):041003–041003 (2017). 7

[55] Y. Nagata, T. Harada, T. Watanabe, H. Kinoshita, and K. Midorikawa, *At wavelength coherent scatterometry microscope using high-order harmonics for EUV mask inspection*, International Journal of Extreme Manufacturing **1**(3):032001 (2019). 7

[56] I. Mochi, S. Fernandez, R. Nebling, U. Locans, R. Rajeev, A. Dejkameh, D. Kazazis, L.-T. Tseng, S. Danylyuk, L. Juschkin, *et al.*, *Quantitative characterization of absorber and phase defects on EUV reticles using coherent diffraction imaging*, Journal of Micro/Nanolithography, MEMS, and MOEMS **19**(1):014002–014002 (2020). 7

[57] P. Thibault, M. Dierolf, O. Bunk, A. Menzel, and F. Pfeiffer, *Probe retrieval in ptychographic coherent diffractive imaging*, Ultramicroscopy **109**(4):338–343 (2009). 7, 63

[58] C. M. Kewish, P. Thibault, M. Dierolf, O. Bunk, A. Menzel, J. Vila-Comamala, K. Jefimovs, and F. Pfeiffer, *Ptychographic characterization of the wavefield in the focus of reflective hard X-ray optics*, Ultramicroscopy **110**(4):325–329 (2010). 7

[59] A. Schropp, R. Hoppe, V. Meier, J. Patommel, F. Seiboth, H. J. Lee, B. Nagler, E. C. Galtier, B. Arnold, U. Zastrau, *et al.*, *Full spatial characterization of a nanofocused x-ray free-electron laser beam by ptychographic imaging*, Scientific Reports **3**(1):1633 (2013). 7

[60] J. Vila-Comamala, A. Sakdinawat, and M. Guizar-Sicairos, *Characterization of x-ray phase vortices by ptychographic coherent diffractive imaging*, Optics Letters **39**(18):5281–5284 (2014). 7

[61] M. Du, L. Loetgering, K. S. E. Eikema, and S. Witte, *Measuring laser beam quality, wavefronts, and lens aberrations using ptychography*, Optics Express **28**(4):5022–5034 (2020). 7, 32, 48, 63

[62] L. Loetgering, M. Baluktsian, K. Keskinbora, R. Horstmeyer, T. Wilhein, G. Schütz, K. S. Eikema, and S. Witte, *Generation and characterization of focused helical x-ray beams*, Science Advances **6**(7):eaax8836 (2020). 7, 90

[63] M. Du, X. Liu, A. Pelekanidis, F. Zhang, L. Loetgering, P. Konold, C. L. Porter, P. Smorenburg, K. S. Eikema, and S. Witte, *High-resolution wavefront sensing and aberration analysis of multi-spectral extreme ultraviolet beams*, Optica **10**(2):255–263 (2023). 7, 20, 48, 49, 53, 56, 63, 65, 77, 90, 91

[64] S. Ghosh, Y. S. G. Nashed, O. Cossairt, and A. Katsaggelos, *ADP: Automatic differentiation ptychography*, in *2018 IEEE International Conference on Computational Photography (ICCP)*, pp. 1–10 (2018). 7

[65] S. Kandel, S. Maddali, M. Allain, S. O. Hruszkewycz, C. Jacobsen, and Y. S. G. Nashed, *Using automatic differentiation as a general framework for ptychographic reconstruction*, Optics Express **27**(13):18653–18672 (2019). 7

[66] J. Seifert, D. Bouchet, L. Loetgering, and A. P. Mosk, *Efficient and flexible approach to ptychography using an optimization framework based on automatic differentiation*, OSA Continuum **4**(1):121–128 (2021). 7

[67] E. Abraham, J. Zhou, and Z. Liu, *Speckle structured illumination endoscopy with enhanced resolution at wide field of view and depth of field*, Opto-Electron Adv **6**(7):220163 (2023). 7

[68] D. S. P. Molina, L. Loetgering, W. Eschen, J. Limpert, and J. Rothhardt, *Broadband ptychography using curved wavefront illumination*, Optics Express **31**(16):26958–26968 (2023). 8

[69] B. Wang, N. J. Brooks, P. Johnsen, N. W. Jenkins, Y. Esashi, I. Binnie, M. Tanksalvala, H. C. Kapteyn, and M. M. Murnane, *High-fidelity ptychographic imaging of highly periodic structures enabled by vortex high harmonic beams*, Optica **10**(9):1245–1252 (2023). 8, 9, 10, 13, 62, 91, 97

[70] A. M. Maiden, J. M. Rodenburg, and M. J. Humphry, *Optical ptychography: a practical implementation with useful resolution*, Optics Letters **35**(15):2585–2587 (2010). 8, 20, 90

[71] M. Guizar-Sicairos, M. Holler, A. Diaz, J. Vila-Comamala, O. Bunk, and A. Menzel, *Role of the illumination spatial-frequency spectrum for ptychography*, Physical Review B **86**(10):100103 (2012). 8, 9, 90

[72] A. Maiden, G. Morrison, B. Kaulich, A. Gianoncelli, and J. Rodenburg, *Soft X-ray spectromicroscopy using ptychography with randomly phased illumination*, Nature Communications **4**(1):1669 (2013). 8, 9, 90

[73] G. R. Morrison, F. Zhang, A. Gianoncelli, and I. K. Robinson, *X-ray ptychography using randomized zone plates*, Optics Express **26**(12):14915 (2018). 8, 9

[74] M. Odstrčil, M. Lebugle, M. Guizar-Sicairos, C. David, and M. Holler, *Towards optimized illumination for high-resolution ptychography*, Optics Express **27**(10):14981 (2019). 8

[75] W. Eschen, C. Liu, M. Steinert, D. S. P. Molina, T. Siefke, U. D. Zeitner, J. Kaspar, T. Pertsch, J. Limpert, and J. Rothhardt, *Structured illumination ptychography and at-wavelength characterization with an EUV diffuser at 13.5nm wavelength*, Optics Express **32**(3):3480–3491 (2024). 8, 9, 90

[76] M. Odstrčil, M. Lebugle, M. Guizar-Sicairos, C. David, and M. Holler, *Towards optimized illumination for high-resolution ptychography*, Optics Express **27**(10):14981–14997 (2019). 9, 90

[77] L. Allen, M. W. Beijersbergen, R. Spreeuw, and J. Woerdman, *Orbital angular momentum of light and the transformation of Laguerre-Gaussian laser modes*, Physical Review A **45**(11):8185 (1992). 10, 62

[78] A. McPherson, G. Gibson, H. Jara, U. Johann, T. S. Luk, I. McIntyre, K. Boyer, and C. K. Rhodes, *Studies of multiphoton production of vacuum-ultraviolet radiation in the rare gases*, Journal of the Optical Society of America B **4**(4):595–601 (1987). 10

[79] M. Ferray, A. L'Huillier, X. F. Li, L. A. Lompre, G. Mainfray, and C. Manus, *Multiple-harmonic conversion of 1064 nm radiation in rare gases*, Journal of Physics B: Atomic, Molecular and Optical Physics **21**(3):L31–L35 (1988). 10

[80] P. B. Corkum, *Plasma perspective on strong field multiphoton ionization*, Physical Review Letters **71**(13):1994 (1993). 10, 46

[81] M. Lewenstein, P. Balcou, M. Y. Ivanov, A. L'Huillier, and P. B. Corkum,

Theory of high-harmonic generation by low-frequency laser fields, Physical Review A **49**:2117–2132 (1994). 10, 46, 47, 62, 90

[82] G. S. M. Jansen, *Wavelength-resolved Extreme Ultraviolet Lensless Imaging and Metrology*, Phd-thesis - research and graduation internal, Vrije Universiteit Amsterdam (2020). 11, 16

[83] T. Ditmire, J. Tisch, E. Gumbrell, R. Smith, D. Meyerhofer, and M. Hutchinson, *Spatial coherence of short wavelength high-order harmonics.*, Applied Physics B: Lasers & Optics **65**(3) (1997). 10

[84] M. B. Gaarde, J. L. Tate, and K. J. Schafer, *Macroscopic aspects of attosecond pulse generation*, Journal of Physics B: Atomic, Molecular and Optical Physics **41**(13):132001 (2008). 11

[85] T. Popmintchev, M.-C. Chen, A. Bahabad, M. Gerrity, P. Sidorenko, O. Cohen, I. P. Christov, M. M. Murnane, and H. C. Kapteyn, *Phase matching of high harmonic generation in the soft and hard X-ray regions of the spectrum*, Proceedings of the National Academy of Sciences **106**(26):10516–10521 (2009). 11

[86] W. Paufler, B. Böning, and S. Fritzsche, *Coherence control in high-order harmonic generation with Laguerre-Gaussian beams*, Physical Review A **100**(1):013422 (2019). 11, 62, 69

[87] M. Lewenstein, P. Salires, and A. L'Huillier, *Phase of the atomic polarization in high-order harmonic generation*, Physical Review A **52**(6):4747–4754 (1995). 12, 47

[88] M. B. Gaarde, F. Salin, E. Constant, P. Balcou, K. J. Schafer, K. C. Kulander, and A. L'Huillier, *Spatiotemporal separation of high harmonic radiation into two quantum path components*, Physical Review A **59**(2):1367–1373 (1999). 12, 47

[89] F. Catoire, A. Ferré, O. Hort, A. Dubrouil, L. Quintard, D. Descamps, S. Petit, F. Burgy, E. Mével, Y. Mairesse, and E. Constant, *Complex structure of spatially resolved high-order-harmonic spectra*, Phys. Rev. A **94**:063401 (2016). 12, 47, 48, 69

[90] C. Hernández-García, J. A. Pérez-Hernández, J. Ramos, E. C. Jarque, L. Roso, and L. Plaja, *High-order harmonic propagation in gases within the discrete dipole approximation*, Physical Review A **82**(3):033432 (2010). 12, 73

[91] C. Guo, A. Harth, S. Carlström, Y.-C. Cheng, S. Mikaelsson, E. Marsell, C. Heyl, M. Miranda, M. Gisselbrecht, and M. B. Gaarde, *Phase control of attosecond pulses in a train*, Journal of Physics B: Atomic, Molecular and Optical Physics **51**(3):034006 (2018). 12, 47, 55, 62, 65, 82, 91

[92] H. Wikmark, C. Guo, J. Vogelsang, P. W. Smorenburg, H. Coudert-Alteirac, J. Lahl, J. Peschel, P. Rudawski, H. Dacasa, S. Carlström, *et al.*, *Spatiotemporal coupling of attosecond pulses*, Proceedings of the National Academy of Sciences **116**(11):4779–4787 (2019). 12, 47, 53, 55, 62, 65, 82

[93] A. L'Huillierr, P. Balcou, S. Candel, K. J. Schafer, and K. C. Kulander, *Calculations of high-order harmonic-generation processes in xenon at 1064 nm*, Physical Review A **46**(5):2778 (1992). 12, 48

[94] C. Hernández-García, J. San Román, L. Plaja, and A. Picón, *Quantum-*

path signatures in attosecond helical beams driven by optical vortices, New Journal of Physics **17**(9):093029 (2015). 12, 62, 63, 67, 69, 73, 82

[95] C. Hernández-García, A. Picón, J. San Román, and L. Plaja, *Attosecond extreme ultraviolet vortices from high-order harmonic generation*, Physical Review Letters **111**(8):083602 (2013). 12, 62, 63, 76, 77, 91

[96] G. Pariente and F. Quéré, *Spatio-temporal light springs: extended encoding of orbital angular momentum in ultrashort pulses*, Optics Letters **40**(9):2037–2040 (2015). 12, 62, 76, 77

[97] L. Clark, G. Guzzinati, A. Béché, A. Lubk, and J. Verbeeck, *Symmetry-constrained electron vortex propagation*, Physical Review A **93**(6):063840 (2016). 13, 66

[98] E. Yao, S. Franke-Arnold, J. Courtial, S. Barnett, and M. Padgett, *Fourier relationship between angular position and optical orbital angular momentum*, Optics Express **14**(20):9071–9076 (2006). 13

[99] F. Van der Veen and F. Pfeiffer, *Coherent x-ray scattering*, Journal of Physics: Condensed Matter **16**(28):5003 (2004). 13

[100] F. Zhang, M. Gouder, A. Pelekanidis, K. S. E. Eikema, and S. M. Witte, *Wavelength-resolved ptychographic imaging using high-harmonic generation pulse pairs*, in D. G. Smith and A. Erdmann (editors), *Computational Optics 2024*, vol. PC13023, p. PC1302307, International Society for Optics and Photonics, SPIE (2024). 15

[101] D. E. Spence, P. N. Kean, and W. Sibbett, *60-fsec pulse generation from a self-mode-locked Ti: sapphire laser*, Optics Letters **16**(1):42–44 (1991). 15

[102] A. Dubietis, G. Jonušauskas, and A. Piskarskas, *Powerful femtosecond pulse generation by chirped and stretched pulse parametric amplification in BBO crystal*, Optics Communications **88**(4-6):437–440 (1992). 16

[103] S. Witte and K. S. E. Eikema, *Ultrafast Optical Parametric Chirped-Pulse Amplification*, IEEE Journal of Selected Topics in Quantum Electronics **18**(1):296–307 (2012). 16

[104] D. W. E. Noom, S. Witte, J. Morgenweg, R. K. Altmann, and K. S. E. Eikema, *High-energy, high-repetition-rate picosecond pulses from a quasi-CW diode-pumped Nd:YAG system*, Optics Letters **38**(16):3021–3023 (2013). 16

[105] M.-S. Tsai, A.-Y. Liang, C.-L. Tsai, P.-W. Lai, M.-W. Lin, and M.-C. Chen, *Nonlinear compression toward high-energy single-cycle pulses by cascaded focus and compression*, Science Advances **8**(31):eabo1945 (2022). 17

[106] A. M. Weiner, *Ultrafast optics*, John Wiley & Sons (2011). 17

[107] D. J. Kane and R. Trebino, *Characterization of arbitrary femtosecond pulses using frequency-resolved optical gating*, IEEE Journal of Quantum Electronics **29**(2):571–579 (1993). 17

[108] F. Zhang, A. Pelekanidis, A. Karpavicius, M. Gouder, J. Seifert, K. Eikema, and S. Witte, *Characterizing post-compression of mJ-level ultrafast pulses via loose focusing in a gas cell*, Optics Express **32**(23):40990–41003 (2024). 17, 64, 106

[109] B. Enders, *Development and application of decoherence models in ptychographic diffraction imaging*, Ph.D. thesis, Technische Universität München

(2016). 20

[110] L. Loetgering, M. Du, D. B. Flaes, T. Aidukas, F. Wechsler, D. S. P. Molina, M. Rose, A. Pelekanidis, W. Eschen, J. Hess, *et al.*, *PtyLab.m/py/jl: a cross-platform, open-source inverse modeling toolbox for conventional and Fourier ptychography*, Optics Express **31**(9):13763–13797 (2023). 20, 32, 66, 95, 107, 108

[111] X. Liu, A. Pelekanidis, M. Du, F. Zhang, K. S. E. Eikema, and S. Witte, *Observation of chromatic effects in high-order harmonic generation*, Physical Review Research **5**:043100 (2023). 20, 63, 65, 90

[112] W. Zhang, H. Zhang, and G. Jin, *Band-extended angular spectrum method for accurate diffraction calculation in a wide propagation range*, Optics Letters **45**(6):1543–1546 (2020). 21

[113] R. Heintzmann, L. Loetgering, and F. Wechsler, *Scalable angular spectrum propagation*, Optica **10**(11):1407–1416 (2023). 21

[114] T. Shimobaba, K. Matsushima, T. Kakue, N. Masuda, and T. Ito, *Scaled angular spectrum method*, Optics Letters **37**(19):4128–4130 (2012). 21

[115] L. Greengard and J.-Y. Lee, *Accelerating the nonuniform fast Fourier transform*, Society for Industrial and Applied Mathematics Review **46**(3):443–454 (2004). 21

[116] X. Deng, B. Bihari, J. Gan, F. Zhao, and R. T. Chen, *Fast algorithm for chirp transforms with zooming-in ability and its applications*, Journal of the Optical Society of America A **17**(4):762–771 (2000). 21

[117] X. Yu, T. Xiahui, Q. Y. xiong, P. Hao, and W. Wei, *Wide-window angular spectrum method for diffraction propagation in far and near field*, Optics Letters **37**(23):4943–4945 (2012). 21

[118] D. Asoubar, S. Zhang, F. Wyrowski, and M. Kuhn, *Efficient semi-analytical propagation techniques for electromagnetic fields*, Journal of the Optical Society of America A **31**(3):591–602 (2014). 21

[119] D. G. Voelz and M. C. Roggemann, *Digital simulation of scalar optical diffraction: revisiting chirp function sampling criteria and consequences*, Applied Optics **48**(32):6132–6142 (2009). 21

[120] J. D. Schmidt, *Numerical simulation of optical wave propagation with examples in MATLAB*, SPIE (2010). 21, 22, 24, 26, 67, 107

[121] M. Leutenegger, R. Rao, R. A. Leitgeb, and T. Lasser, *Fast focus field calculations*, Optics Express **14**(23):11277–11291 (2006). 21

[122] Y. Hu, Z. Wang, X. Wang, S. Ji, C. Zhang, J. Li, W. Zhu, D. Wu, and J. Chu, *Efficient full-path optical calculation of scalar and vector diffraction using the Bluestein method*, Light: Science & Applications **9**(1):119 (2020). 21, 27

[123] E. Hecht, *Optics*, UK: Pearson Education Limited, 5 edn. (2017). 23

[124] K. Matsushima and T. Shimobaba, *Band-limited angular spectrum method for numerical simulation of free-space propagation in far and near fields*, Optics Express **17**(22):19662–19673 (2009). 26, 27, 29, 30, 40

[125] L. R. Rabiner, R. W. Schafer, and C. M. Rader, *The Chirp-Z transform algorithm*, IEEE Transactions on Audio and Electroacoustics **17**(2):86–92 (1969). 27

[126] C. E. Shannon, *Communication in the presence of noise*, Proceedings of the IRE **37**(1):10–21 (1949). 29

[127] *WolframAlpha*, `https://www.wolframalpha.com/input?i=Fourier+transform+calculator`. [Online; accessed 16-July-2024]. 38

[128] R. L. Sandberg, A. Paul, D. A. Raymondson, S. Hädrich, D. M. Gaudiosi, J. Holtsnider, I. T. Raanan, O. Cohen, M. M. Murnane, H. C. Kapteyn, *et al.*, *Lensless diffractive imaging using tabletop coherent high-harmonic soft-x-ray beams*, Physical Review Letters **99**(9):098103 (2007). 46

[129] Y. Mairesse, A. De Bohan, L. Frasinski, H. Merdji, L. Dinu, P. Monchicourt, P. Breger, M. Kovacev, R. Taïeb, B. Carré, *et al.*, *Attosecond synchronization of high-harmonic soft x-rays*, Science **302**(5650):1540–1543 (2003). 46

[130] K. Schafer, B. Yang, L. DiMauro, and K. Kulander, *Above threshold ionization beyond the high harmonic cutoff*, Physical Review Letters **70**(11):1599 (1993). 46

[131] K. Varju, P. Johnsson, J. Mauritsson, A. L'Huillier, and R. Lopez-Martens, *Physics of attosecond pulses produced via high harmonic generation*, American Journal of Physics **77**(5):389–395 (2009). 46, 62, 90

[132] F. Krausz and M. Ivanov, *Attosecond physics*, Reviews of Modern Physics **81**(1):163 (2009). 46

[133] P.-M. Paul, E. S. Toma, P. Breger, G. Mullot, F. Augé, P. Balcou, H. G. Muller, and P. Agostini, *Observation of a train of attosecond pulses from high harmonic generation*, Science **292**(5522):1689–1692 (2001). 46

[134] A. H. Zewail, *Femtochemistry: Atomic-scale dynamics of the chemical bond*, The Journal of Physical Chemistry A **104**(24):5660–5694 (2000). 46

[135] E. Goulielmakis, Z.-H. Loh, A. Wirth, R. Santra, N. Rohringer, V. S. Yakovlev, S. Zherebtsov, T. Pfeifer, A. M. Azzeer, M. F. Kling, *et al.*, *Real-time observation of valence electron motion*, Nature **466**(7307):739–743 (2010). 46

[136] S. Akturk, X. Gu, P. Bowlan, and R. Trebino, *Spatio-temporal couplings in ultrashort laser pulses*, Journal of Optics **12**(9) (2010). 46

[137] C. Bourassin-Bouchet, M. M. Mang, F. Delmotte, P. Chavel, and S. De Rossi, *How to focus an attosecond pulse*, Optics Express **21**(2):2506–2520 (2013). 46

[138] G. Cerullo, A. Dienes, and V. Magni, *Space–time coupling and collapse threshold for femtosecond pulses in dispersive nonlinear media*, Optics Letters **21**(1):65–67 (1996). 46

[139] B. Beaurepaire, D. Guénot, A. Vernier, F. Böhle, M. Perrier, A. Jullien, R. Lopez-Martens, A. Lifschitz, and J. Faure, *Limitations in ionization-induced compression of femtosecond laser pulses due to spatio-temporal couplings*, Optics Express **24**(9):9693–9705 (2016). 46

[140] M. A. Porras, *Propagation-induced changes in the instantaneous polarization state, phase, and carrier-envelope phase of few-cycle pulsed beams*, Journal of the Optical Society of America B **30**(6):1652–1659 (2013). 47

[141] A. L. Cavalieri, N. Müller, T. Uphues, V. S. Yakovlev, A. Baltuška, B. Horvath, B. Schmidt, L. Blümel, R. Holzwarth, S. Hendel, *et al.*, *Attosecond spectroscopy in condensed matter*, Nature **449**(7165):1029–1032 (2007). 47

[142] M. Schultze, M. Fieß, N. Karpowicz, J. Gagnon, M. Korbman, M. Hofstetter, S. Neppl, A. L. Cavalieri, Y. Komninos, T. Mercouris, *et al.*, *Delay in photoemission*, Science **328**(5986):1658–1662 (2010). 47

[143] B. Zhang, D. F. Gardner, M. H. Seaberg, E. R. Shanblatt, C. L. Porter, R. Karl, C. A. Mancuso, H. C. Kapteyn, M. M. Murnane, and D. E. Adams, *Ptychographic hyperspectral spectromicroscopy with an extreme ultraviolet high harmonic comb*, Optics Express **24**(16):18745–18754 (2016). 47

[144] E. Frumker, G. G. Paulus, H. Niikura, A. Naumov, D. M. Villeneuve, and P. B. Corkum, *Order-dependent structure of high harmonic wavefronts*, Optics Express **20**(13):13870 (2012). 47, 48

[145] L. Quintard, V. Strelkov, J. Vabek, O. Hort, A. Dubrouil, D. Descamps, F. Burgy, C. Péjot, E. Mével, F. Catoire, *et al.*, *Optics-less focusing of XUV high-order harmonics*, Science Advances **5**(4):eaau7175 (2019). 47, 51

[146] M. Hoflund, J. Peschel, M. Plach, H. Dacasa, K. Veyrinas, E. Constant, P. Smorenburg, H. Wikmark, S. Maclot, C. Guo, *et al.*, *Focusing Properties of High-Order Harmonics*, Ultrafast Science **2021** (2021). 47

[147] D. R. Austin, T. Witting, C. A. Arrell, F. Frank, A. S. Wyatt, J. P. Marangos, J. W. Tisch, and I. A. Walmsley, *Lateral shearing interferometry of high-harmonic wavefronts*, Optics Letters **36**(10):1746–1748 (2011). 48

[148] D. T. Lloyd, K. OKeeffe, and S. M. Hooker, *Complete spatial characterization of an optical wavefront using a variable-separation pinhole pair*, Optics Letters **38**(7):1173–1175 (2013). 48

[149] D. G. Lee, J. J. Park, J. H. Sung, and C. H. Nam, *Wave-front phase measurements of high-order harmonic beams by use of point-diffraction interferometry*, Optics Letters **28**(6):480–482 (2003). 48

[150] P. Mercère, P. Zeitoun, M. Idir, S. L. Pape, D. Douillet, X. Levecq, G. Dovillaire, S. Bucourt, K. A. Goldberg, P. P. Naulleau, and S. Rekawa, *Hartmann wave-front measurement at 13.4 nm with λEUV/120 accuracy*, Optics Letters **28**(17):1534–1536 (2003). 48

[151] L. Freisem, G. S. M. Jansen, D. Rudolf, K. S. E. Eikema, and S. Witte, *Spectrally resolved single-shot wavefront sensing of broadband high-harmonic sources*, Optics Express **26**(6):6860–6871 (2018). 48, 91

[152] M. J. Padgett, *Orbital angular momentum 25 years on*, Optics Express **25**(10):11265–11274 (2017). 62

[153] Y. Shen, X. Wang, Z. Xie, C. Min, X. Fu, Q. Liu, M. Gong, and X. Yuan, *Optical vortices 30 years on: OAM manipulation from topological charge to multiple singularities*, Light: Science & Applications **8**(1):90 (2019). 62

[154] S. W. Hell and J. Wichmann, *Breaking the diffraction resolution limit by stimulated emission: stimulated-emission-depletion fluorescence microscopy*, Optics Letters **19**(11):780–782 (1994). 62

[155] L. Li and F. Li, *Beating the Rayleigh limit: Orbital-angular-momentum-based super-resolution diffraction tomography*, Physical Review E **88**(3):033205 (2013). 62

[156] G. Vicidomini, P. Bianchini, and A. Diaspro, *STED super-resolved microscopy*, Nature Methods **15**(3):173–182 (2018). 62

[157] K. Murzyn, M. L. S. van der Geest, L. Guery, Z. Nie, P. van Essen, S. Witte, and P. M. Kraus, *Breaking Abbes diffraction limit with harmonic deactivation microscopy*, Science Advances **10**(46):eadp3056 (2024). 62

[158] K. Gahagan and G. Swartzlander, *Optical vortex trapping of particles*, Optics Letters **21**(11):827–829 (1996). 62

[159] M. Padgett and R. Bowman, *Tweezers with a twist*, Nature Photonics **5**(6):343–348 (2011). 62

[160] A. E. Willner, H. Huang, Y. Yan, Y. Ren, N. Ahmed, G. Xie, C. Bao, L. Li, Y. Cao, Z. Zhao, J. Wang, M. P. J. Lavery, M. Tur, S. Ramachandran, A. F. Molisch, *et al.*, *Optical communications using orbital angular momentum beams*, Advances in Optics and Photonics **7**(1):66–106 (2015). 62

[161] J. Wang, *Advances in communications using optical vortices*, Photonics Research **4**(5):B14–B28 (2016). 62

[162] E. Stegenburgs, A. Bertoncini, A. Trichili, M. S. Alias, T. K. Ng, M.-S. Alouini, C. Liberale, and B. S. Ooi, *Near-infrared OAM communication using 3D-printed microscale spiral phase plates*, IEEE Communications Magazine **57**(8):65–69 (2019). 62

[163] A. Mair, A. Vaziri, G. Weihs, and A. Zeilinger, *Entanglement of the orbital angular momentum states of photons*, Nature **412**(6844):313–316 (2001). 62

[164] R. Fickler, R. Lapkiewicz, W. N. Plick, M. Krenn, C. Schaeff, S. Ramelow, and A. Zeilinger, *Quantum entanglement of high angular momenta*, Science **338**(6107):640–643 (2012). 62

[165] A. G. Peele, P. J. McMahon, D. Paterson, C. Q. Tran, A. P. Mancuso, K. A. Nugent, J. P. Hayes, E. Harvey, B. Lai, and I. McNulty, *Observation of an x-ray vortex*, Optics Letters **27**(20):1752–1754 (2002). 62

[166] P. Rebernik Ribič, B. Rösner, D. Gauthier, E. Allaria, F. Döring, L. Foglia, L. Giannessi, N. Mahne, M. Manfredda, C. Masciovecchio, *et al.*, *Extreme-ultraviolet vortices from a free-electron laser*, Physical Review X **7**(3):031036 (2017). 62

[167] L. Rego, J. S. Román, A. Picón, L. Plaja, and C. Hernández-García, *Nonperturbative twist in the generation of extreme-ultraviolet vortex beams*, Physical Review Letters **117**(16):163202 (2016). 62, 63, 66, 91

[168] C. Hernández-García, L. Rego, J. San Román, A. Picón, and L. Plaja, *Attosecond twisted beams from high-order harmonic generation driven by optical vortices*, High Power Laser Science and Engineering **5**:e3 (2017). 62, 63

[169] W. Paufler, B. Böning, and S. Fritzsche, *High harmonic generation with Laguerre–Gaussian beams*, Journal of Optics **21**(9):094001 (2019). 62, 63, 91

[170] C. Jin, B. Li, K. Wang, C. Xu, X. Tang, C. Yu, and C. Lin, *Phase-matching analysis in high-order harmonic generation with nonzero orbital angular momentum Laguerre-Gaussian beams*, Physical Review A **102**(3):033113 (2020). 62, 63

[171] M. Zürch, C. Kern, P. Hansinger, A. Dreischuh, and C. Spielmann, *Strong-field physics with singular light beams*, Nature Physics **8**(10):743–

746 (2012). 62, 91

[172] G. Gariepy, J. Leach, K. T. Kim, T. J. Hammond, E. Frumker, R. W. Boyd, and P. B. Corkum, *Creating high-harmonic beams with controlled orbital angular momentum*, Physical Review Letters **113**(15):153901 (2014). 62, 77, 91

[173] R. Géneaux, A. Camper, T. Auguste, O. Gobert, J. Caillat, R. Taeb, and T. Ruchon, *Synthesis and characterization of attosecond light vortices in the extreme ultraviolet*, Nature Communications **7**(1):12583 (2016). 62, 63, 91

[174] R. Géneaux, C. Chappuis, T. Auguste, S. Beaulieu, T. T. Gorman, F. Lepetit, L. F. DiMauro, and T. Ruchon, *Radial index of Laguerre-Gaussian modes in high-order-harmonic generation*, Physical Review A **95**(5):051801 (2017). 62, 63, 69

[175] D. Gauthier, P. R. Ribič, G. Adhikary, A. Camper, C. Chappuis, R. Cucini, L. DiMauro, G. Dovillaire, F. Frassetto, R. Géneaux, *et al.*, *Tunable orbital angular momentum in high-harmonic generation*, Nature Communications **8**(1):14971 (2017). 62, 77

[176] F. Kong, C. Zhang, F. Bouchard, Z. Li, G. G. Brown, D. H. Ko, T. Hammond, L. Arissian, R. W. Boyd, E. Karimi, *et al.*, *Controlling the orbital angular momentum of high harmonic vortices*, Nature Communications **8**(1):14970 (2017). 62, 77

[177] F. Sanson, A. Pandey, F. Harms, G. Dovillaire, E. Baynard, J. Demailly, O. Guilbaud, B. Lucas, O. Neveu, M. Pittman, *et al.*, *Hartmann wavefront sensor characterization of a high charge vortex beam in the extreme ultraviolet spectral range*, Optics Letters **43**(12):2780–2783 (2018). 62, 63, 91

[178] K. M. Dorney, L. Rego, N. J. Brooks, J. San Román, C.-T. Liao, J. L. Ellis, D. Zusin, C. Gentry, Q. L. Nguyen, J. M. Shaw, *et al.*, *Controlling the polarization and vortex charge of attosecond high-harmonic beams via simultaneous spin–orbit momentum conservation*, Nature photonics **13**(2):123–130 (2019). 62, 77, 91

[179] F. Sanson, A. Pandey, I. Papagiannouli, F. Harms, G. Dovillaire, E. Baynard, J. Demailly, O. Guilbaud, B. Lucas, O. Neveu, *et al.*, *Highly multimodal structure of high topological charge extreme ultraviolet vortex beams*, Optics Letters **45**(17):4790–4793 (2020). 62, 63, 66, 71, 74, 91

[180] A. K. Pandey, A. de las Heras, T. Larrieu, J. San Román, J. Serrano, L. Plaja, E. Baynard, M. Pittman, G. Dovillaire, S. Kazamias, *et al.*, *Characterization of extreme ultraviolet vortex beams with a very high topological charge*, ACS Photonics **9**(3):944–951 (2022). 62, 63, 66, 91

[181] L. Rego, K. M. Dorney, N. J. Brooks, Q. L. Nguyen, C.-T. Liao, J. San Román, D. E. Couch, A. Liu, E. Pisanty, M. Lewenstein, *et al.*, *Generation of extreme-ultraviolet beams with time-varying orbital angular momentum*, Science **364**(6447):eaaw9486 (2019). 62, 77, 91

[182] A. de las Heras, D. Schmidt, J. S. Román, J. Serrano, J. Barolak, B. Ivanic, C. Clarke, N. Westlake, D. E. Adams, L. Plaja, C. G. Durfee, and C. Hernández-García, *Attosecond vortex pulse trains*, Optica **11**(8):1085–

1093 (2024). 62, 77

[183] R. A. Bartels, A. Paul, H. Green, H. C. Kapteyn, M. M. Murnane, S. Backus, I. P. Christov, Y. Liu, D. Attwood, and C. Jacobsen, *Generation of spatially coherent light at extreme ultraviolet wavelengths*, Science **297**(5580):376–378 (2002). 62, 90

[184] T. Popmintchev, M.-C. Chen, D. Popmintchev, P. Arpin, S. Brown, S. Ališauskas, G. Andriukaitis, T. Balčiunas, O. D. Mücke, A. Pugzlys, A. Baltuška, B. Shim, S. E. Schrauth, A. Gaeta, C. Hernández-García, *et al.*, *Bright coherent ultrahigh harmonics in the keV X-ray regime from mid-infrared femtosecond lasers*, Science **336**(6086):1287–1291 (2012). 62, 90

[185] R. Klas, A. Kirsche, M. Gebhardt, J. Buldt, H. Stark, S. Hädrich, J. Rothhardt, and J. Limpert, *Ultra-short-pulse high-average-power megahertz-repetition-rate coherent extreme-ultraviolet light source*, PhotoniX **2**:1–8 (2021). 62, 90

[186] P. Salières, A. L'Huillier, and M. Lewenstein, *Coherence control of high-order harmonics*, Physical Review Letters **74**(19):3776 (1995). 62

[187] T. Popmintchev, M.-C. Chen, A. Bahabad, M. Gerrity, P. Sidorenko, O. Cohen, I. P. Christov, M. M. Murnane, and H. C. Kapteyn, *Phase matching of high harmonic generation in the soft and hard X-ray regions of the spectrum*, Proceedings of the National Academy of Sciences **106**(26):10516–10521 (2009). 62

[188] R. Weissenbilder, S. Carlström, L. Rego, C. Guo, C. Heyl, P. Smorenburg, E. Constant, C. Arnold, and A. L'Huillier, *How to optimize high-order harmonic generation in gases*, Nature Reviews Physics **4**(11):713–722 (2022). 62

[189] J. Gao, C. Yang, X. Ge, Y. Zheng, Z. Zeng, and R. Li, *Phase-matching of high-order harmonic generation in the extreme ultraviolet region with orbital angular momentum*, Optics Express **32**(1):871–878 (2024). 62, 63

[190] M. Lewenstein, P. Salieres, and A. L'Huillier, *Phase of the atomic polarization in high-order harmonic generation*, Physical Review A **52**(6):4747 (1995). 62

[191] S. Kazamias, F. Weihe, D. Douillet, C. Valentin, T. Planchon, S. Sebban, G. Grillon, F. Augé, D. Hulin, and P. Balcou, *High order harmonic generation optimization with an apertured laser beam*, The European Physical Journal D-Atomic, Molecular, Optical and Plasma Physics **21**:353–359 (2002). 64

[192] D. Malacara-Hernández and A. Gomez-Vieyra, *Optical design of systems with off-axis spherical mirrors*, in *22nd Congress of the International Commission for Optics: Light for the Development of the World*, vol. 8011, pp. 298–304, SPIE (2011). 66, 70, 106

[193] A. I. Gonzalez, G. Jargot, P. Rigaud, L. Lavenu, F. Guichard, A. Comby, T. Auguste, O. Sublemontier, M. Bougeard, Y. Zaouter, P. Georges, M. Hanna, and T. Ruchon, *Spatio-spectral structures in high harmonic generation driven by tightly focused high repetition rate lasers*, J. Opt. Soc. Am. B **35**(4):A6–A14 (2018). 69

[194] P. M. Paul, E. S. Toma, P. Breger, G. Mullot, F. Aug, P. Balcou, H. G.

Muller, and P. Agostini, *Observation of a Train of Attosecond Pulses from High Harmonic Generation*, Science **292**(5522):1689–1692 (2001). 76

[195] C. Y. Hémonnot and S. Köster, *Imaging of biological materials and cells by X-ray scattering and diffraction*, ACS Nano **11**(9):8542–8559 (2017). 90

[196] C. Porter, T. Coenen, N. Geypen, S. Scholz, L. van Rijswijk, H.-K. Nienhuys, J. Ploegmakers, J. Reinink, H. Cramer, R. van Laarhoven, D. O'Dwyer, P. Smorenburg, A. Invernizzi, R. Wohrwag, H. Jonquiere, *et al.*, *Soft x-ray: novel metrology for 3D profilometry and device pitch overlay*, in *Metrology, Inspection, and Process Control XXXVII*, vol. 12496, pp. 412–420, SPIE (2023). 90

[197] I. Pupeza, C. Zhang, M. Högner, and J. Ye, *Extreme-ultraviolet frequency combs for precision metrology and attosecond science*, Nature Photonics **15**(3):175–186 (2021). 90

[198] W. Eschen, C. Liu, D. S. P. Molina, R. Klas, J. Limpert, and J. Rothhardt, *High-speed and wide-field nanoscale table-top ptychographic EUV imaging and beam characterization with a sCMOS detector*, Optics Express **31**(9):14212–14224 (2023). 90

[199] G. K. Tadesse, W. Eschen, R. Klas, M. Tschernajew, F. Tuitje, M. Steinert, M. Zilk, V. Schuster, M. Zürch, T. Pertsch, *et al.*, *Wavelength-scale ptychographic coherent diffractive imaging using a high-order harmonic source*, Scientific Reports **9**(1):1735 (2019). 90, 97

[200] J. Vila-Comamala, A. Diaz, M. Guizar-Sicairos, A. Mantion, C. M. Kewish, A. Menzel, O. Bunk, and C. David, *Characterization of high-resolution diffractive X-ray optics by ptychographic coherent diffractive imaging*, Optics Express **19**(22):21333–21344 (2011). 90

[201] Y. Yao, Y. Jiang, J. Klug, Y. Nashed, C. Roehrig, C. Preissner, F. Marin, M. Wojcik, O. Cossairt, and Z. Cai, *Broadband X-ray ptychography using multi-wavelength algorithm*, Journal of Synchrotron Radiation **28**(1):309–317 (2021). 90

[202] B. L. Henke, E. M. Gullikson, and J. C. Davis, *X-Ray Interactions: Photoabsorption, Scattering, Transmission, and Reflection at E = 50-30,000 eV, Z = 1-92*, Atomic Data and Nuclear Data Tables **54**(2):181–342 (1993). 90

[203] A. Rana, J. Zhang, M. Pham, A. Yuan, Y. H. Lo, H. Jiang, S. J. Osher, and J. Miao, *Potential of attosecond coherent diffractive imaging*, Physical Review Letters **125**(8):086101 (2020). 90

[204] J. Huijts, S. Fernandez, D. Gauthier, M. Kholodtsova, A. Maghraoui, K. Medjoubi, A. Somogyi, W. Boutu, and H. Merdji, *Broadband coherent diffractive imaging*, Nature Photonics **14**(10):618–622 (2020). 90

[205] X. Ji, X. He, Z. Jiang, Y. Kong, S. Wang, and C. Liu, *Resolution enhancement with highly curved illumination in ptychography*, Applied Optics **61**(34):10150–10158 (2022). 90

[206] M. Pancaldi, F. Guzzi, C. S. Bevis, M. Manfredda, J. Barolak, S. Bonetti, I. Bykova, D. D. Angelis, G. D. Ninno, M. Fanciulli, L. Novinec, E. Pedersoli, A. Ravindran, B. Rösner, C. David, *et al.*, *High-resolution ptychographic imaging at a seeded free-electron laser source using OAM beams*,

Optica **11**(3):403–411 (2024). 90

[207] Y. Iwasaki, A. G. Kusne, and I. Takeuchi, *Comparison of dissimilarity measures for cluster analysis of X-ray diffraction data from combinatorial libraries*, npj Computational Materials **3**(1):1–9 (2017). 91, 92, 110

[208] M. Van Heel and M. Schatz, *Fourier shell correlation threshold criteria*, Journal of Structural Biology **151**(3):250–262 (2005). 94

[209] Vortex Photonics, `https://www.vortex-photonics.de/`. 96

[210] S. M. Kay, *Fundamentals of Statistical Signal Processing: Estimation Theory*, Prentice-Hall, Inc. (1993). 102

[211] D. Bouchet, S. Rotter, and A. P. Mosk, *Maximum information states for coherent scattering measurements*, Nature Physics **17**(5):564–568 (2021). 102

[212] D. Bouchet, J. Seifert, and A. P. Mosk, *Optimizing illumination for precise multi-parameter estimations in coherent diffractive imaging*, Optics Letters **46**(2):254–257 (2021). 102

[213] D. Bouchet, J. Dong, D. Maestre, and T. Juffmann, *Fundamental Bounds on the Precision of Classical Phase Microscopes*, Physical Review Applied **15**(2):024047 (2021). 104

[214] D. Paganin, *Coherent X-ray optics*, 6, Oxford University Press, USA (2006). 106

[215] Optix fab, `http://www.optixfab.com/`. 106

[216] P. Li, *Investigations and improvements in ptychographic imaging*, Ph.D. thesis, University of Sheffield (2016). 108

[217] A. Maiden, D. Johnson, and P. Li, *Further improvements to the ptychographical iterative engine*, Optica **4**(7):736–745 (2017). 108